UTTAC-87, 2018

UTTAC

ANNUAL REPORT 2017

TANDEM ACCELERATOR COMPLEX
Research Facility Center for Science and Technology
University of Tsukuba

http://www.tac.tsukuba.ac.jp/

UTTAC

ANNUAL REPORT 2017

April 1, 2017 – March 31, 2018

UTTAC-87, 2018

Editors : Tetsuaki Moriguchi, Kimikazu Sasa, Yoshihiro Yamato, Masumi Matsumura, Masao Sataka, Hiroshi Naramoto, and Hiroshi Kudo (editor-in-chief)

UTTAC ANNUAL REPORT is a series of issues, which include annual reports of
Tandem Accelerator Complex, Research Facility Center
for Science and Technology, University of Tsukuba.

Tandem Accelerator Complex, Research Facility Center for Science and Technology,
University of Tsukuba
Tennodai 1-1-1, Tsukuba, Ibaraki 305-8577, Japan

annual@tac.tsukuba.ac.jp

PREFACE

This annual report covers researches carried out at University of Tsukuba Tandem Accelerator Complex (UTTAC) during the fiscal year 2017 (1 April 2017 ~ 31 March 2018). The topics include not only accelerator-based researches using the 6MV Pelletron and 1MV Tandetron accelerators, but also radioisotope-based researches including positron annihilation spectroscopy and Mössbauer spectroscopy.

August 1, 2018
Editorial board

EDITORIAL: Research results and the facility's publication list

In the early period of UTTAC, the publication list in its annual report was certainly the outcome of the facility. After about 40 years since then, the research field at UTTAC has expanded entirely towards applied studies such as accelerator mass spectrometry, ion beam analysis and modification of materials, radiation tolerance test of electronic devices, etc. Reflecting such circumstances, for many users the experimental data taken at UTTAC is necessary but not enough. In actual, they usually proceed with research using other facilities in parallel. It follows that the equivalence of the user's research results and the facility's outcome, mentioned above, has become unclear. It is the publication list of this Annual Report that tells such a trend clearly. Here at UTTAC, while there is a certain number of direct outcome, we see a remarkable increase of the research results that are generated indirectly or supportively.

July 31, 2018
Editorial board

CONTENTS

1. ACCELERATOR AND RELATED FACILITIES

2. NUCLEAR AND ATOMIC PHYSICS

3. ACCELERATOR MASS SPECTROMETRY

4. BEAM AND ISOTOPE APPLICATIONS

1.

ACCELERATOR AND RELATED FACILITIES

1.1 Accelerator operation 2017

K. Sasa, S. Ishii, H. Oshima, Y. Tajima, T. Takahashi, Y. Yamato, T. Moriguchi, A. Uedono

1 MV Tandetron accelerator

The operating time and the experimental beam time of the 1 MV Tandetron accelerator were 628.3 and 300.7 hours, respectively, during the total service time in FY 2017. The total number of 59 days was used for beam experiments. A total of 244 researchers and students used Tandetron in FY 2017. Figures 1 and 2 show classification of the accelerated ions and of the experimental purposes, respectively. Notably, 13.9% of the accelerator machine time was used by external users for materials analysis with RBS/ERDA.

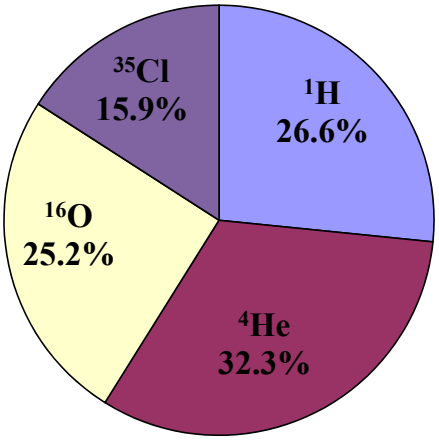

Fig. 1. Accelerated ions by the 1 MV Tandetron accelerator in FY 2017.

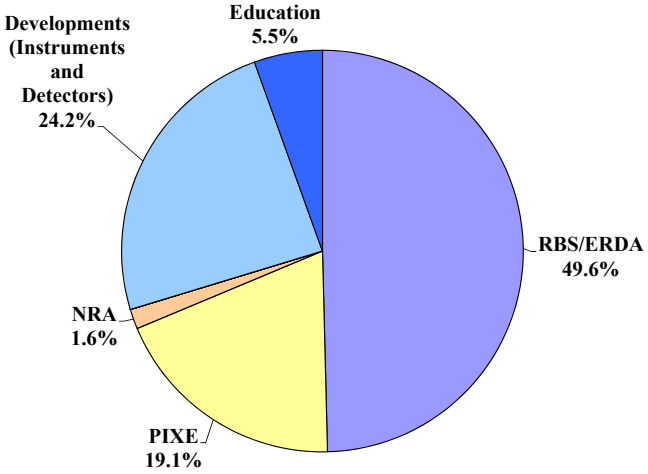

Fig. 2. Purpose of use of the 1 MV Tandetron accelerator in FY 2017.

6 MV Pelletron tandem accelerator

The operating time and the experimental beam time of the 6 MV Pelletron tandem accelerator were 1857 and 1501 hours, respectively, in FY 2017. The number of days the accelerator was in operation was 154. As a result, 90 research programs were carried out and a total of 636 researchers used the accelerator. Figure 3 shows the beam time histogram with respect to the terminal voltage. Figures 4 and 5 show classification of the accelerated ions and of the experimental purposes, respectively. The operating time at the terminal voltage of 6 MV was 52.2% of the total beam time. The AMS experiment occupied the longest beam time, 47.3% of the total. This was followed by the microbeam experiments, 21.6% of the total, for study of structural materials in the Strategic Innovation Promotion Program: SIP.

There was no major trouble for routine beam delivery and experiments in 2017. However, the foil changer in the accelerator terminal caused malfunctioning in circulating the carbon foil unit, as was the same case as in 2016 [1]. We opened the accelerator tank and repaired the foil changer in March 2018. A stripper gas valve in the accelerator terminal was also replaced with new one at the same time. As for the rest of maintenances, we repaired the beam attenuator on the low energy side.

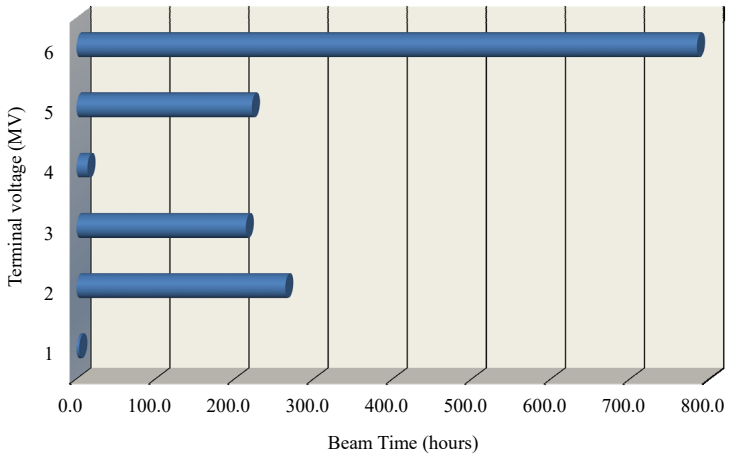

Fig. 3. Beam time histogram as a function of the terminal voltage for the 6 MV Pelletron tandem accelerator in FY 2017.

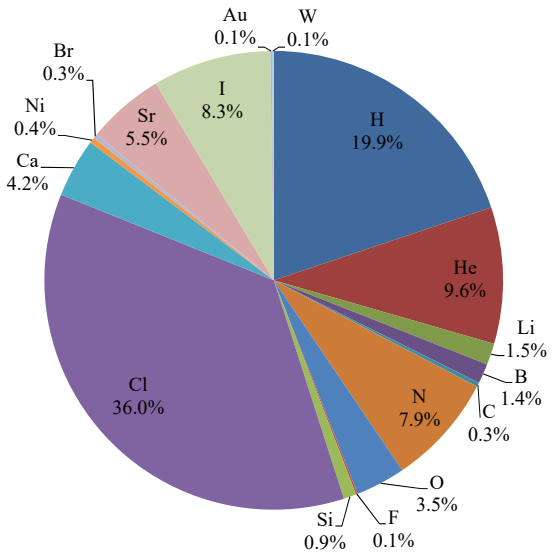

Fig. 4. Accelerated ions by the 6 MV Pelletron tandem accelerator in FY 2017.

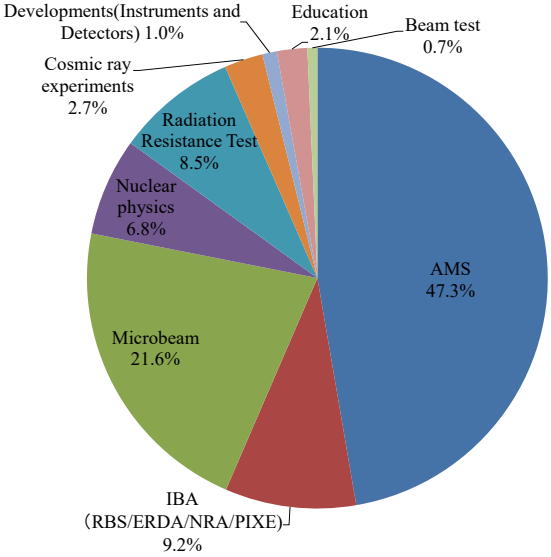

Fig. 5. Purpose of use of the 6 MV Pelletron tandem accelerator in FY 2017.

Reference

[1] K. Sasa et al., UTTAC ANNUAL REPORT 2016, UTTAC-86 (2017) 1.

1.2 Measurement of the polarization of the polarized proton beam via the p-^{4}He elastic scattering reaction

T. Moriguchi, M. Amano, Y. Yamato, A. Ozawa, S. Suzuki, D. Kamioka, D. Nagae[1]

The Lamb-shift polarized ion source (PIS) was installed at UTTAC in 1976 for experimental nuclear physics [1]. PIS was damaged seriously by the Great East Japan Earthquake, but the decision was made to reconstruct PIS as one of the ion sources for the newly designed 6 MV tandem accelerator. Following the reconstruction of PIS, we attempted to generate the polarized beams and confirmed the resonance peaks which correspond to polarized proton and deuteron beams [2]. In FY2017, we measured the polarization of a polarized proton beam downstream of the 6 MV tandem accelerator with a polarimeter using the p-^{4}He elastic scattering reaction.

The polarized proton beam from PIS was accelerated to 12 MeV and transported to the A6 course. The spin quantization axis was set to be perpendicular to the horizontal plane. The direction of the spin (spin-up or spin-down) could be selected by reversing the direction of the magnetic field of the spin filter, which is the main component of PIS for the generation of polarized beams. Figure 1 shows the schematic cross section of the polarimeter used in the present measurement [3], which is viewed along the direction of the spin quantization axis of the polarized beam. The inside of the polarimeter was filled with ^{4}He gas of approximately 0.1 MPa. Elastically scattered protons in the polarimeter traveled through the intervals of each vane and were detected by silicon detectors at both sides. We connected this polarimeter to the end of the A6 course. Polarization P is expressed as

$$A \cdot P = \frac{N_{\mathrm{L}} - N_{\mathrm{R}}}{N_{\mathrm{L}} + N_{\mathrm{R}}} \tag{1}$$

where A is the analyzing power; N_{L} and N_{R} are the number of elastically scattered protons detected by the silicon detectors on the left and right sides of the polarimeter, respectively. In this case, A is approximately equal to one [4]. Figure 2 shows the experimental results obtained from the two silicon detectors. The main peaks shown in Fig. 2 correspond to the energy of the elastically scattered protons. In the case of spin-up (spin-down), the number of the protons scattered to the left (right) side is larger than that to the other side, as shown in Fig. 2. From this experimental result and using Eq. (1), we found that the polarization at the end of the beam course was approximately 44% for the spin-up case and 36% for the spin-down case. These polarizations are lower than that of downstream of the PIS (approximately 80%) obtained using the quenching method [2]. One of the reasons for this depolarization may be the electron exchange between ions and a residual gas inside the beam duct in the accelerator. In order to suppress the depolarization, we used a thin carbon foil (approximately ten μg/cm^2) as the electron stripper without argon gas in the gas stripper canal. However, owing to possible defects in the gas valve or vacuum system, argon gas might have leaked slightly into the canal. This would increase the depolarization. We are now attempting to improve the polarization of the polarized proton beam.

[1]RIKEN, Nishina Center

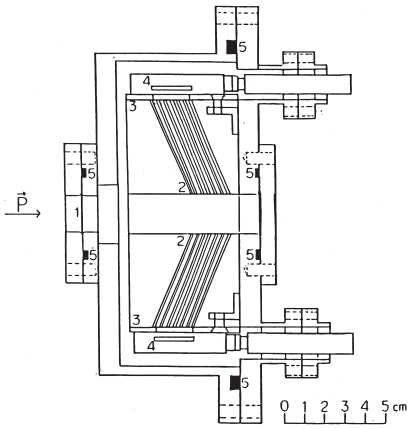

Fig. 1. Schematic cross section of the polarimeter with labels: 1. Harver foils, 2. vanes, 3. diaphragms, 4. silicon detectors, and 5. O-ring [3].

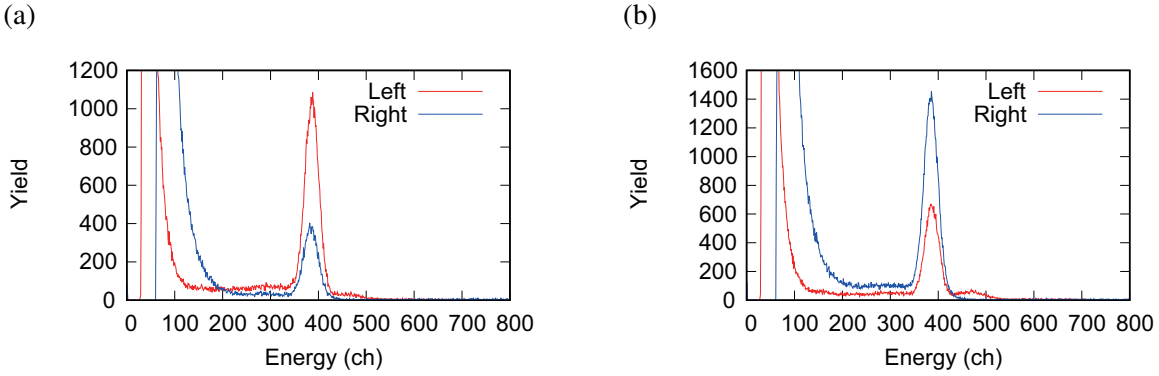

Fig. 2. Energy spectra obtained from silicon detectors at the left (red line) and the right (blue line) sides of the polarimeter. Shown in (a) and (b) are the results for spin-up and spin-down, respectively.

References

[1] Y. Tagishi et al., Nucl. Instrum. Methods 164 (1979) 411.

[2] T. Moriguchi et al., UTTAC Annual Report 2016, UTTAC-8 (2017) 5.

[3] A. Kurashima et al., UTTAC Annual Report 1987, UTTAC-54 (1988) 14.

[4] P. W. Keaton, Jr. et al., Phys. Rev. Lett. 29 (1972) 880.

1.3 Charge state distribution of ions accelerated by the 6MV tandem accelerator at UTTAC

M. Sataka, T. Takahashi, H. Naramoto, H. Kudo, K. Sasa

Ion acceleration tests with the 6MV tandem accelerator have been continued from the previous fiscal year [1]. Since we have only about 2 year experience of the accelerator operation, there is still a lack of technical data required when an experiment at UTTAC is planned. Such data are of practical importance especially for external users who collect data for wide range of experimental parameters by utilizing several accelerator facilities. One of the examples is the study of radiation tolerance of electronic devices used in space [2].

We have measured beam currents of accelerated ions at the terminal voltages of 1, 3 and 6 MV as a function of ion charge state, employing Ar gas as the charge stripper. We also examined the foil stripper for several ion species. Both of the strippers were set and used under the conditions to obtain the most effective beam transport. The ions tested were Li, B, C, F, Si, Br and W. For the ions heavier than Br, fluctuation of the terminal voltage by electron loading could be suppressed by tightening the entrance slit. This allowed to stabilize the terminal voltage by reducing the ion beam current only by ~10%.

Figure 1 shows the beam current vs. charge state of silicon ions measured for the terminal voltage of 6MV using the gas and foil strippers. The distribution of beam current shifts to the higher charge state by 2–3 for use of the foil stripper than for the gas stripper. The practical maximum energy for Si obtained is 66 MeV for Si^{10+} when using the foil stripper, and 60 MeV for Si^{9+} when using the gas stripper. The most probable charge state of Si is found to be increased by ~3 for the foil stripper (7+ state) compared with the gas stripper (4+ state). For Br, the corresponding increase is found to be ~6.

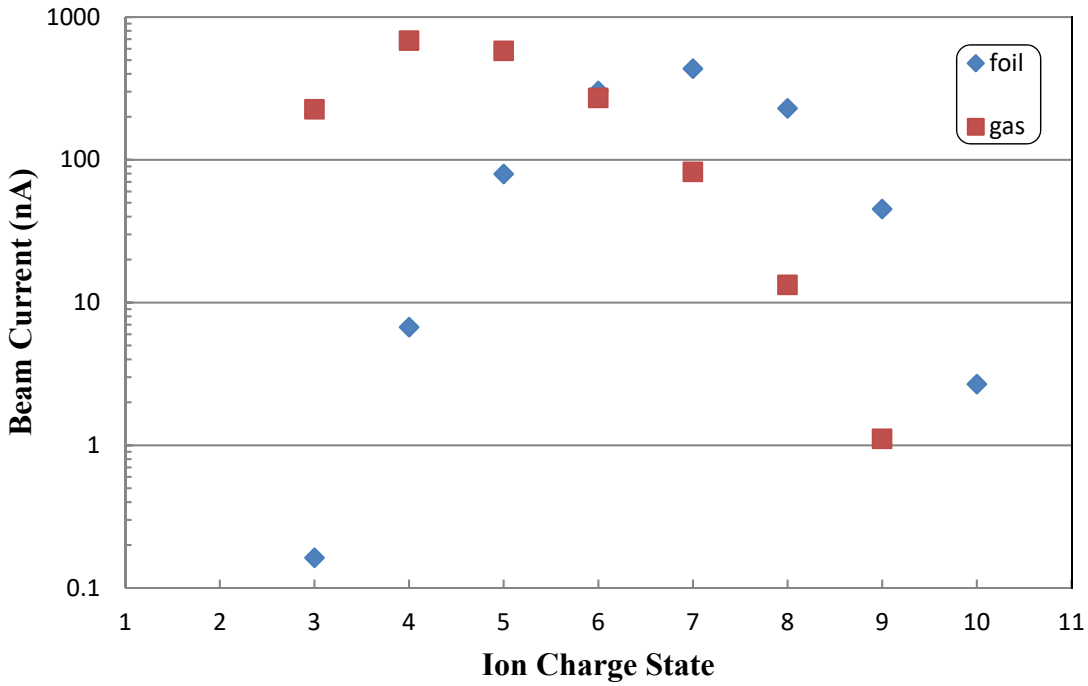

Fig. 1. Beam current vs. charge state of silicon ions measured for the terminal voltage of 6 MV.

Table 1 shows the summary of the acceleration tests of ion species in 2016 and 2017. For a given ion species, the charge states and energies of ion beams obtainable from the 6MV tandem accelerator are shown by the circular and triangular symbols. Other beam conditions with no symbols in Table 1 are not realized at UTTAC. For ion beams available at UTTAC, the maximum energy covered by the 6MV tandem accelerator is 90 MeV.

Table 1. Test results of acceleration of ion species at the terminal voltage of 6 MV in 2016 and 2017. The measured beam intensity is shown by the symbols: ○≥ 1nA and △≤1nA. Shown in red are the data obtained for foil strippers.

Charge	Energy	Ion Species													
State	(MeV)	He	Li	B	C	O	F	Si	Cl	Ni	Br	Ag	I	W	Au
14	90										△	△	○		△
13	84										○	△	○		△
12	78									△	○	○	○		○
11	72									○	○	○	○	△	○
10	66							○	○	○	○	○	○	△	○
9	60						○	○	○	○	○	○	○	○	○
8	54					○	○	○	○	○	○	○	○	○	○
7	48					○	○	○	○	○	○	○	○		
6	42					○	○	○	○	○	○	○			
5	36			△	○	○	○	○	○	○	○	○			
4	30			○	○	○	○	○	○	○	○				
3	24		○	○	○	○	○	○		○					
2	18	○	○	○	○	○	○								
1	12	○	○	○	○										

References

[1] M. Sataka et al., UTTAC Annual Report 2016, UTTAC-86 (2017) 9.

[2] Y. Tsuchiya et al., §5.2 of this UTTAC Annual Report 2017 (2018).

2.

NUCLEAR AND ATOMIC PHYSICS

2.1 Production of polarized unstable nuclei by using polarized proton beams

A. Ozawa, T. Moriguchi, Y. Yamato, M. Amano, D. Kamioka, S. Suzuki

We are attempting to produce polarized unstable nuclei by using polarized proton beams in the aim of measuring nuclear moments of unstable nuclei. Until FY2016, we have tried to produce unstable nuclei by target material including Mg and Si in 1 MV tandetron and 6 MV tandem accelerator [1].

In FY2017 we performed an experiment using polarized proton beams to check our nuclear magnetic resonance (NMR) system associated with beta-rays (beta-NMR system). Schematic view of our beta-NMR system is shown in Fig. 1. Polarized proton beams irradiate the target material. Beta-rays emitted from the produced unstable nuclei are detected by scintillation counters located up and down of the target material. To perform NMR, the static magnetic field (H_0) and the radio-frequency (RF) magnetic field which is perpendicular to H_0 are applied to the target material. To check the performance of our beta-NMR system, we tested a Si target with E_p = 12 MeV. We applied ~1.8 kG for H_0. In the previous measurement [2], polarized ^{29}P and ^{25}Al nuclei were produced and the magnetic moment of ^{25}Al was successfully measured. In the present work, the polarized proton beams accelerated to 12 MeV by the 6 MV tandem accelerator irradiated a 0.5 mm thick Si target placed in our beta-NMR system. Proton polarization degree in the ion source was about 70%. Figure 2 shows the time spectrum of beta-rays observed after irradiation of the polarized proton beams (about 20 nA beam intensity) for 10 seconds. The fitting results assuming half-lives of ^{29}P ($T_{1/2}$ = 4.2 s), ^{25}Al ($T_{1/2}$ = 7.2 s) and ^{30}P ($T_{1/2}$ = 150 s) are shown by a solid line in Fig. 2. In this measurement, we observed beta-ray asymmetry of up and down ratio deduced from the counts measured by the up and down beta-ray detectors. The symmetry is proportional to nuclear polarization degree created in the unstable nuclei. Presently the deduced asymmetry is 0.769(1) %, which is almost consistent with the observed asymmetry in the previous measurement [3]. Thus, production and detection of the nuclear polarization have been confirmed in our beta-NMR system. In the next step, we

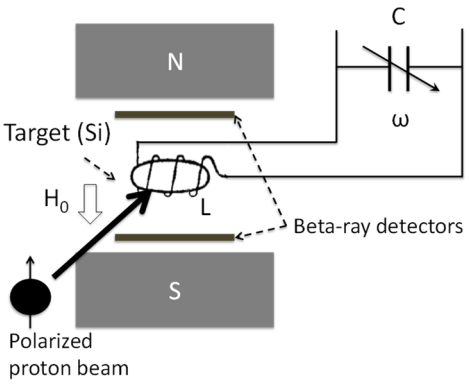

Fig. 1 Beta-NMR system. The system consists of a magnet (H_0), a LC resonance circuit, which provides RF with ω, and beta-ray detectors.

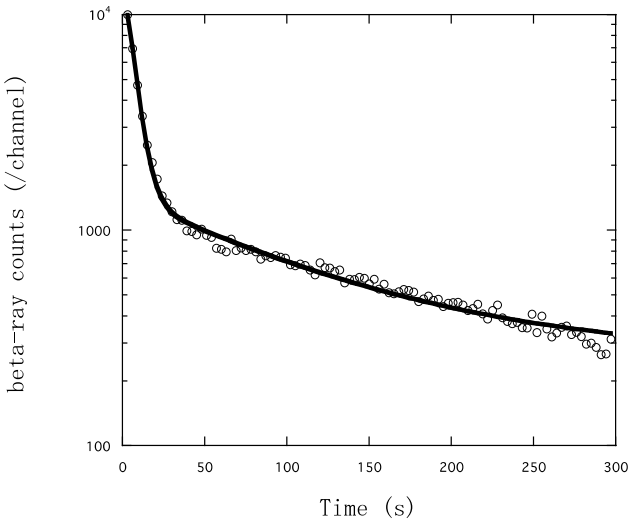

Fig. 2. Time spectrum of beta-rays in 12 MeV proton beam with a Si target. The solid line is the fitting result assuming half-lives of ^{29}P, ^{25}Al and ^{30}P.

will apply NMR to the polarized nuclei and confirm the magnetic moments of ^{25}Al and ^{29}P. The magnetic moment of ^{29}P will be compared with the published data [3].

References

[1] A. Ozawa et al., UTTAC Annual Report 2016 (2017) 11.

[2] T. Minamisono et al, Phys. Rev. C 14 (1976) 376.

[3] K. Sugimoto et al., in Hyperfine Interactions in Excited Nuclei, edited by G. Goldring and R. Kalish (Gordon and Breach, New York, 1971), p. 325.

2.2 Development of a position-sensitive detector using scintillating fibers

T. Yamaguchi[1,2], K. Wakayama[2], K. Nishimuro[2], T. Kobayashi[2], T. Moriguchi, A. Ozawa, S. Suzuki

We are developing a novel simple position readout method for a plastic scintillation counter for the Rare-RI Ring facility at the RI Beam Factory (RIBF) [1]. In high-energy RI beam facilities, well-established gas position-sensitive detectors, such as parallel plate avalanche counters (PPAC) [2], are used for beam diagnostics. As the Rare-RI Ring facility has many focal planes in an approximately 160-m-long injection beam line, numerous detectors are required for beam diagnostics. However, the operation and maintenance of such detectors can be expensive and often time-consuming. Thus, simple operation without complicated gas handling and expensive detectors is desired.

In the present study, we performed proof-of-principle experiments for a prototype detector. The prototype uses thin plastic scintillator bars and multi-pixel photon counters (MPPCs) for the scintillation light readout. This can also be used as a versatile diagnostics tool for small-intensity beams. We performed the detector test experiments[3] at the Heavy Ion Medical Accelerator in Chiba (HIMAC) facility [3] and at UTTAC. Using different beam species and energies, the detector performance was studied systematically.

The present prototype detector consists of 20 plastic scintillator bars (Eljen Technology EJ-200, $3 \times 3 \times 100$ mm^3) arranged to form a flat plane. Each end of the scintillator bars was connected to a common light guide bar ($3 \times 3 \times 120$ mm^3). The scintillation photons were read out by 4 MPPCs (Hamamatsu S12572-100C) through the light guides. The beam position can be obtained from the timing and charge differences of the scintillation light pulses propagated from each end of the light guide bars.

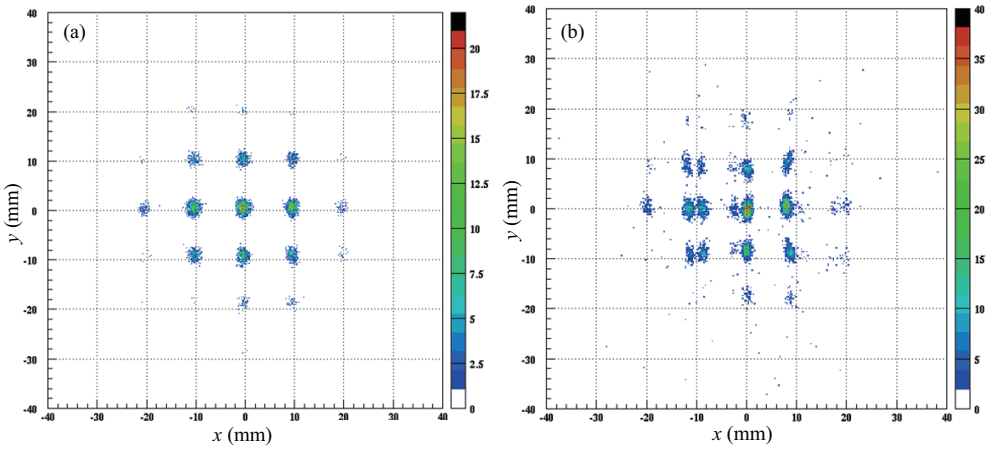

Fig. 1. Comparison of the two-dimensional beam profiles obtained (a) from PPAC, and (b) from the prototype detector (using the pulse timing differences). Certain beam spots are divided into two parts, because the particles passing through a hole hit two plastic scintillator bars [4].

A test experiment was carried out at HIMAC using a 200-MeV/nucleon ^{84}Kr beam. Two PPACs were used as references to calibrate the positions. We successfully obtained the beam position distributions

[1]Cross appointment
[2]Department of Physics, Saitama University
[3]condensed from the proceedings of the International Conference on Nuclear Physics at Storage Rings (STORI'17) [4]

from the prototype. The position resolution was 2–3 mm in σ, and the detection efficiency was close to 100%. A measurement was also carried out using a collimator to verify the resolutions. The collimator had holes of diameter 2 mm at intervals of 10 mm in the x- and y-directions. Figure 1 shows the typical beam profiles obtained (a) from PPAC, and (b) from the prototype detector. The collimated beam spots are separated well. In Fig. 1 (b), several beam spots are divided into two parts. This is because the ions that passed through a single hole hit two plastic scintillator bars.

At UTTAC, a 12-MeV proton beam from the 6MV tandem accelerator was used to test the response to a small energy deposit. The beam was irradiated onto a 2.5-μm-thick Au foil placed at the target chamber of the A7 course. The protons scattered at 30° were directed to the prototype detector. A position correlation is successfully observed as shown in Fig. 2, where the plotted ratios, $Q_{x\ \mathrm{ratio}}$ and $Q_{y\ \mathrm{ratio}}$, are sensitive to the x- and y-positions, respectively. In detail, they are calculated from the pulse height integrated values;

$$Q_{x\ \mathrm{ratio}} = \frac{Q^{\mathrm{up}}_{\mathrm{left}} - Q^{\mathrm{up}}_{\mathrm{right}} + Q^{\mathrm{down}}_{\mathrm{left}} - Q^{\mathrm{down}}_{\mathrm{right}}}{Q^{\mathrm{up}}_{\mathrm{left}} + Q^{\mathrm{up}}_{\mathrm{right}} + Q^{\mathrm{down}}_{\mathrm{left}} + Q^{\mathrm{down}}_{\mathrm{right}}}, \quad Q_{y\ \mathrm{ratio}} = \frac{Q^{\mathrm{up}}_{\mathrm{left}} - Q^{\mathrm{down}}_{\mathrm{left}} + Q^{\mathrm{up}}_{\mathrm{right}} - Q^{\mathrm{down}}_{\mathrm{right}}}{Q^{\mathrm{up}}_{\mathrm{left}} + Q^{\mathrm{down}}_{\mathrm{left}} + Q^{\mathrm{up}}_{\mathrm{right}} + Q^{\mathrm{down}}_{\mathrm{right}}}, \tag{1}$$

where the combinations of left, right, up, and down indicate the positions of MPPCs placed at the four corners of the detector. However, the resolution should still be improved. Notably, a series of developments performed at UTTAC and HIMAC facilities resolved the previously observed non-linear response between the positions and the pulse differences of the detector. Further developments are ongoing.

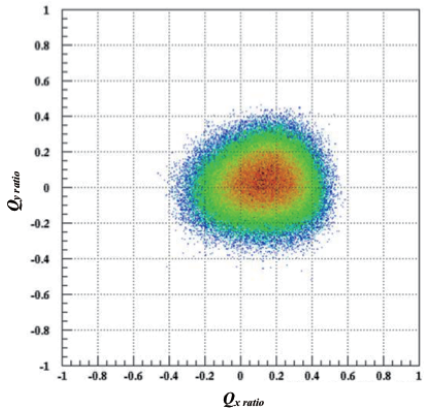

Fig. 2. Typical position correlation observed for the proton beam. $Q_{x\ \mathrm{ratio}}$ and $Q_{y\ \mathrm{ratio}}$ are given by eq. (1).

References

[1] A. Ozawa et al., Prog. Theo. Exp. Phys. 2012 (2012) 03C009.

[2] H. Kumagai et al., Nucl. Instrum. Methods Phys. Res. B 317 (2013) 717.

[3] M. Kanazawa et al., Nucl. Phys. A 746 (2004) 393c.

[4] K. Wakayama et al., JPS Conf. Proc., to be published.

2.3 Measurements for nitric acid produced by proton beam irradiation in a humidified air

Y. Nakai[1], S. Tomita, R. Suganuma, S. Hattori[2], K. Kobayashi[2], Y. Shiina, S. Ishino[2], N. Yamamoto, K. Sasa

Atmospheric chemical processes induced by galactic and solar cosmic rays and their influences on the atmosphere environments have attracted attentions in these days. Gas-phase nucleation induced by ionizing particles as cosmic rays has been discussed as one of important processes leading to cloud particle formation [1, 2]. In humidified gas involving a trace SO_2, generation of small droplets is enhanced by sulfuric acid formed by ionizing radiation [3]. Moreover, it is known that massive injection of ionizing particles into the atmosphere, such as solar proton events, causes an increase of the atmospheric nitric acid being a main reservoir of nitrogen oxides [4]. Thus, through laboratory studies of formation of nitric acid and sulfuric acid by ionizing particles [5], one can potentially obtain helpful information of elementary chemical processes for understanding of atmospheric influences of cosmic rays. However, sufficient information has not been given experimentally yet. We have investigated formation processes of sulfuric acid and nitric acid induced by irradiation of protons. In 2017, we performed measurements of nitric acid produced by irradiation of a proton beam in humidified air.

The sample air was generated by mixing pure dry air and wet air produced by bubbling a pure air in an ultra-pure water. The humidity of the sample air was adjusted by controlling the mixing ratio between the wet and dry air with mass flow controllers and was monitored with a dew-point meter. The sample air was introduced into a borosilicate glass tube with a length of 25 cm, where its total flow rate was kept at 2.5 SLM (Standard Liters per Minute). The 6 MeV proton beam delivered from the 6MV Pelletron tandem accelerator at UTTAC was introduced into the glass tube through a polyimide-film window. The beam penetrated along the glass tube filled with the flowing sample air. The irradiated sample air was transported into the filter-pack instrument. Three kinds of filters were stacked in it along a gas flow for collection of gas-phase nitric acid and other species (Filter-pack method [5]). A polyamide membrane filter was used for collection of gas-phase nitric acid. The collected nitric acid on the filter was dissolved in a 40 mL ultra-pure water. The amount of nitric anion, NO_3^-, in the solution was measured with ion chromatography analysis. The amount of gas-phase nitric acid in the gas passing through the filter was estimated from those of NO_3^- in the solution by assuming the collection efficiency of 100%.

In Fig. 1, preliminarily results are shown for the concentrations of gas-phase nitric acid produced by the proton irradiation under the condition of 1 atm pressure, ~42 % relative humidity, and ~296 K temperature. The concentration was calculated by dividing the amount of estimated gas-phase nitric acid by a total volume of the air passing through the filter. The production of nitric acid is found to be almost proportional to the beam current. Items to be considered still remain, such as collection efficiency of gas-phase nitric acid. Further analysis and consideration are proceeding.

[1] RIKEN Nishina Center
[2] School of Materials and Chemical Technology, Tokyo Institute of Technology

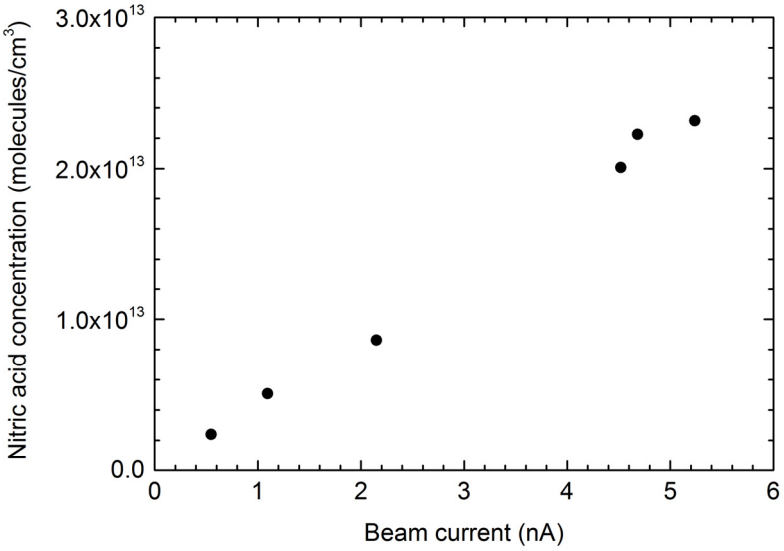

Fig. 1. Concentrations of gas-phase nitric acid in the proton-irradiated sample air versus beam currents (preliminary).

References

[1] J. Curtius et al., Space Sci. Rev. 125 (2006) 159.

[2] F. Arnold, Space Sci. Rev. 137 (2008) 225.

[3] S. Tomita et al., Nucl. Instr. Meth. Phys. Res. B 365 (2015) 616.

[4] B. Funke et al., Atmos. Chem. Phys. 11 (2011) 9089.

[5] M. B. Enghoff et al., Atmos. Chem. Phys. 12 (2012) 5319.

[6] Network Center for EANET, Technical Manual for Air Concentration Monitoring in East Asia (2013).

3.

ACCELERATOR MASS SPECTROMETRY

3.1 Operational status of the Tsukuba 6 MV multi-nuclide AMS system in fiscal 2017

K. Sasa, T. Takahashi, T. Matsunaka[1], S. Hosoya[2], M. Honda, Y. Ota, K. Takano, Y. Ochiai, M. Matsumura, K. Sueki

The AMS system on the 6 MV tandem accelerator was operated a total of 47 days in fiscal 2017. We measured 613 samples in total dealing with rare radionuclides such as ^{36}Cl, ^{41}Ca, ^{90}Sr and ^{129}I, as is summarized in Table 1. Figure 1 shows a breakdown of measured nuclides. Figure 2 shows monthly-measured nuclides from April 2017 to March 2018. ^{36}Cl was measured most frequently in the fiscal year 2017 in order to investigate the radiative contamination in rainwater and soil samples by the Fukushima Daiichi Nuclear Power Plant accident and the trace of cosmic ray events in the ice core.

Table 1. Number of samples measured in the fiscal year 2017.

Nuclides	Number
^{36}Cl	322
^{41}Ca	29
^{90}Sr	119
^{129}I	143
Total	613

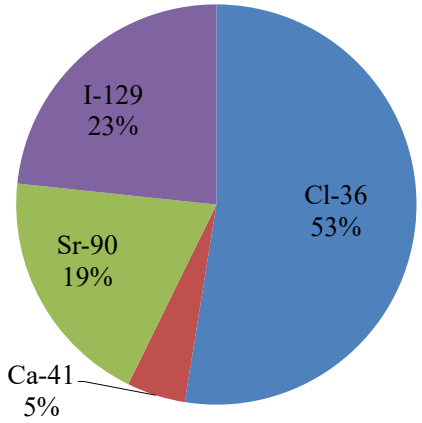

Fig. 1. Breakdown of the nuclides measured by the multi-nuclide AMS system in the fiscal year 2017.

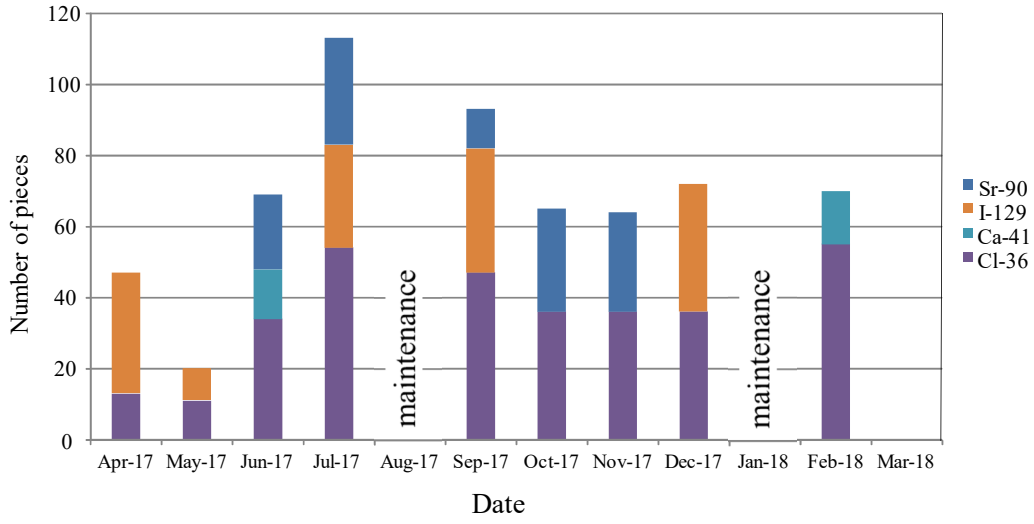

Fig. 2. Breakdown of the nuclides measured monthly by the multi-nuclide AMS system from April 2017 to March 2018.

[1] Kanazawa University
[2] The National Institutes for Quantum and Radiological Science and Technology (QST)

We have been developing ultrasensitive detection techniques for ^{41}Ca–AMS with the multi-nuclide AMS system. ^{41}Ca ($T_{1/2} = 1.04 \times 10^5$ yr) is produced by neutron capture of ^{40}Ca or spallation reactions in the primary targets. Accordingly, ^{41}Ca is an ideal tracer for dating the exposure age of meteorites and terrestrial surfaces. ^{41}Ca is also used for biomedical applications. The ion source can extract CaF_3^- beams up to 500 nA from CaF_2. We use the terminal voltage of 6.0 MV for ^{41}Ca–AMS. Carbon stripper foils (4.8 μg/cm^2) are used for ^{41}Ca–AMS to obtain highly charged ions. We tried to detect a charge state of $^{41}Ca^{5+}$ with a total energy of 32.5 MeV in 2017. The beam transmission of $^{41}Ca^{5+}$ was about 7 %. A multi-plate gas-ionization detector was employed to separate ^{41}Ca spectrum from isobaric interferences of ^{41}K. Figure 3 shows two dimensional spectra for a blank sample and a standard sample of ^{41}Ca/Ca = 1.155×10^{-10}. Figure 4 shows the calibration curve for ^{41}Ca measurements with 6 standard samples [3]. We obtained a background level of ^{41}Ca/Ca down to about 3×10^{-15} and a measurement precision of 3% for 9.76×10^{-12} isotopic ratio using the multi-nuclide AMS system.

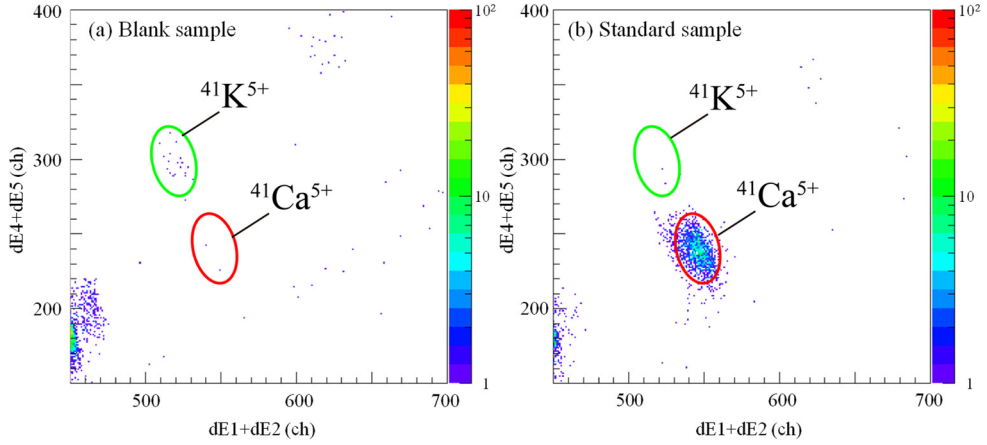

Fig. 3. Two-dimensional spectra of ^{41}Ca–AMS measured with the five-anode ΔE–E gas ionization detector and measuring time of 5 min. (a) Blank sample. (b) Standard sample of ^{41}Ca/Ca = 1.155×10^{-10}.

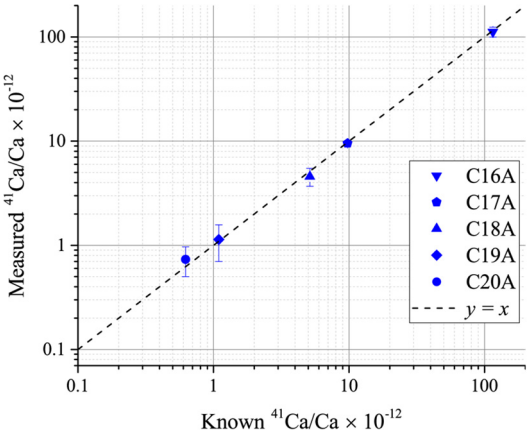

Fig. 4. Calibration curve for ^{41}Ca measurements of standard samples [3].

References

[1] K. Sasa et al., Nucl. Instr. Meth. Phys. Res. B 361 (2015) 124.

[2] S. Hosoya et al., Nucl. Instr. Meth. Phys. Res. B 406 (2017) 268.

[3] K. Nishiizumi et al., Nucl. Instr. Meth. Phys. Res. B 172 (2000) 399.

3.2 Temporal variation of ^{36}Cl in monthly precipitation at Tsukuba before and after the FDNPP accident

Y. Ochiai, K. Sasa, Y. Tosaki[1], T. Takahashi, M. Matsumura, S. Hosoya, K. Takano, Y. Ota, K. Sueki

On March 11, 2011, the Great East Japan Earthquake and the subsequent tsunami damaged the Fukushima Daiichi Nuclear Power Plant (FDNPP). A large number of radionuclides including ^{131}I and ^{134}Cs were released to the environment. ^{36}Cl was also one of the nuclides released from the FDNPP accident, which was expected to be produced by a nuclear reaction of neutron and ^{35}Cl in the coolant, i.e., ^{35}Cl (n, γ) ^{36}Cl. However, little is known about the total released amount or behavior of ^{36}Cl in the environment because of the difficulty in its detection. This report focuses on the temporal variation of ^{36}Cl in precipitation derived from the FDNPP accident by the measurement of ^{36}Cl / Cl.

We collected rainwater samples monthly from January 2010 to December 2012 at the University of Tsukuba. Cl^- in rainwater was extracted using the ion exchange method and precipitated as AgCl with 0.3 M $AgNO_3$. The precipitation was washed with ultrapure water and ethanol, and was loaded with a sample holder. Measurements of ^{36}Cl were conducted with AMS at UTTAC [1]. The background level of the system for ^{36}Cl-AMS is ^{36}Cl / Cl = 3×10^{-15}, which is the lowest one obtained in Japan. Some parameters for ^{36}Cl-AMS were as follows: the terminal voltage of 6.0 MV, the detected ion of $^{36}Cl^{8+}$ (56.0 MeV), and the measurement time of 300 seconds × 8 times per one sample.

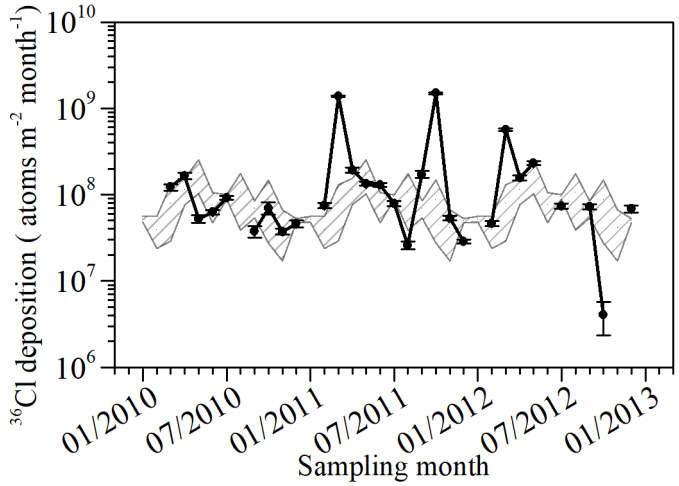

Fig. 1. The temporal variation of ^{36}Cl in monthly precipitation. The hatched area shows the monthly average of ^{36}Cl from April 2004 to December 2009.

Figure 1 shows the variation of ^{36}Cl in the monthly precipitation at Tsukuba. The amount of ^{36}Cl in precipitation in March 2011 was $(1.38 \pm 0.02) \times 10^9$ atoms m^{-2} month^{-1} which was 17 times higher than the average in March from 2005 to 2009, $(8.0 \pm 5.1) \times 10^7$ atoms m^{-2} month^{-1} [2]. The result was presumed to be caused by the FDNPP accident because there is no similar data before March 2011 and

[1] Geological Survey of Japan, AIST

recent studies reported the release of ^{36}Cl by the FDNPP accident [3]. The amount of ^{36}Cl in precipitation in October 2011 was (1.49 ± 0.04) × 10^{9} atoms m^{-2} $month^{-1}$ which was higher than the amount of ^{36}Cl in precipitation in March 2011. However, we have not clarified the cause and further investigation is necessary.

Figure 2 shows comparison of the variation of ^{36}Cl in monthly precipitation with that of ^{129}I [4] from September 2010 to February 2012. It is found that ^{36}Cl correlates strongly with ^{129}I from April to September 2011 (correlation number r = 0.7). Therefore, the behavior of ^{36}Cl is considered to be similar to that of ^{129}I in the environment. In March 2011, the ratio of deposition of the two nuclides is ^{129}I / ^{36}Cl = 3.1 × 10^{3}. In addition, the total amount of ^{129}I released from the FDNPP accident is estimated to be 8.1 GBq, according to recent investigations [5]. Assuming that ^{36}Cl emitted from the FDNPP accident was transported and deposited in the same way as ^{129}I, the total amount of released ^{36}Cl is estimated to be 0.14 GBq. It is presumed that ^{36}Cl has relatively a small impact on the environment because its amount of emission is 8–9 orders of magnitude less than that of ^{131}I (151 PBq) [6] or ^{137}Cs (14.5 PBq) [6] which possibly cause serious effects on human bodies.

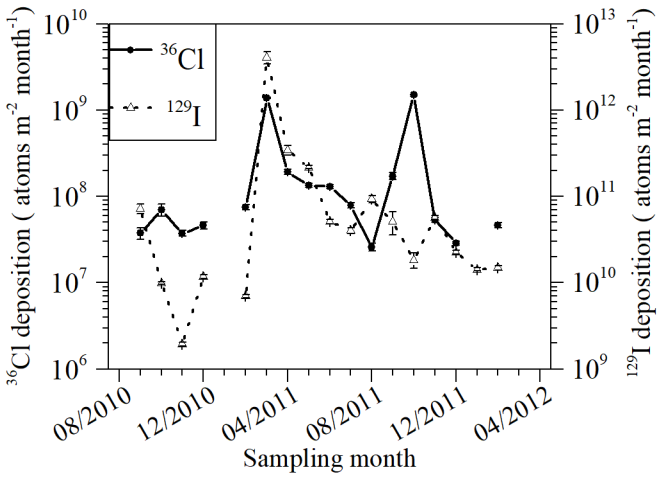

Fig. 2. Comparison of ^{36}Cl and ^{129}I in monthly precipitation.

References

[1] K. Sasa et al., Nucl. Instrum. Meth. Phys. Res. B 361 (2015) 124.

[2] Y. Tosaki et al., J. Environ. Radioactiv. 106 (2012) 73.

[3] Y. Miyake et al., Nucl. Instrum. Meth. Phys. Res. B 361 (2015) 627.

[4] M. Matsumura et al., Geochem. J. 52(2) (2018) 155.

[5] X. Hou et al., Environ. Sci. Technol. 47(7) (2013) 3091.

[6] G. Katata et al., Atom. Chem. Phys. 15 (2015) 1029.

3.3 ^{36}Cl record in the Antarctic ice core around the cosmic-ray event of 5480 BC studied with ^{36}Cl AMS

K. Takano, K. Sasa, T. Takahashi, Y. Tosaki[1], S. Hosoya, Y. Ota, Y. Ochiai, K. Sueki, K. Horiuchi[2]

Cosmic rays are high energy particles that come to the earth from the outside solar system. They interact with atoms and molecules in the atmosphere, which is responsible for the production of cosmogenic nuclides such as ^{14}C, ^{10}Be, ^{26}Al and ^{36}Cl. Therefore, the concentration of cosmogenic nuclides reflects the intensity of cosmic rays. Miyake et al. [1] measured ^{14}C contents in pine tree rings with 1- to 2-year time resolution for the period from 5490 BC to 5411 BC, and found a large ^{14}C increase around 5480 BC. To further investigate the cause of the increase, we tried to detect such a cosmic ray event by measuring cosmogenic ^{36}Cl in ice core samples from the Dome Fuji, Antarctica. ^{36}Cl is produced in the atmosphere by the spallation reaction of incoming cosmic rays with ^{40}Ar, and it falls down and deposits in the ice core.

For detection of cosmic-ray events in the Antarctic ice core, high time-resolution records are required together with measurements of the ^{36}Cl/Cl ratio on the order of 10^{-14}. Therefore, we needed to improve isobar (^{36}S) separation techniques for high sensitivity ^{36}Cl measurements with the 6 MV AMS system at UTTAC [2]. We tried to use AgBr as the backing material in sample holders in order to reduce interferences of ^{36}S [3]. The AgBr materials were prepared under different chemical processing conditions in order to compare the effect of ^{36}S elimination. We added either concentrated HNO_3 or NH_4OH to saturated KBr solution. In this report, we refer to the former as the acid condition and the latter as the alkaline condition. Then, AgBr was precipitated with saturated $AgNO_3$. Finally AgBr were centrifuged and washed with ultrapure water and ethanol. Table 1 shows the result of the measurements for the three cases .We obtained the lowest isobar (^{36}S) interference with AgBr precipitated under the acid condition.

Table 1. Comparison of isobar contribution with AgBr materials prepared under different conditions. The counts of ^{36}S are normalized to the ^{35}Cl current value.

	AgBr-reagent	AgBr-alkaline	AgBr-acid
^{36}S / ^{35}Cl	2.31 ± 0.47	2.16 ± 0.26	0.49 ± 0.22

Owing to the improved ^{36}Cl-AMS, ^{36}Cl / Cl ratios on the order of 10^{-14} can be measured with high precision. We thereby measured ^{36}Cl concentrations in the Dome Fuji ice core around the 5480 BC event. The depth interval of each sample is 50 cm which corresponds to about 20 year interval. We added ~0.75 mg of Cl carrier to each sample (approximately 90-180 g in weight), which resulted in measured ^{36}Cl / Cl ratios of 2.04×10^{-14}–13.5×10^{-14} around the 5480 BC event. Figure 1 shows the variation of the ^{36}Cl

[1] Geological Survey of Japan, AIST
[2] Hirosaki University

concentrations which ranges from 0.3 × 10^4 to 1.1 × 10^4 atoms g^{-1}. There is a small increase in the concentration of ^{36}Cl around 5480 BC. Further studies should include measurements of cosmogenic nuclides of ^{10}Be and ^{36}Cl with higher time resolution in order to reveal the origin of cosmic rays around the 5480 BC event.

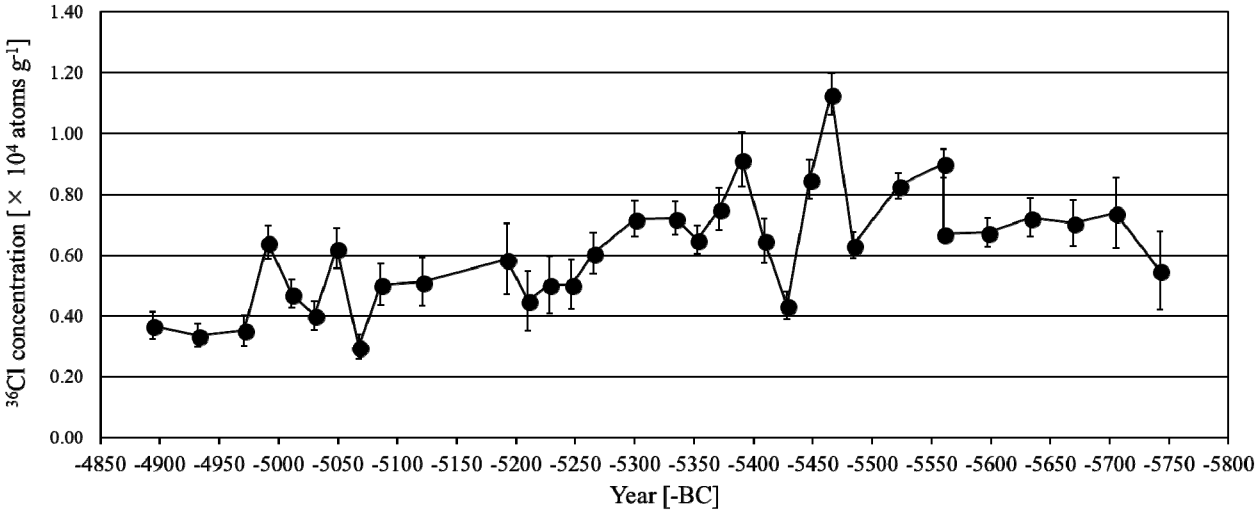

Fig. 1. Measured results of ^{36}Cl concentration.

References

[1] F. Miyake et al., PNAS 114 (2017) 881.

[2] K. Sasa et al., Nucl. Instr. Meth. Phys. Res. B 361 (2015) 124.

[3] S. Hosoya et al., UTTAC Annual Report 2016, UTTAC-86 (2017) 18.

3.4 Depth profile of ^{36}Cl in the soil at Fukushima after the Fukushima Dai-ichi Nuclear Power Plant accident

Y. Ota, K. Sueki, K. Sasa, T. Takahashi, T. Matsunaka[1], M. Matsumura, Y. Satou[2], S. Hosoya, K. Takano, Y. Ochiai

In the environment, ^{36}Cl ($T_{1/2}$ = 3.01 × 10^5 yr), the major radioisotope of chlorine, is mainly produced by the reaction ^{40}Ar (p, 2p3n) ^{36}Cl as a cosmogenic nuclide. In addition, nuclear weapon tests at oceanic sites between 1952 and 1958 led to the release of large amounts of artificial ^{36}Cl into the atmosphere. Before the Fukushima Dai-ichi Nuclear Power Plant (FDNPP) accident, ^{36}Cl remained as a tracer in the soil. We had measured ^{36}Cl/Cl continuously by the former AMS system at UTTAC until 2011 [1–3]. The ratio of ^{36}Cl/Cl in the surface soil varied in the range of (0.09–4.10) × 10^{-13} at Futaba- and Okuma-machi, Fukushima in 2008 and 2009 [3]. After the FDNPP accident, the ^{36}Cl/Cl ratios were (0.11–2.63) × 10^{-11} for the surface soil samples collected at 10 sites around the FDNPP on April 20, 2011 [4]. The pronounced increase of ^{36}Cl is probably due to the FDNPP accident. For further investigations, we measured ^{36}Cl/Cl by the new AMS system at UTTAC [5]. The ratios of ^{36}Cl/Cl were obtained in the range of (0.01–1.00) × 10^{-11} from the surface soil samples collected at 31 sites around the FDNPP from June 2013 to November 2016. The measurements of 10 sites were reported in 2016 [6]. Meanwhile, it was believed that chlorine is non-reactive and moves simply with water in the soil. Measurements of the surface soil might not be enough for revealing the deposition density of ^{36}Cl released from the FDNPP accident. Thus, we obtained the depth profile of ^{36}Cl in the soil at Fukushima to investigate the movement of ^{36}Cl.

We collected 30-cm-long soil cores at Namie-machi, Fukushima (37° 33′ 39″E, 140° 49′ 41″N) on June 2013 and September 2017. Soil cores were sliced into the thicknesses of 0.7 to 4 cm. The subdivided soil samples were vacuum-freeze-dried and sieved through 2 mm mesh. Fractions of less than 2mm were pulverized by an agate ball mill (200 rpm, 15 min × 3 times). Then, we obtained the concentrated solution of $^{36}Cl^-$ following the sample preparation scheme (Fig. 1) designed with reference to Tamari (2009), Amano (2011) and Bastviken et al. (2007) [2, 3, 7]. Then, we conducted

Fig. 1. Sample preparation scheme to extract $^{36}Cl^-$.

[1] Kanazawa University
[2] Japan Atomic Energy Agency (JAEA)

the operation to remove ^{36}S that interferes ^{36}Cl-AMS, and prepared as AgCl. The detailed procedure is described elsewhere [6]. The ^{36}Cl/Cl ratio was measured by the AMS system. The terminal voltage for acceleration was 6.0 MV and the detected ion was $^{36}Cl^{8+}$. The measured ^{36}Cl/Cl ratios were normalized by using the ^{36}Cl standard (^{36}Cl/Cl = 5.00×10^{-13}) developed by Sharma et al. [8].

Figure 2 shows the depth profiles of ^{36}Cl/Cl, $^{36}Cl^-$ and Cl^- concentrations in 2013 and 2017. The ^{36}Cl/Cl ratios ranges from 10^{-12} to 10^{-11}. In comparison with the ^{36}Cl/Cl ratio before the FDNPP accident, the ^{36}Cl/Cl ratios are high not only near the surface, but also even at a depth of 5 cm or more. This fact indicates that ^{36}Cl released from the FDNPP accident deposited into the soil and moved downward until 2013. Therefore, it is very difficult to determine the deposition density of $^{36}Cl^-$ using the surface soil. Meanwhile, recent study has shown that Cl^- is converted into chlorinated organic compounds (Cl_{org}) [5]. It has been implied that more than 40% of the total Cl in the surface soil are Cl_{org} in the boreal and temperate zones [9]. For this reason, the depth profile of $^{36}Cl_{org}$ is required. If ^{36}Cl released from the FDNPP accident is converted into $^{36}Cl_{org}$ and retained in surface soil, we may estimate the deposition density of total ^{36}Cl (= $^{36}Cl^-$ + $^{36}Cl_{org}$) instead of $^{36}Cl^-$.

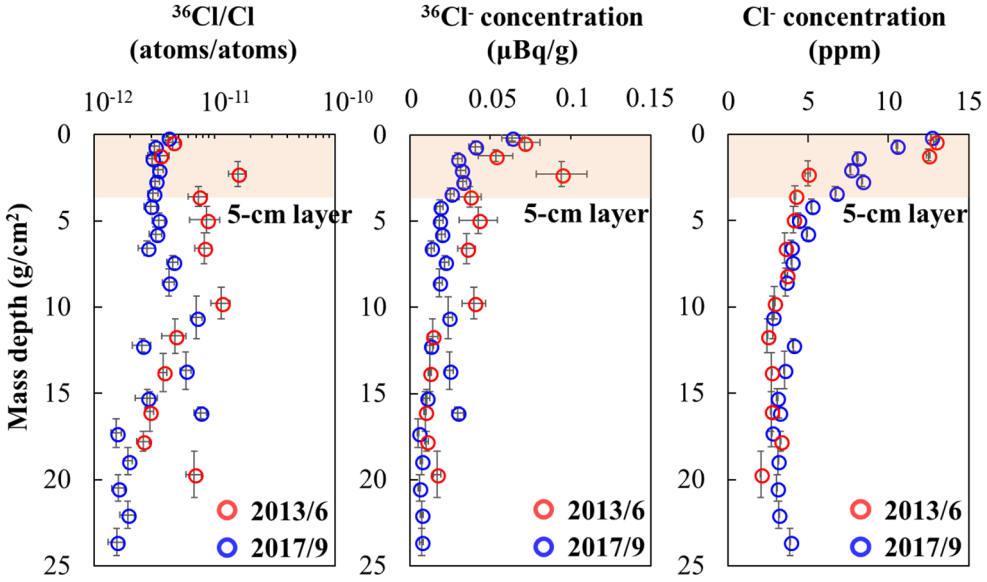

Fig. 2. Depth profiles of ^{36}Cl/Cl, $^{36}Cl^-$ concentration and Cl^- concentration in soil at Namie-machi, Fukushima (37° 33′ 39″E, 140° 49′ 41″N) on June 2013 and September 2017.

References

[1] R. Seki et al., Nucl. Instr. Meth. Phys. Res. B 259 (2007) 486.

[2] M. Tamari, Master's thesis, University of Tsukuba 2009 (in Japanese).

[3] T. Amano, Master's thesis, University of Tsukuba 2011 (in Japanese).

[4] Y. Miyake et al., Nucl. Instr. Meth. Phys. Res. B 361 (2015) 627.

[5] K. Sasa et al., Nucl. Instr. Meth. Phys. Res. B 361 (2015) 124.

[6] Y. Ohta et al., UTTAC Annual Report 2016 (2017) 20.

[7] D. Bastviken et al., Geochimica et Cosmochimica Acta 71 (2007) 3182.

[8] P. Sharma et al., Nucl. Instr. Meth. Phys. Res. B 52 (1990) 410.

[9] D. Bastviken et al., SKB TR-13-26 (2013).

3.5 Anthropogenic iodine-129 in the Japan Sea Bottom Water in 2017

T. Matsunaka[1], S. Nagao[1], M. Inoue[1], S. Ochiai[1], T. Morita[2], S. Miki[2], T. Aramaki[3], I. Kudo[4], N. Honda[2], T. Takikawa[5], K. Sueki, M. Honda, K. Sasa

The Japan Sea is a semi-enclosed deep marginal sea in the northwestern North Pacific with the maximum depth of ~3700 m. The sea is one of the reservoirs and monitors for emitted anthropogenic pollutants such as radionuclides from nuclear activities and hazardous organics from human activities. The Japan Sea has surface subtropical and subarctic circulations and has deep convection system of the Japan Sea Bottom Water (JSBW). The long-term observation revealed that warming and oxygen decrease of the JSBW respond sensitively to air temperature raise in winter [1]. The relatively wide range of turnover time for the JSBW were estimated to be 75–380 years detecting bomb-derived ^{14}C [2–3]. Further investigation of water dynamic in the Japan Sea using radioactive tracer is of essential importance not only for elucidating the interaction between climate change and the convection system, but also for understanding the behavior of the marine pollutants.

Anthropogenic ^{129}I ($T_{1/2}$ = 15.7 million years) produced from the thermal neutron fission of ^{235}U and ^{239}Pu is released dominantly by nuclear fuel reprocessing plants in the northwestern Europe. Less radiologically harmful ^{129}I provides information about the deep ventilation of sea water in the North Atlantic. The main pathway of such pollutants to reach the Japan Sea is considered to be atmospheric transportation from the northwestern Europe, especially for ^{129}I [4]. The main objective of this study is to illuminate the availability of ^{129}I as a tracer of surface circulations and vertical convections in the Japan Sea and Okhotsk Sea. Therefore, we investigated the horizontal and vertical distributions of ^{129}I in the large area of these seas in 2017.

The radioactivity of dissolved ^{129}I in surface water varied from 17.3 ± 0.7 to 23.1 ± 1.0 nBq L^{-1} at the area of 38–46ºN and 135–141ºE in the Japan Sea, and was negatively correlated with salinity (R^2 = 0.82), as shown in Fig. 1. This salinity-dependent distribution indicates that the dissolved ^{129}I concentration in the area is controlled by mixing of water mass from the Liman Current with low salinity to the Tsushima Current with high salinity. Meanwhile, the mean radioactivity of dissolved ^{129}I in the JSBW observed at the layer of 2480–3500 m of the Japan Basin in 2017 was 4.1 ± 0.5 nBq L^{-1}, which increased by 1.1 nBq L^{-1} from that in 2007 [5] (Fig. 2). The turnover time for the JSBW 205 ± 25 years, estimated using ^{129}I, is consistent with the literatures [2, 3]. These results demonstrate that ^{129}I is a useful tracer for study of the surface subarctic front and deep JSBW in the Japan Sea.

[1] Kanazawa University
[2] Japan Fisheries Research and Education Agency
[3] National Institute for Environmental Studies
[4] Hokkaido University
[5] Nagasaki University

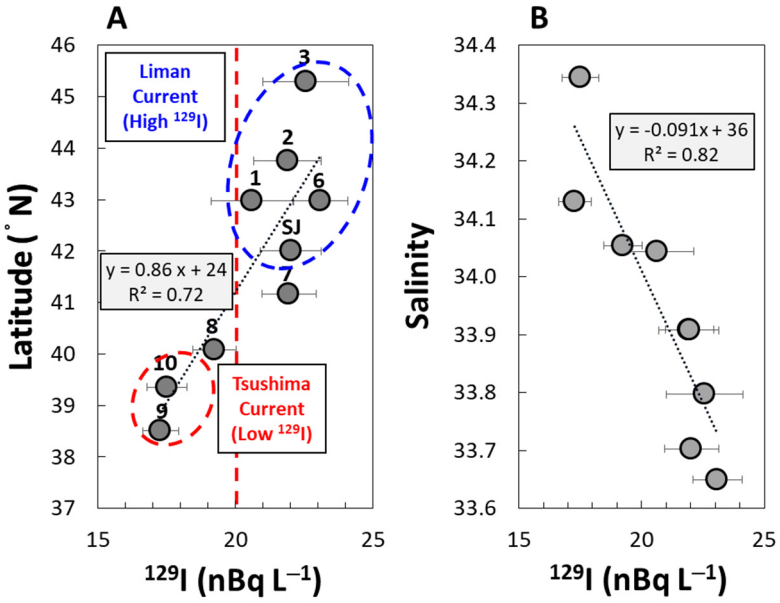

Fig. 1. Correlations between ^{129}I radioactivity in sea water from the Japan Sea and latitude (A) and salinity (B). The linear regression lines and the coefficient of determination R^2 are shown in the diagrams.

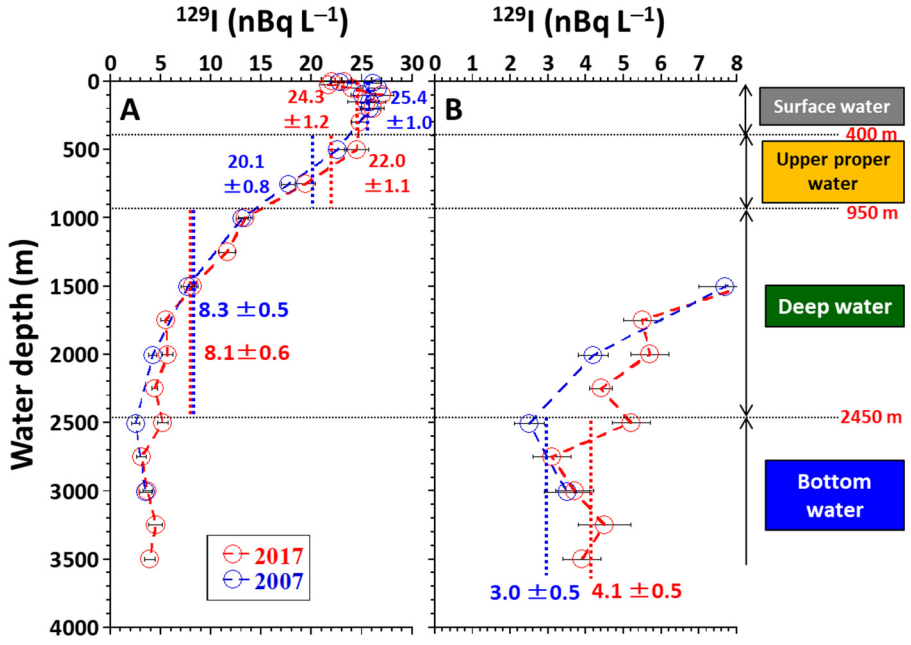

Fig. 2. Vertical distributions of ^{129}I in the Japan Basin observed in 2007 [5] and 2017 (this study). The boundaries of surface water, upper proper water, deep water, and bottom water are shown on the right. (B) shows the laterally enlarged diagram of (A).

References

[1] T. Gamo, Trends Anal. Chem. 30 (2011)1308.

[2] T. Gamo, Y. Horibe, J. Oceanogr. Soc. Japan 39 (1983) 220.

[3] Y. Kumamoto et al., J. Oceanogr. Soc. Japan 64 (2008) 429.

[4] T. Suzuki et al., Nucl. Instr. Meth. Phys. Res. B 294 (2013) 563.

[5] T. Suzuki et al., Nucl. Instr. Meth. Phys. Res. B 268 (2010) 1229.

3.6 Development of the prompt and sensitive determination method for strontium-90 with accelerator mass spectrometry

S. Hosoya[1], K. Sasa, M. Honda, T. Takahashi, Y. Satou[2], K. Takano, Y. Ochiai, K. Sueki

Strontium-90 (^{90}Sr; $T_{1/2}$ = 28.79 yr) is a radioactive nuclide (β^- decay) and the fission product of uranium and plutonium. In fact, ^{90}Sr was discharged into environmental by the Fukushima Daiichi Nuclear Power Plant accident. Strontium is the same alkaline earth metal as calcium and its chemical properties are similar. When ^{90}Sr is taken into the body, it accumulates in the bone and causes internal exposure. The ^{90}Sr measurement is important for understanding the behavior of radioactive nuclides in environment and in vivo. A conventional analysis method of ^{90}Sr is the β decay counting. However, β decay counting requires the milking process of ^{90}Y. It is easier to measure the β ray from ^{90}Y (2.28 MeV) than from ^{90}Sr (0.54 MeV). It takes two or three weeks to wait for the ^{90}Y growth until the radioactive equilibrium is reached. Recently, the ICP-QMS technique was developed for a rapid analysis of ^{90}Sr [1]. However, its detection limit is rather insufficient. Meanwhile, AMS has a great potential to enable quick and high-sensitivity measurement of ^{90}Sr.

Table 1. Comparison of ^{90}Sr analysis methods.

	β decay counting	ICP-QMS	AMS
Detection limit	~ 1 mBq	~ 20 mBq	~ 0.1 mBq (^{90}Sr/Sr ~ 10^{-14})
Analysis time	60 min.+ Milking 2–3 weeks	~ 15 min.	~ 30 min.

The ^{90}Sr analysis methods are compared in Table 1.

The ion source for AMS is of cesium sputtering type. Because strontium is alkaline earth metal element, as mentioned above, the electron affinity is low so that the negative ion beam of strontium cannot be obtained from the sputtering ion source. Hence we tried to extract molecular ion beam of negatively charged SrF_2. The non-conductor SrF_2 was mixed with some conductive powder to suppress electrical charging. Test results of beam extraction is listed in Table. 2. $^{88}SrF_3^-$ could be successfully extracted up to ~ 400 nA from the mixed powder of SrF_2 and PbF_2.

Table 2. Extracted $^{88}SrF_3^-$ currents from various mixtures of SrF_2.

Mixed powder (SrF_2: others)	$^{88}SrF_3^-$ current (nA)
PbF_2 (1:4)	~ 400
Au (1:4)	~ 300
Au (1:1)	~ 150
Ta (1:4)	~ 100

The standard sample of high reliability is important for AMS to determine the quantity of an unknown sample. We used the standard sample prepared from the Proficiency Test sample (PT sample). The PT samples are distributed from IAEA and used as mutual evaluation sample at AMS facilities all over the world. These samples are suitable for AMS because the reliable values are given by IAEA. The standard sample was prepared by diluting the PT sample to an arbitrary ratio and making it according to the process shown in Fig. 1. We prepared three standard samples of ^{90}Sr/Sr = 3.38×10^{-9}, 4.14×10^{-10}, and 1.75×10^{-10}.

Table 3 shows the system parameters of ^{90}Sr AMS at UTTAC. The detector used is of 5-anode gas

[1] Present address: The National Institutes for Quantum and Radiological Science and Technology (QST)
[2] Japan Atomic Energy Agency (JAEA)

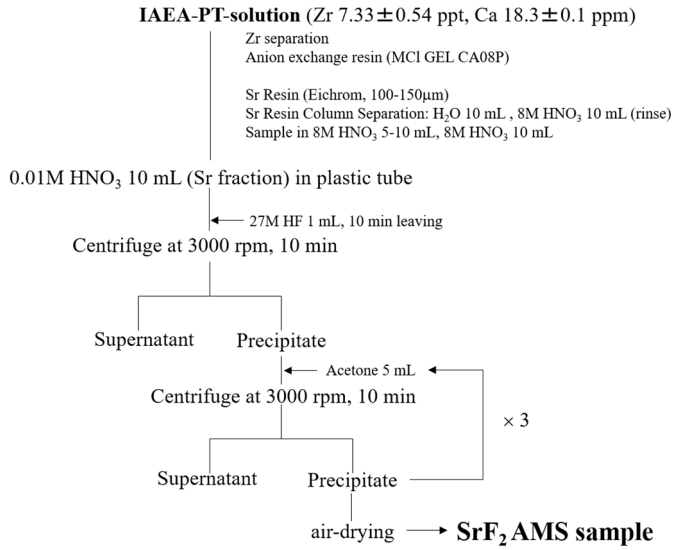

Fig. 1. ^{90}Sr-AMS standard sample preparation scheme.

Table 3. System parameters of UTTAC ^{90}Sr AMS.

Sample material	SrF_2
Extracted beam	$^{88}SrF_3^-$ (~ 400 nA)
Terminal voltage	6 MV
Stripper	Carbon foil (3.8 μg/cm^2)
Detected ion	$^{90}Sr^{8+}$
Transmission	~ 8 %
Beam energy	51.8 MeV
Detector gas	Isobutane
Detector window	Si_3N_4 (75 nm)

ionization type. Details of the detector setup and the isobar (^{90}Zr) separation technique are described in Ref. [2]. $^{90}Sr^{8+}$ could be detected at 30 Torr of the detector gas of isobutane, as is seen in Fig. 2.

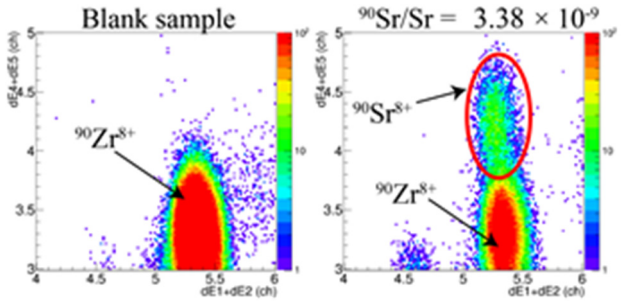

Fig. 2. AMS results for the standard sample (^{90}Sr/Sr = 3.38 × 10^{-9}) and the blank sample (commercial reagent) spectra.

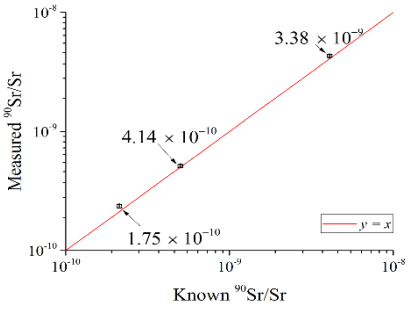

Fig. 3. Measured ratios of ^{90}Sr/Sr for the standard samples vs. the known ratios for the PT sample.

Results of the measurements for the 3 standard samples are plotted against the known ratios for the PT sample in Fig. 3, which assures consistency of the whole experimental procedure. The background level was measured by using the blank sample (commercial reagent) and its level of ^{90}Sr/ Sr ~ 6 × 10^{-13} (equivalent to ^{90}Sr ~ 3 mBq) has been obtained. Until now, Lawrence Livermore National Laboratory has been the only facility that allows AMS measurements (using the 10 MV tandem accelerator) of ^{90}Sr with the same background as the level above [3]. In this research, the world's highest-level performance has been achieved at UTTAC. The present work has demonstrated the prompt and sensitive analysis of ^{90}Sr using our AMS, compared with the conventional ^{90}Sr analysis method.

References

[1] Y. Takagai et al., Analytical Method 6 (2014) 355.

[2] S. Hosoya et al., UTTAC Annual Report, UTTAC-85 (2016) 17.

[3] S. J. Tumey et al., Journal of Radioanalytical and Nuclear Chemistry 282 (2009) 821.

3.7 Trial of determination of ^{41}Ca in stony meteorites by accelerator mass spectrometry

Y. Oura[1], T. Hara[1], S. Hosoya, K. Takano, Y. Ochiai, T. Takahashi, K. Sueki, K. Sasa

Chlorine-36 and ^{41}Ca are cosmogenic radionuclides found in meteorites and produced by several nuclear reactions such as proton and secondary neutron induced spallation reactions and neutron capture reaction. We determined ^{36}Cl concentrations in chondrites and iron meteorites by accelerator mass spectrometry (AMS) system at UTTAC to study irradiation histories of meteorites. In 2016 we tried to determine ^{41}Ca concentration in iron meteorite by using a new AMS system at UTTAC [1]. In 2017 we tried to determine ^{41}Ca concentration in stony meteorites by AMS.

In mass spectrometry including AMS, isobars sometimes interfere in the determination of nuclide of interest. Stony meteorites contain more K (^{41}K) than iron meteorites (containing almost no K). Using a radiotracer, a chemical separation procedure for Ca in stony meteorites was evaluated especially for removal of K. The evaluated procedure was applied to two stony meteorites, Gao and Dajala meteorites, and their ^{36}Cl concentrations and elemental concentrations were determined by the former AMS system at UTTAC [2] and a neutron activation analysis, respectively.

About 0.1 g of powdered samples was dissolved in dil. HNO_3 after an alkali fusion with Ca carrier (5 – 10 mgCa) and Cl carrier (2 – 4 mgCl). $AgNO_3$ was added to precipitate AgCl. Ammonia water was added to the supernatant solution to adjust pH into 5.4 – 5.8, then $Fe(OH)_3$ was precipitated. Also, CaC_2O_4 was precipitated by adding $(NH_4)_2C_2O_4$ in the supernatant solution followed by dissolution of CaC_2O_4 in 6 mol/L HCl. Remained trace Fe in this solution was removed by anion exchange method, and then CaF_2 was finally obtained by adding HF to the eluate containing Ca. Although CaF_2 was heated at 500°C for determination of ^{41}Ca in iron meteorites in 2016, CaF_2 was heated at 110°C overnight in this study. Final Ca fractions were divided into halves, and both halves were subjected to AMS measurement independently. Additionally reagent blank and procedure blank were also determined.

In AMS measurement of ^{41}Ca, the terminal voltage of the tandem accelerator was set to 6 MV and $^{41}Ca^{5+}$ and $^{40}Ca^{5+}$ were measured for about 3000 sec (10 times of 300 sec) or 5000 sec by gas ionization detector and Faraday cup, respectively (in 2016 Ca^{7+} was measured similarly). The calibration curve obtained is shown in Fig. 1 and good correlation between the ^{41}Ca / ^{40}Ca count ratio and the certified ^{41}Ca / ^{40}Ca atomic ratio is observed. The results for stony meteorites are tabulated in Table 1. In stony meteorites ^{41}K / ^{40}Ca content atomic ratio is about 0.006 whereas the detected ^{41}K / ^{40}Ca count ratios are about 1×10^{-8}. Although the detected counts of ^{41}K were greater than of ^{41}Ca, K was removed enough to detect ^{41}Ca. Determined ^{41}Ca concentrations in two portions (A and B) for the two meteorites demonstrate good reproducibility of the present measurements of ^{41}Ca / ^{40}Ca.

For Dajala meteorite, in which ^{36}Cl concentration is 16 dpm/kg, about 100 counts of ^{41}Ca was obtained, corresponding to the ^{41}Ca concentration of 14 dpm/kg. Also, the concentration of ^{41}Ca was estimated to be 14 dpm/kg, which resulted from combination of the determined ^{36}Cl concentration and the

[1] Tokyo Metropolitan University

model calculation by Ammon et al. [3]. The ^{41}Ca concentrations in Dajala determined agree with the estimated concentration, mentioned earlier, indicating that the determined values of ^{41}Ca are believed to be accurate. On the contrary, for Gao meteorite, the two different concentrations of ^{36}Cl determined are 9.95 [2] and 5.93 dpm/kg are about 3 − 5 times larger than the estimated concentration. It is probable that the specimen of Gao meteorite for ^{41}Ca determination is different from those for the former ^{36}Cl determination. Determination of ^{36}Cl by using the Cl fraction of Gao meteorite will help to solve the discrepancy.

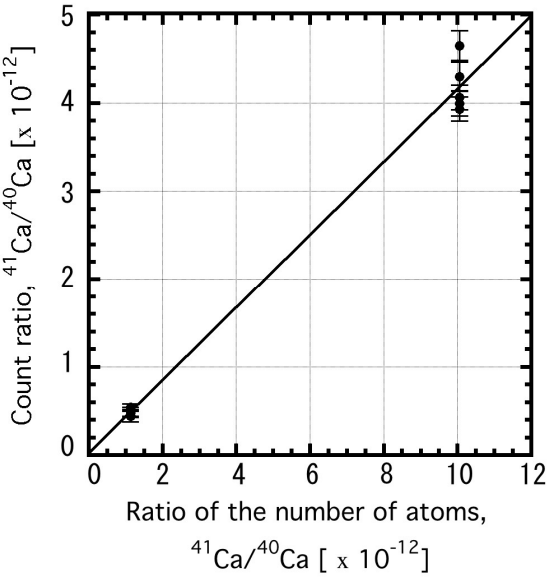

Fig. 1. Calibration curve for ^{41}Ca obtained by measurement of ^{41}Ca standard samples. Sensitivity of ^{41}Ca when using Ca^{5+} is almost the same as using Ca^{7+} at the run in 2016.

Table 1. Results for iron meteorites.

		Measurement time [s]	Count of ^{41}Ca	Atomic ^{41}Ca / ^{40}Ca [× 10^{-12}]	^{41}Ca [dpm/kg]	Estimated ^{41}Ca [dpm/kg]	Count of ^{41}K
Gao	A	3000	380	2.1	25 ± 1	5, 8	2010
	B	3000	295	2.0	24 ± 1		1662
Dajala	A	3000	67	0.73	14 ± 2	14	542
	B	5000	128	0.73	14 ± 1		1781

In reagent blank and procedure blank, 2.3 × 10^{-5} dpm and 3.0 × 10^{-5} dpm of ^{41}Ca were detected, respectively, using about 5 mg of Ca carrier. These are 30 − 100 times smaller than the detected ^{41}Ca in four meteorites samples. Assuming that a minimum limit of detection is two times that of ^{41}Ca in blank sample, down to 0.3 dpm / kg is found to be detectable if a sample of 0.1 g is used and Ca carrier of 4 mg is added.

References

[1] Y. Oura et al., UTTAC Annual Report 2016, UTTAC-86 (2017) 30.

[2] Y. Hamanaka et al., UTTAC Annual Report 2008, UTTAC-78 (2009) 27.

[3] K. Ammon et al., Meteoritics and Planetary Science 44 (2009) 485.

4.

BEAM AND ISOTOPE APPLICATIONS

4.1 Carrier trapping by vacancy-type defects in Mg-implanted GaN studied using monoenergetic positron beams

A. Uedono, S. Takashima[1], M. Edo[1], K. Ueno[1], H. Matsuyama[1], W. Egger[2], T. Koschine[2], C. Hugenschmidt[3], M. Dickmann[3], K. Kojima[4], S. F. Chichibu[4], S. Ishibashi[5]

Vacancy-type defects in Mg-implanted GaN are probed using monoenergetic positron beams. Mg^+ ions are implanted to provide a 500-nm-deep box profile with Mg concentrations, [Mg], of 1×10^{17}–1×10^{19} cm^{-3} at room temperature [1]. In the as-implanted samples, the major defect species is a complex of a Ga vacancy (V_{Ga}) and a nitrogen vacancy (V_N). After annealing above 1000°C, the major defect species is changed to vacancy clusters due to vacancy agglomeration. This agglomeration is suppressed, and the agglomeration onset temperature is decreased with a decreasing [Mg]. For samples with [Mg] ≥ 1×10^{18} cm^{-3}, the trapping rate of positrons by vacancy-type defects decreases after annealing above 1100–1200°C. This decrease is attributed to the change in the defect charge states from neutral to positive due to a downward shift of the Fermi level. The carrier trapping/detrapping properties of the vacancy-type defects and their time dependences are also revealed. Results are shown in Figs. 1-11.

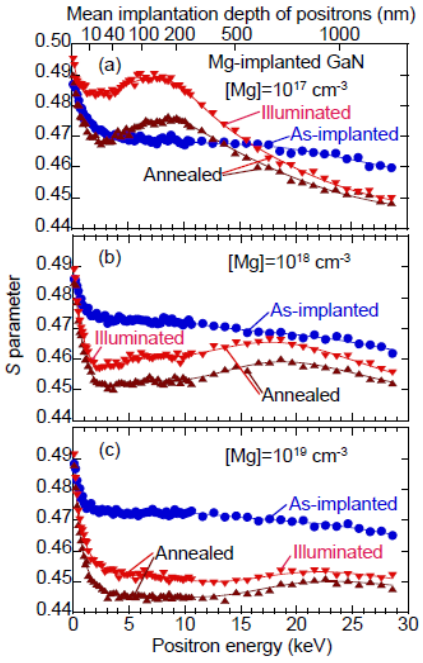

Fig. 1. S parameters as a function of the incident positron energy E.

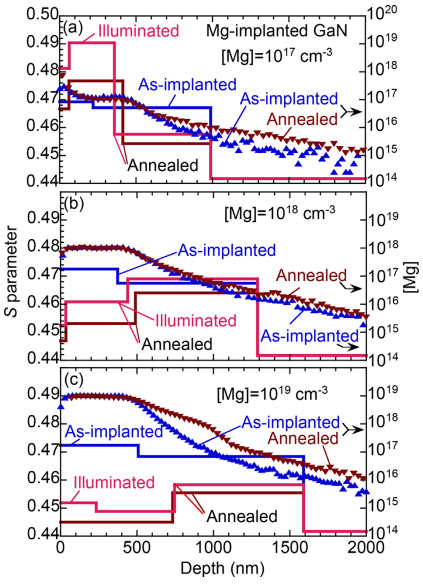

Fig. 2. Depth distribution of S obtained from the analysis.

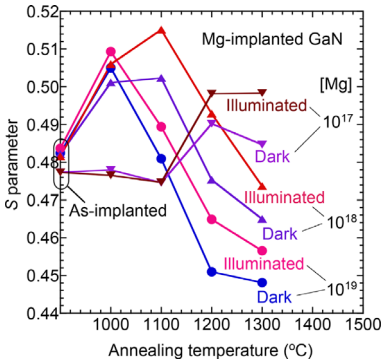

Fig. 3. Annealing behaviors of S for Mg-implanted GaN.

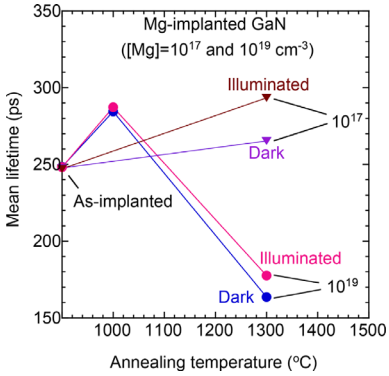

Fig. 4. Annealing behaviors of the mean lifetime for Mg-implanted GaN.

[1] Fuji Electric Co., Ltd.
[2] Universität der Bundeswehr München
[3] Technische Universität München
[4] Tohoku University
[5] National Institute of Advanced Industrial Science and Technology (AIST)

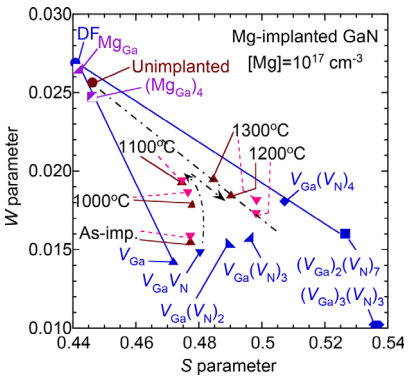

Fig. 5. S–W relationships for Mg-implanted GaN. with [Mg]=1×10^{17} cm^{-3}.

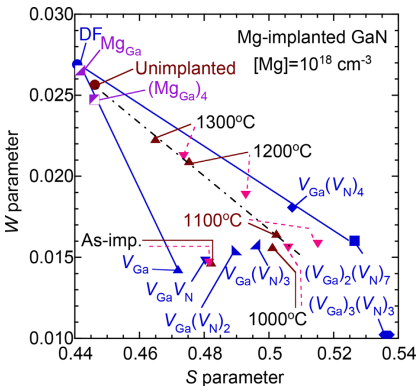

Fig. 6. S–W relationships for Mg-implanted GaN. with [Mg]=1×10^{18} cm^{-3}.

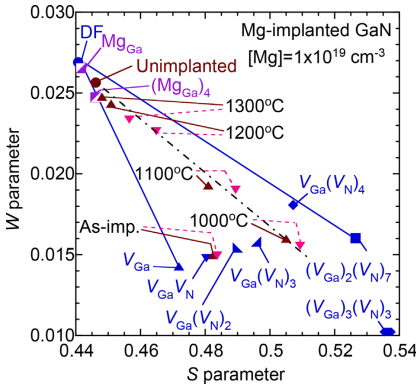

Fig. 7. S–W relationships for Mg-implanted GaN. with [Mg]=1×10^{19} cm^{-3}.

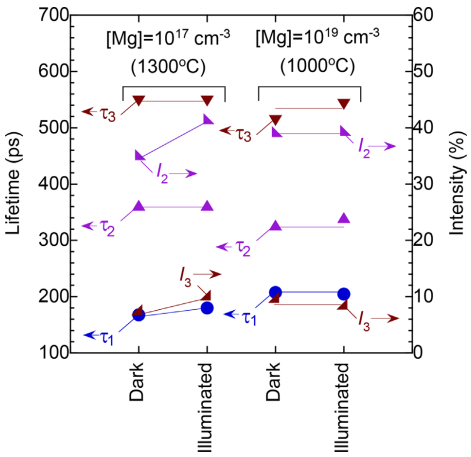

Fig. 8. Lifetimes (τ_1, τ_2, and τ_3) and the corresponding intensities (I_2 and I_3) for Mg-implanted GaN with [Mg]=1×10^{17} cm^{-3} after annealing at 1300°C and with [Mg]=1×10^{19} cm^{-3} after annealing at 1000°C.

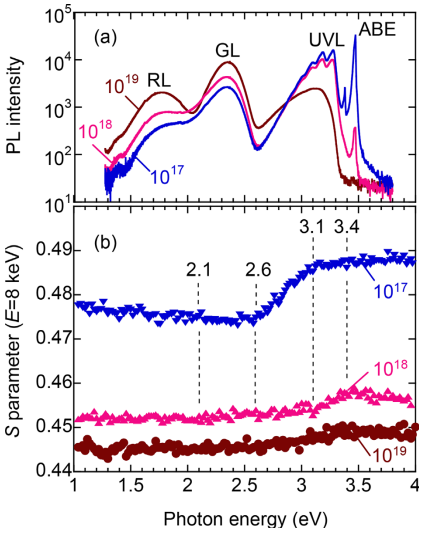

Fig. 9. a) PL spectra measured at 10K, and b) S values for Mg implanted GaN.

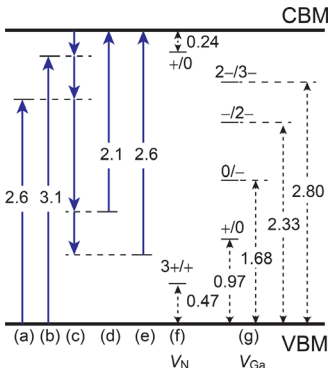

Fig. 10. Schematic band diagram and possible transition levels of the vacancy-type defects, where VBM and CBM are the valence band maximum and conduction band minimum, respectively.

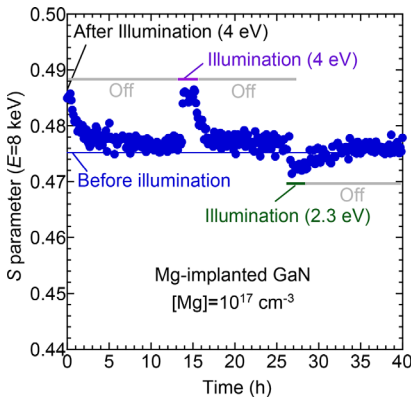

Fig. 11. Time dependence of S measured at E.=8 keV for Mg-implanted GaN with [Mg]=1×10^{17} cm^{-3}.

Reference

[1] A. Uedono et al., Phys. Status Solidi B 255 (2018) 1700521.

4.2 Two-dimensional mapping of hydrogen and other elements with microbeam-based transmission ERDA and PIXE

A. Yamazaki, H. Naramoto, K. Sasa, S. Ishii, S. Tomita, M. Sataka, H. Kudo, A. Uedono

Light trace elements in structural materials often affect their characteristics. PIXE measurements combined with microbeam scanning are frequently performed for mapping of trace elements in materials. Recently, development of thin window semiconductor detector has enabled detection of soft X-rays that are emitted from light elements such as boron, carbon and nitrogen, and microbeam PIXE becomes more and more useful for imaging light trace elements.

Hydrogen also plays an important role for some mechanical properties of materials. However, the PIXE analysis is not applicable to hydrogen detection since hydrogen atom emits no characteristic X-rays. Alternatively, we can use the ERDA method as an ion beam analysis of hydrogen. Especially, ERDA in the transmission geometry, i.e., transmission ERDA is suitable for the 2D mapping of hydrogen in thin samples. It is notable that in this energy range of He ions, the hydrogen recoil cross section is very large (a factor of up to $\sim$400 greater than that of the Rutherford cross section) , while the influence of bremsstrahlung is relatively low. In FY2017, we tried to obtain 2D maps of hydrogen and other elements simultaneously by parallel processing of signals from microbeam transmission ERDA and from microbeam PIXE.

Experimental setup of the simultaneous measurements for ERDA and PIXE is illustrated in Fig. 1. A ^{4}He beam of 8 MeV was provided by the 6MV tandem accelerator at UTTAC and its microbeam scanning was performed with the OM-2000 microbeam focusing and scanning system installed at L3 course of the tamdem accelerator facility [1]. The model sample prepared consists of three layers: a copper fine grid of 4–7 μm thickness (200 lines/inch, bar and hole widths of 12 and 113 μm, respectively), a 3.5-μm thick Mylar sheet, and a 80-μm thick aluminum film. The aluminum film was placed as a stopper of the incident ^{4}He beam, but was thin enough for transmission of recoil hydrogen atoms.

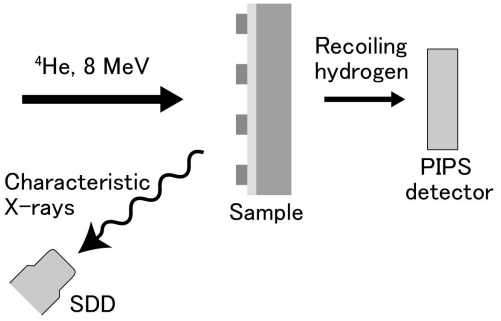

Fig. 1. Experimental setup of the simultaneous measurements for ERDA and PIXE.

The beam size on the sample was evaluated using the scanning transmission ion microscopy in off-axis geometry (off-axis STIM). A copper fine mesh was scanned by the ^{4}He ion microbeam. A Si-PIN photodiode was used to detect the forwardly scattered ^{4}He. The smallest beam diameter estimated from the sharpness of the edge profiles of the STIM images is 2 μm. This value provides the spatial resolution

of elemental distributions in samples.

Figures 2(a) and 2(b) show the measured transmission ERDA and PIXE spectra, respectively. The recoil hydrogens from the Mylar sheet are recognized in the ERDA spectrum, reflecting the energy dependence of recoil cross section under the present experimental conditions. In the PIXE spectrum, the two peaks around 1500 channel indicate copper K_α (8.05 keV) and K_β (8.91 keV) X-rays.

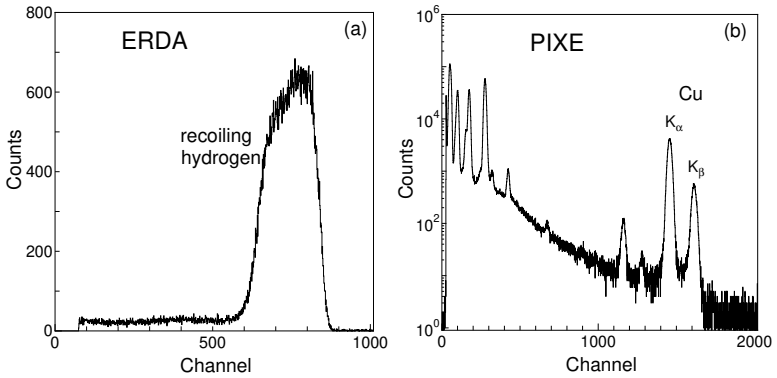

Fig. 2. (a) ERDA and (b) PIXE spectra obtained by irradiating the sample with an 8 MeV ^{4}He beam.

Figure 3 shows measured elemental maps of hydrogen and copper in the sample. The hydrogen images obtained by transmission ERDA is shown as orange-colored squares in Fig. 3(a). In contrast, Fig. 3(b) shows the simultaneously measured image of the copper fine mesh (yellow-colored) on the surface of the sample. These two maps are surely the reverse images of each other because the ^{4}He projectile that passes through the copper grid no longer has sufficient energy to contribute to the hydrogen mapping. A pair of these maps provides complementary information on multi-elemental distributions in the sample. The present results indicate that the combined PIXE-ERDA method might become a powerful tool beyond the existing analytical methods.

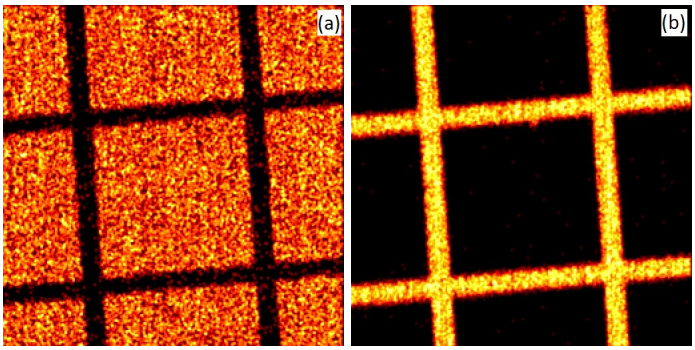

Fig. 3. 2D elemental mapping of (a) hydrogen by ERDA, and (b) Cu K X-rays by PIXE.

References

[1] A. Yamazaki et al., Nucl. Instr. Meth. Phys. Res. B 404 (2017) 92.

[2] A. Yamazaki et al., Submitted to Nucl. Instr. Meth. Phys. Res. B.

4.3 Production of 16 channel preamplifier module and development of high-sensitivity HERDA equipped with strip SSD

D. Sekiba, K. Tsujita, Y. Sugisawa, I. Harayama, M. Uenomachi[1], K. Shimazoe[1], H. Takahashi[2], K. Ozeki[3]

HERDA (High-resolution Elastic Recoil Detection Analysis) is a useful method to determine the hydrogen depth profile with mono-layer depth resolution [1, 2]. In the last decade, we have made efforts to improve the detection limit for hydrogen by, for example, introducing the double MCP system [3] and/or the moving SSD (solid state detector) system. While the use of the moving SSD as a position sensitive detector can suppress the two main noise sources, i.e., dark currents and stray particles, it is really time consuming. In order to solve this difficulty, we adopted a 16 channel strip PIPS (Passivated Implanted Planar Si detector, CAMBERRA, type: PF-16RT-58*58-300EB) of 58×58 mm^2, so that the pitch of the 16 pad is ~ 3.6 mm.

For operation of the 16 channel strip PIPS, we made a 16 channel preamplifier module, in which the down-sized preamplifier tips (see Fig. 1(a)) reported previously [4, 5] were installed. The home-made 16 amplifier tips were put in the two NIM module cases. Figure 1(b) and 1(c) show the inside and the front panels of the NIM modules, respectively.

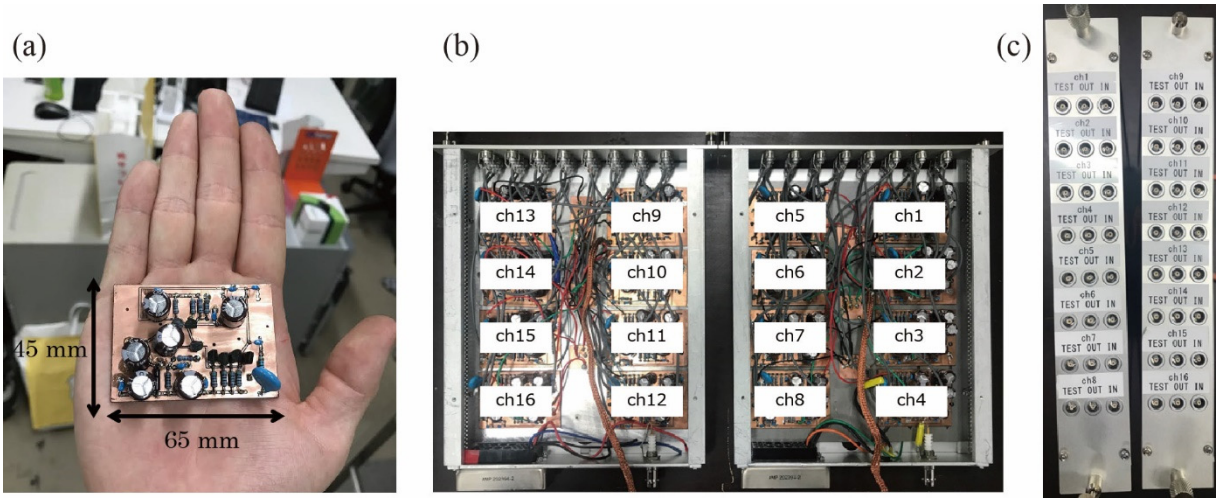

Fig. 1. (a) Down-sized preamplifier on a hand of Mr. Tsujita (the maker of the preamplifiers). (b) Inside of the NIM modules, in which the 16 preamplifiers are settled. (c) Front panels of the developed NIM modules. A set of three connectors for input, output, and test pulse are allotted to each channel.

The 16 signal lines are extracted to the outside of the chamber via an electric feedthrough with the shape of the D-sub connector. The signal lines were connected to the NIM modules of preamplifier beside the chamber. The outputs were connected to a home-made dToT (dynamic Time over Threshold) [6] module put in a NIM case, in which CR-RC circuits and dToT circuits are installed.

[1] Department of Nuclear Engineering Management, School of Engineering, The University of Tokyo
[2] Institute of Engineering Innovation, School of Engineering, The University of Tokyo
[3] Department of Mechanical Engineering, Ibaraki University

The test of the new system, in which the new detector and electronics were involved, was performed in the D-course of 1MV Tandetron in UTTAC. The sample was a-C:H (hydrogenated amorphous carbon) film (t ~ 170 nm) deposited on a Si wafer. The hydrogen concentration in the film was 2.1×10^{22} atoms/cm^3 determined by RBS (Rutherford backscattering)/ERDA. 1 MeV $^{16}O^+$ was used as an incident beam. The recoil angle was 30º with respect to the beam incident direction.

Figure 2(a) shows the measured histogram as a function of time over threshold at each channel. We can see a series of peaks in the region surrounded by the two red dotted lines. These peaks correspond to the hydrogen recoils, and their yields are reconstructed as the HERDA spectra in Fig. 2(b) with the blue circles. The spectrum qualitatively reproduced that taken by a conventional MCA (multi-channel analyzer) system (red circles), though ~15% of the signals seems to be lost with the developed dToT systems. Most of the lost part could be included in the long tails seen in the short time side of Fig. 2(a). We will try to fix this problem in the future. The detection limit of hydrogen derived from the HERDA spectrum with dToT is 8.0×10^{19} atoms/cm^3 for 149 sec of data acquisition time.

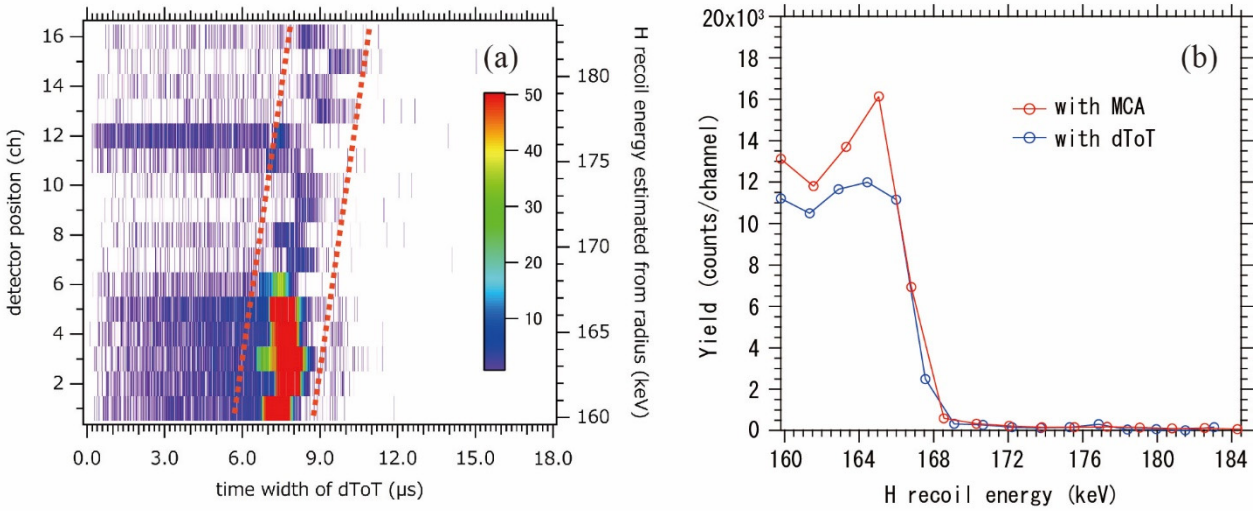

Fig. 2. (a) Two-dimensional histogram of yield as a function of time and channel of the detector. The two red dotted lines are ROI (Region of interest) of the yield integration. (b) HERDA spectra taken with the combination of the strip PIPS and a commercially available preamplifier, normal shaper and MCA system (red) and taken with the developed dToT system (blue).

References

[1] K. Kimura et al., Nucl. Instr. Meth. Phys. Res. B 140 (1998) 387.

[2] D. Sekiba et al., Nucl. Instr. Meth. Phys. Res. B 401 (2017) 29.

[3] D. Sekiba et al., Nucl. Instr. Meth. Phys. Res. B 430 (2018) 6.

[4] Y. Hosono et al., Nucul. Instr. Meth. A 361 (1995) 554.

[5] K. Tsujita et al., UTTAC annual report 2016 (2017) 36.

[6] Y. Tiang et al., IEEE Trans. Nucl. Sci. 62 (2015) 1798.

4.4 Location of hydrogen in Mg/H-coimplanted GaN by RBS/ERDA and channeling NRA

J. Kikuda, I. Hrayama, T. Ozawa[1], K. Fukutani[1], D. Sekiba

Gallium nitride (GaN) is a wide-band-gap semiconductor, which is promising for the optoelectronic and high-power devices. In spite of much effort on the device construction, the formation of p-type GaN with the Mg implantation has still problems to be overcome. Some experimental results implied that hydrogen beside Mg passivates most of the acceptors (Mg in this case) [1]. It is believed that the subsequent treatments after the Mg implantation, such as the high temperature flashing at ~1000 ºC or the electron bombardment, induce the desorption of hydrogen. The removal of hydrogen would lead to the settling of Mg on the correct Ga site. This scenario has, however, not been experimentally established yet. In order to examine this scenario, we employed RBS/ERDA (Rutherford backscattering spectrometry / Elastic recoil detection analysis) and channeling NRA (Nuclear reaction analysis). In the present report, the insights obtained on the hydrogen desorption temperature and the location in the lattice are reported.

RBS/ERDA was carried out in the D-course of 1MV Tandetron at UTTAC. A beam of 2.5 MeV $^{4}He^{2+}$ was shaped to 1 × 1 mm^2 by the single slit system. The recoil and backscattering angles are 30º and 150º with respect to the beam direction, respectively [2]. The beam incident angle on the sample was 75º from the surface normal. The channeling NRA experiment with ^{1}H (^{15}N, αγ) ^{12}C was carried out at Micro Analysis Laboratory, Tandem accelerator (MALT) in the University of Tokyo. A beam of ~6.4 MeV $^{15}N^{+}$ was shaped to 2 × 2 mm^2 by the double slit system and the beam energy was tuned to explore the depth of 50 nm. The characteristic 4.43 MeV γ-rays were collected by the two 4-inch BGO scintillators.

The three-step dopant implantation was carried out as follows, 30 keV $^{24}Mg^{+}$ with 3.5 × 10^{13} at/cm^2 , 60 keV $^{24}Mg^{+}$ with 6.5 × 10^{13} at/cm^2, and 7 keV H_2^{+} with 7.0 × 10^{14} at/cm^2. Five different samples were prepared with varying the subsequent annealing temperature: #1 at 900 °C, #2 at 950 °C, #3 at 1000 °C, #4 at 1050 °C, and #5 at 1100 °C.

Figure1 shows the ERDA spectra taken for the samples #2~5. The surface peaks observed at 1200 keV, are due to the adsorbates containing hydrogen. On the sample #2 (red), we can observe a broad peak over the energy region of 700 ~ 1000 keV. This energy corresponds to the depth of the implanted hydrogens. This broad peak disappears for the sample #3, and no longer appears for the samples with the higher-temperature annealing (#4, #5). It is found for the first time that the co-implanted hydrogen desorbs at a temperature between 950 °C and 1000 °C. It is of further

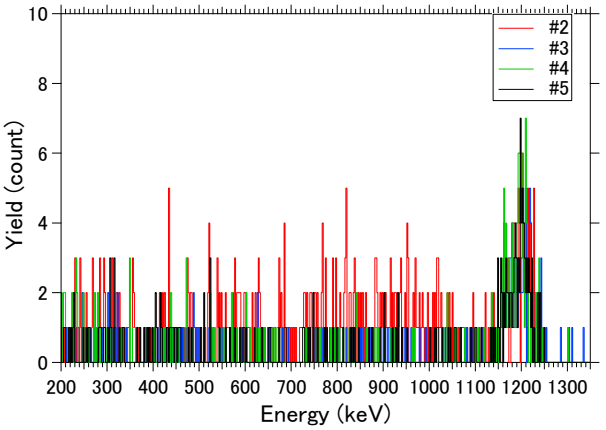

Fig. 1. ERDA spectra taken on GaN of #2~5.

[1] Institute of Industrial Science, University of Tokyo

interest to perform similar measurements for the samples annealed with a finer step of temperature.

Figure 2 shows the two dimensional (2D) mapping of RBS yields taken with sweeping the angles with respect to the vertical axis θ (polar) and horizontal axis φ (tilt). In this measurement, a 6.4 MeV $^{15}N^{2+}$ beam was incident on sample #1. The angles (θ, φ) = (3.6, 0.0) correspond to the [0001] axis of GaN.

We performed NRA measurements at three points in the 2D map A (θ, φ) = (5.4, 1.7), B (θ, φ) = (3.6, 0), and C (θ, φ) = (0.6, −2.6) as indicated in Fig. 2. These points correspond to random, axial channeling, and planar channeling conditions, though the point C is slightly displaced from the correct position not intentionally. Figure 3 shows the NRA spectra taken with the beam incidence angle corresponding to the points A ~ C in Fig. 2. We can see broad peaks at ~4.4 MeV slightly distinguishable from the background in each spectrum, which can be attributed to 4.43 MeV γ-ray of ^{1}H (^{15}N, αγ) ^{12}C.

Figure 4 displays the integrated yields of the 4.43 MeV γ-ray signals taken at the points A ~ C. While the statistical errors are still large, it seems that the yields for the axial and planar channeling are larger than that for the random case. This implies that the considerable amount of hydrogen stays at the interstitial site involved in the axial and other planar channels. In future, a comparative study with similar measurements taken for the annealed samples should provide detailed information on the behavior of hydrogen.

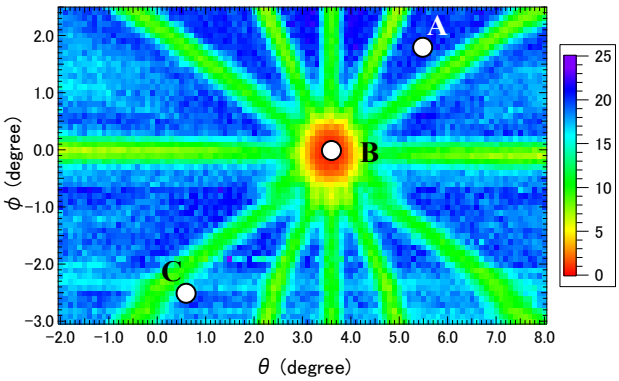

Fig. 2. 2D map of RBS yield taken with sweeping θ and ϕ.

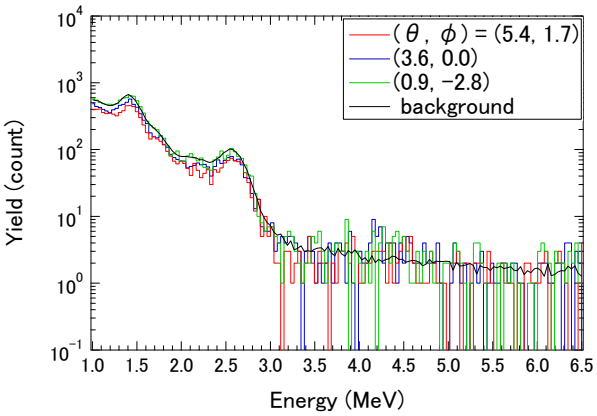

Fig. 3. NRA spectra taken at the three points A ~ C indicated in Fig. 2.

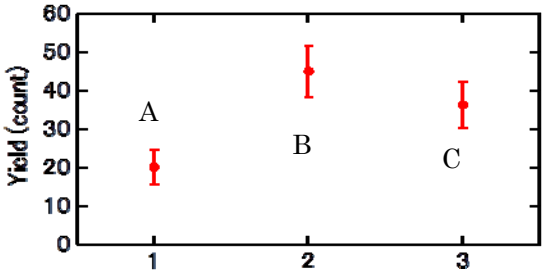

Fig. 4. The amount of hydrogen determined from the results shown in Fig. 3.

References

[1] S. Nakamura et al., Jpn. J. Appl. Phys. 31 (1992) 1258.

[2] D. Sekiba et al., J. Appl. Phys. 106 (2009) 114912.

4.5 Present status of TOF-E telescope ERDA system development

Y. Sugisawa, D. Sekiba, I. Harayama

Recently, there are high demands for analysis of light elements in thin films. For instance, since the continuous control of anion composition in metal oxides enables us to tailor their optical, electronic and structural properties, it is necessary to determine the compositional ratio of the anions, in particular of O and N [1]. TOF (Time of Flight) -E (Energy) telescope ERDA (Elastic Recoil Detection Analysis) is an effective method of depth profiling of light elements with the elemental identification [2]. It usually has a better depth resolution than that of ΔE-E telescope ERDA [3]. This property is expected to be applicable to the analysis of thin multilayer films. We have developed TOF-E telescope ERDA system mainly with the aim of the determination of O/N ratio and also with a sufficient depth resolution suitable for analysis of multilayer films, in which each layer has a thickness of several tens of nanometers.

In this system, the velocity and energy of a recoiling particle are measured coincidently, which allows identification of the particle mass. Figure 1 shows a schematic view of the TOF-E telescope ERDA system installed at D-course of 1 MV Tandetron at UTTAC. We employed two time-detectors, T1 and T2, and one SSD (solid state detector) of 300 mm^2. T1 and T2 generate the start and stop triggers in the TOF measurement, respectively, while SSD determines the kinematic energy of the particle. The time-detectors consist of MCPs (Micro Channel Plate), carbon foils with a thickness of 7 $\mu g/cm^2$ and electrostatic-mirror-grids, as shown schematically in Fig. 2 [4]. When the recoiling particle passes through the carbon foil, secondary electrons are emitted from the carbon foil and are reflected by the mirror grid. They are then detected by MCP. The carbon foils T1 and T2 are set on the ϕ9 and ϕ15 mm apertures, respectively. T1 is placed at 263 mm apart from the sample and the distance between the two time-detectors is 428 mm. SSD is placed at 771 mm apart from the sample. In this layout, the solid angle of acceptance of the present system is 0.37 msr, taking into account the effective area of SSD.

In the present study, the incident beam was 4 MeV $^{35}Cl^{4+}$ and the typical beam size was shaped to about 1×1 mm^2 with a double slit system. The beam was incident at 75º from the surface normal of the sample and the recoiling particles were measured at −75º from the surface normal. Accordingly, the recoil angle was 30º from the beam direction. The typical beam current was several nA. The data acquisition time was ~ 1 hour for one sample.

Figure 3 shows a two-dimensional histogram of the developed TOF-E telescope ERDA measured for a Kapton film which is composed of H, C, N and O. The assignment of these elements is given in Fig. 3. Note that the Cl ridge in the histogram results from the Cl ions that are scattered at 30º in the Kapton film. The estimated time resolution of the present system is 1.5 ns and the corresponding mass resolution is 1.0 u (u: unified atomic mass unit) around the mass of O. Since the difference of mass for N and O is about 2 u, these two elements are distinguishable with this setup. Figure 4 shows the line profile at 2.6 MeV, obtained for a 48 keV energy width which is indicated with two vertical lines in Fig. 3. Certainly, we can recognize C, N, and O peaks in Fig. 4.

In the present, there are two main problems in our TOF-E telescope ERDA system. One is the

difficulty in separating individual distributions of C, N, and O from the histogram, although peaks of each element are recognizable. To do this, it necessary to improve the time resolution which is determined dominantly by the signal processing system. The other is the total detection efficiency of the time -detectors, which is lower than that of SSD. The total detection efficiency of the current system estimated for 5×10^4 s was less than 2.6% so that most of the secondary electrons emitted from the carbon foil were lost before arriving at MCP. In future works, we are going to optimize the signal processing system and develop new time detectors to improve the time resolution and the detection efficiency.

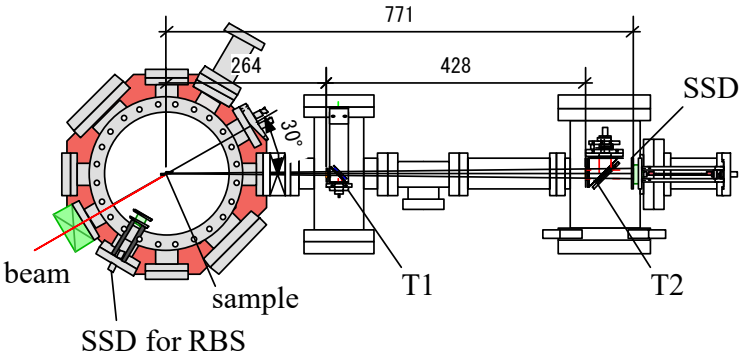

Fig. 1. Schematic view of the developed TOF-E telescope ERDA system.

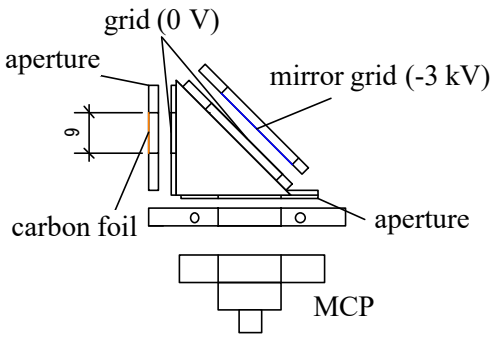

Fig. 2. Arrangement of MCP, a carbon foil, and an electrostatic mirror grid in the time detector used in the present system.

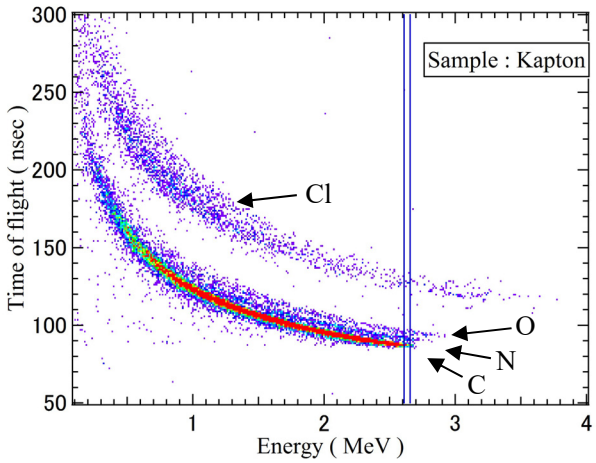

Fig. 3. Two-dimensional histogram for a Kapton film measured using the developed TOF-E telescope ERDA system. Note that Cl ridge is due to scattered Cl ions.

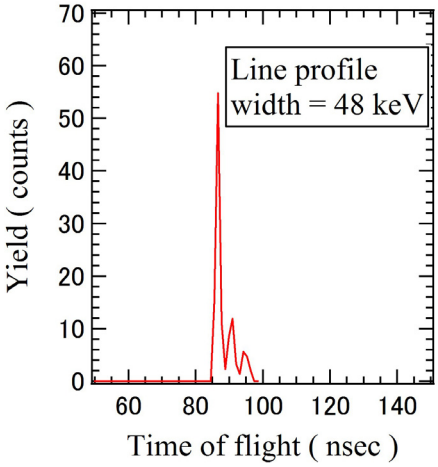

Fig. 4. Line profile of the two-dimensional histogram shown in Fig. 3 around 2.6 MeV with the width of 48 keV.

References

[1] A. Kobayashi et al., Phys. Status Solidi RRL 8 (2014) 362.

[2] J. Julin et al., Nucl. Instr. Meth. Phys. Res. B 406 (2017) 61.

[3] I. Harayama et al., Nucl. Instr. Meth. Phys. Res. B 384 (2016) 61.

[4] F. Busch et al., Nucl. Instr. Meth. 171 (1980) 71.

4.6 Experimental verification of a gain reduction model for the space charge effect in a wire chamber

K. Fujii[1], I. Harayama, Y. Kato[1], N. Nagakura[1], D. Sekiba, Y. Watahiki, S. Yamashita[2]

In our neutron lifetime precise measurement in J-PARC, we monitor and collect the tracks of proton and β-ray coincidently in a wire chamber. Under the condition that the parameters of the wire chamber are optimized to the β-ray detection, the output linearity for protons is crucially suffered from gain reduction due to the space charge effect. In order to collect the desirable events correctly, it is necessary to obtain the gain reduction factor s based on a phenomenological model.

A gain reduction model was previously proposed taking into account the self-induced space charge effect [1], whereas the experimental verification of the model has been still required. In the model, s is expressed as follows,

$$s \equiv \frac{\log\left(1 + f G_0 \frac{dE}{dl}\right)}{f G_0 \frac{dE}{dl}} , \qquad (1)$$

where f is a constant factor including all microscopic characteristics of the space charge effect, which determines the absolute scale of gain reduction, G_0 is the multiplication factor without the space charge effect, dE/dl is energy loss per wire length. Actually, dE/dl depends on the geometry of the wire and the projectile directions. G_0 is determined by energy calibration using ^{55}Fe X-rays. The factor f is treated here as a fitting parameter since it is hard to calculate it analytically.

In this study, a multi-wire drift chamber (MWDC) filled with a mixed gas of He and CO_2 was irradiated by a proton beam from the Tandetron accelerator at UTTAC. The proton beam energy E_p, the applied anode wire voltage V_0, and the angle of the proton beam direction relative to the anode wires of the MWDC, ϕ, were changed as experimental parameters. The dependence of s on these parameters is compared with that expected by the model.

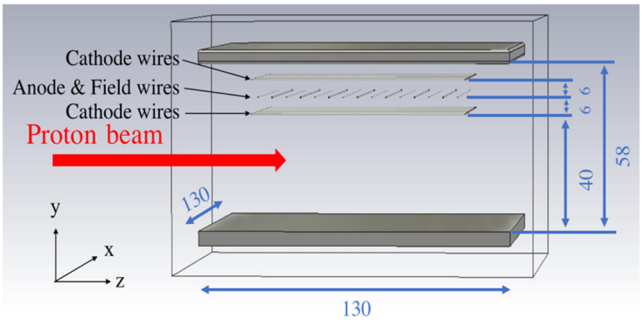

Fig. 1. The schematic layout of the MWDC.

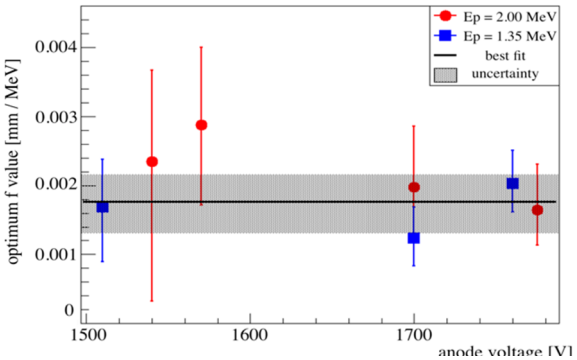

Fig. 2. Combined results of the optimum f values.

[1] Graduate School of Science, University of Tokyo
[2] International Center for Elementary Particle Physics, University of Tokyo

Figure 1 shows the overall structure of the MWDC, which has a dimension of 13 cm × 13 cm × 6 cm. It is made of G10 FR-4, or glass-epoxy laminate, and is housed in a 14 L vacuum chamber filled with 85 kPa He gas and 15 kPa CO_2 gas. Electrons created by ionization of the gas are drifted by an electric field of 4×10^2 V/cm in the *y*-direction, towards the multi-wire region located in the upper part of the MWDC.

The output pulse heights for the proton beam were initially measured at a multiplication factor of about 10^3 by tuning the anode voltage. The results were compared with those obtained from the Geant4-based Monte Carlo simulation [2] assuming the same MWDC geometry. It is successfully confirmed that the experimental distributions for the different beam energies can be reproduced by the simulations under the conditions of the "low enough" multiplication factors quantitatively.

The output pulse heights for the proton beam obtained with a high multiplication factor (~10^4) were then compared with the energy deposition calculated by the simulations. The data were taken with changing ϕ from 40 to 90° at an interval of 10° to find the dependence on dE/dl. In this way, s was derived as the ratio of the experimental output pulse height with respect to the simulation results without gain reduction effect. The value was compared with the results of simulations with the gain reduction model with sweeping f as a free parameter. The f value that minimizes χ^2/ndf was selected as the optimum value.

Figure 2 shows the result of the derived f values for different values of E_p and V_0. The f values seems to be a constant within the present uncertainties. The comparison of the experimental energy deposit distributions before and after correcting for the space charge effect is shown in Fig. 3, together with those calculated by the simulation. The energy deposit distributions corrected by the space charge effect based on the proposed model agree well with the simulation results. Thus the space charge effect can be included certainly, once an appropriate f value is found and is well scaled with the relative difference of the angles between the wire and projectile directions. For details, see Ref. [3].

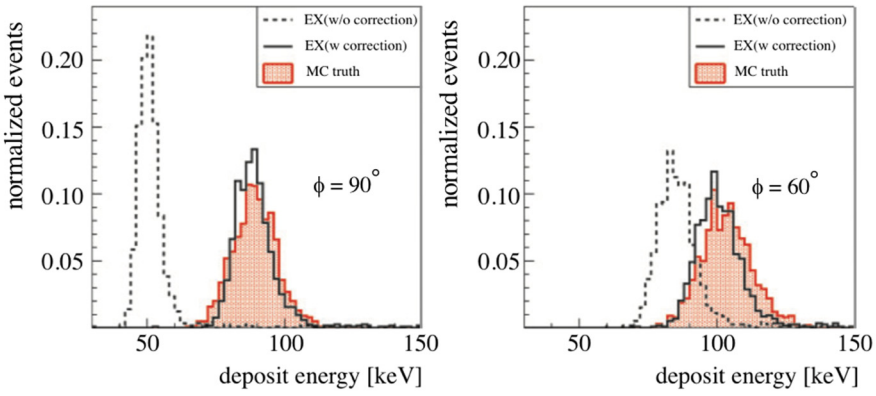

Fig. 3. The experimental energy deposit distributions with and without the correction of the gain reduction for ϕ=90º (left) and 60º (right), together with the simulation results.

References

[1] Y.Arimoto et al., Nucl. Instr. Meth. Phys. Res. A 799 (2015) 187.

[2] S. Agostinelli et al., Nucl. Instr. Meth. Phys. Res. A 506 (2003) 250.

[3] N. Nagakura et al., Prog. Theor. Exp. Phys. 013C01 (2018).

4.7 Quantitative micro-PIXE analyses of trace elements in sphalerite from hydrothermally-altered sediments

M. Kurosawa, K. Ikehata, K. Hattori, K. Sasa, S. Ishii

Sphalerite, a cubic form of ZnS (β-ZnS), is the most common zinc ore mineral and is widespread in hydrothermally altered rocks [1]. A chemical property of sphalerite is a deviation from stoichiometry in ZnS. Also, small cation vacancies (less than 1 atom %) have been observed [1]. In addition, natural sphalerites contain Fe, Mn, Cd, Co, Se, and Hg at a concentration levels of several tens to thousands parts per million weight (wt. ppm) [1–5]. Another trace impurities of Ti, Cu, Sb, Sn, In, Ag, As, Ga, Ge, Ni, Ba, Mo, V, and Cr have been also reported in natural samples [1–5], so that sphalerite is the major source material of Cd, In, Ge, and Ga [1]. Since concentration levels of the minor and trace heavy-elements are considered to be very close to hydrothermal conditions, these contents have been frequently analyzed to examine formation processes of hydrothermally-altered rocks and hydrothermal ore deposits [1–5]. For these reasons, we analyzed major to trace elements in sphalerites from deep sea-floor sediments altered by hydrothermal activities to examine a heavy-metal condensation by the same activities.

Determination of trace elements can be usually performed by using particle-induced X-ray emission (PIXE), reported here, and laser-ablation inductively-coupled plasma mass spectrometry (LA–ICP–MS) [2–5]. The sphalerite samples for PIXE were collected from drilling core samples of thick sea-floor clay sediments near an active hydrothermal field at Iheya-North-Knoll in the Okinawa Trough back-arc basin, Japan [6]. The sediments consisted mainly of clay minerals including Mg, Na, K, and Ca and contained small amounts of secondary minerals formed by the hydrothermal activities [6]. The present samples were a few millimeter-sized and polygonal-shaped crystals with no visible inclusions of their secondary minerals. The sample surfaces were polished and were coated with a carbon film to prevent electrostatic charging.

PIXE analyses were performed at the 1MV Tandetron accelerator. A 0.1 to 0.3 nA beam of 1.92-MeV proton was focused to a 26 × 26 μm^2 to 33 × 36 μm^2 spot on the sample using slits and magnetic lenses. The beam was incident perpendicularly on the sample surface, and the X-ray measurement take-off angle was 45° [7]. The characteristic X-rays excited by the incident beam were collected by the Si(Li) X-ray-energy detector with a nominal resolution of 137 eV at 5.9 keV. Since measurements of intense X-rays from S and Zn were required to examine the stoichiometry in ZnS, we used a 55-μm-thick Mylar filter to prevent the entry into the detector of protons scattered from samples. The total charge was determined by integrating the target currents, and all samples were analyzed to the integrated charges of 0.05 to 0.25 μC. Analytical points were chosen based on optical viewing using a CCD camera mounted on the microscope. Quantification of the PIXE analyses was performed based on the model of Kurosawa et al. [7]. Secondary fluorescence effect was corrected by the method of Reuter et al. [8].

PIXE spectra of the sphalerite samples consist mainly of intense K X-ray peaks from S and Zn, and their pile-up and escape peaks as shown in Fig. 1. The spectra show K X-ray peaks from Mn, Fe, Co, Ni, and Cu, and L X-ray peaks from Cd and Pb. These elements are major impurities in the present sphalerite

samples. There is no significant peak overlap between the escape and pile-up peaks and L X-ray peaks from important impurities (Cd and Pb) in sphalerite. L X-ray peaks from another important impurities (Ag, In, Sn, Sb, Ga, Ge, As, and Se), although they are absent in the present case, would not be affected by the escape and pile-up peaks.

Element concentrations of the sphalerite (Fig. 1), determined by PIXE, were as follows: 60.45 wt.% for Zn, 32.83 wt.% for S, 2.760 wt.% for Fe, 1.848 wt.% for Cu, 0.550 wt.% for Mn, 0.495 wt.% for Pb, 0.139 wt.% for Cd, 440 ppm for Co, 420 ppm for Ni, and 210 ppm for Cr. These contents of element, except for Pb, were almost the same as those of another sphalerite samples from the present altered sediments. These minor and trace-element contents almost agreed with those from sphalerites in sea-floor hydrothermal ore deposits. [2, 5]. Detection of the present high Pb contents may be due to microscopic or invisible inclusions of galena (PbS) [4].

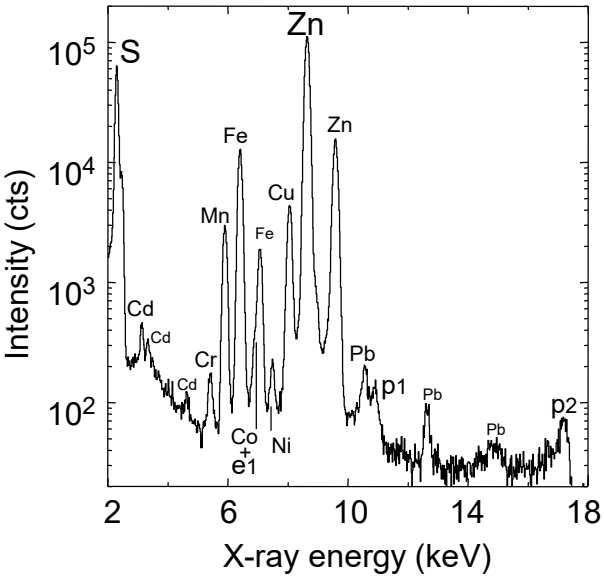

Fig. 1. PIXE spectrum of sphalerite in altered sea-floor sediments. Escape and pile-up peaks are identified as follows: e1 (escape peak of Zn Kα), p1 (pile-up peak of S Kα+Zn Kα), and p2 (pile-up peak of Zn Kα+Zn Kα).

A chemical formula of the sphalerite (Fig. 1) is $(Zn_{0.903}Fe_{0.048}Cu_{0.028}\ Mn_{0.010}Pb_{0.002}Cd_{0.001}\ Co_{0.001}Ni_{0.001})_{0.994}S_{1.000}$, indicating the stoichiometry of ZnS composition. Most of the sphalerite samples demonstrated similar stoichiometry with slight cation deficiencies, indicating that the hydrothermal activities (<500 °C) do not affect the stoichiometry of sphalerite.

In summary, the present PIXE analyses demonstrated that chemical compositions of sphalerites from the present altered sediments were very similar, except for Pb. No large cation deficiency (non-stoichiometry) associated with the hydrothermal activities were also observed in the sphalerite. These data imply that sphalerites from the surveyed area lack a chemical feature indicative of hydrothermal activity related to ore deposit formation. In the future work, it may be important to explore possibility of the sphalerites as a source material for the elements (Cd, In, Ge, and Ga) of industrial importance.

References

[1] J. F. W. Bowles et al., Rock Forming Minerals. Vol. 5A, Non-Silicates: Oxides, Hydroxides and Sulphides, The Geological Society of London, London (2011) p418.

[2] D. Huston et al., Econ. Geol. 90 (1995) 1167.

[3] S. Murao et al, Nucl. Instr. Meth. Phys. Res. B 109/110 (2008) 627.

[4] N. Cook et al., Geochim. Cosmochim. Acta 73 (2009) 4761.

[5] J. Lockington et al, Miner. Petrol. 108 (2014) 873.

[6] Y. Miyoshi et al., Resour. Geol. 65 (2015) 346.

[7] M. Kurosawa et al., Nucl. Instr. Meth. Phys. Res. B 266 (2008) 3633.

[8] W. Reuter et al., J. Appl. Phys. 46 (1975) 3194.

4.8 Preliminary report on micro-PIXE analysis of trace Ni in single fluid inclusions from a miarolitic quartz at Tsushima granite

M. Kurosawa, K. Sasa, S. Ishii

Nickel is an abundant element in the Earth's mantle and core, and the abundance in the primitive mantle (2000 ppm) is twenty times higher than that in the bulk continental crust [1]. Thus, mafic magmas derived from the mantle normally contain high concentration of Ni. Whereas, Ni abundances in granitic rocks are relatively low (9–17 ppm; [1]), and accordingly, nickel minerals are rare in granitic rocks and hydrothermal veins related to granites. There is also no detection of trace Ni in fluid inclusions from granitic rocks and the hydrothermal veins. Some nickel sulfide minerals, however, have been sometimes observed from hydrothermal ore veins in or near granites [2–6], and the origin of Ni remains as an issue to be solved [5]. In most cases, the origin might be ascribed to contaminations of Ni leached from the surrounding mafic rocks [5] or sedimentary rocks [6], but a possibility of purely granitic-magma origin still remains [2, 4]. In this report, we describe the first observation of trace Ni in fluid inclusions from a miarolitic quartz at Tsushima granite with the purely magmatic origin [7].

A quartz crystal including fluid inclusions was collected from a miarolitic cavity in biotite granite at Uchiyama, the Tsushima islands, Nagasaki Prefecture, Japan [8]. The quartz crystal contains many polyphase and vapor-rich fluid inclusions formed by brine-vapor separation due to fluid boiling (Fig. 1). Subordinate two-phase aqueous inclusions, trace amount of liquid CO_2 and aqueous liquid-rich inclusions were also observed in the quartz crystal [8]. A considerable amount of Ni were detected in some vapor-rich and polyphase fluid inclusions from the miarolitic quartz. Salinities of the vapor-rich inclusions were mainly of 0.5–2.2 wt.% NaCl equivalent. The vapor-rich and polyphase inclusions were typically 30–60 μm in size, ellipsoidal or negative-crystal shapes, and the inclusion depths were less than 10 μm. The quartz-crystal samples were cut and polished, and then the surface was coated with a carbon film to prevent electrostatic charging.

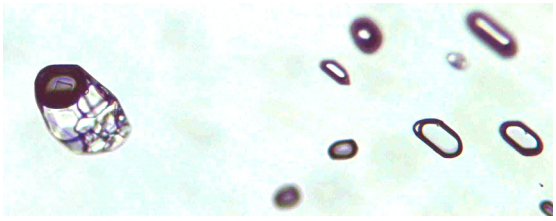

Fig. 1. Photomicrograph of polyphase and vapor-rich fluid inclusions in a quartz crystal from miarolitic cavity at Tsushima granite. A large inclusion on the left side is a polyphase inclusion, 70 μm in size, with a bubble (dark ellipsoidal) and many daughter crystals of halite, $FeCl_2$ and so on. Several ellipsoids in the right side are vapor-rich inclusions.

The procedure for PIXE analysis is noted briefly here since the details are described in §4.7 of this Annual Report. A 1.0 to 2.0 nA beam of 1.92-MeV proton was focused to ~50 ×50 μm^2 spot on the sample. A filter of 55-μm-thick Mylar film was used for the X-ray detector not only to prevent the stray protons, but also to attenuate the intense X-rays from the predominant light elements. All samples were analyzed for irradiation of 1.92-MeV H^+ with integrated charge of 2.0 μC. In the present analysis, the correction of the secondary fluorescence effect amounts to only less than a few % for most of the elements.

The PIXE spectrum of a vapor-rich fluid inclusion from the miarolitic cavity consists of K X-ray peaks from Al, Si, S, Cl, K, Ca, Ti, Mn, Fe, Ni, Cu, Zn, and Br, and of L X-ray peaks from Pb (Fig. 2). Most of

vapor-rich inclusions from the miarolitic cavity demonstrates similar X-ray spectra. Element concentrations of the vapor-rich inclusion determined by the PIXE data are as follows: 3325 ppm for Cl, 2301 ppm for K, 1884 ppm for Fe, 1720 ppm for Ca, 111 ppm for Mn, 82 ppm for Zn, 60 ppm for Pb, 38 ppm for Ni, 24 ppm for Cu, and 3 ppm for Br. Most of the vapor-rich inclusions contain about 5–30 ppm Ni. The polyphase inclusions also contain Ni of 5 to 50 ppm. These are the first observation of trace Ni in fluid inclusions from granite-related rocks.

Miarolitic cavities in granite are void spaces with outlines shaped by large quartz and feldspar crystals and are commonly formed by entrapment of fluid separated from granitic magma during solidification of the granite [8]. Thus, the detection of trace Ni in the fluid inclusions indicates the presence of Ni in hydrothermal fluids originally released from the granite. In northern Tsushima, Ni-containing sulfide minerals have been sometimes reported from hydrothermal ore veins related to the Tsushima granite [2, 4]. The Ni source seems to be hydrothermal fluids from the granite [4]. The present Ni detection in fluid inclusions from the miarolitic quartz supports the granitic magma origin of Ni.

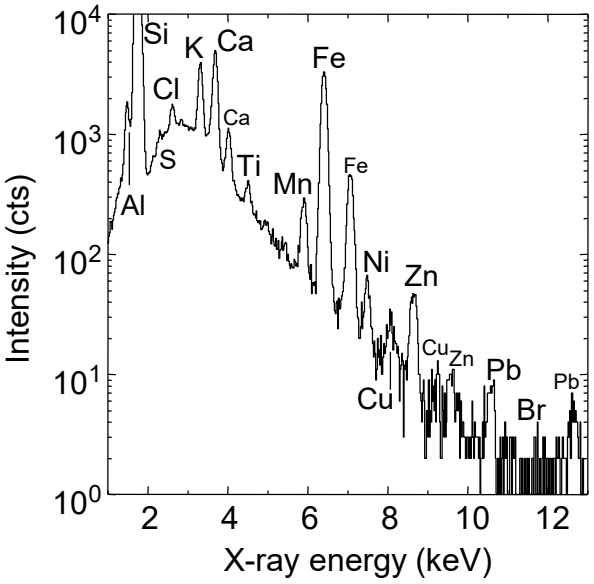

Fig. 2. PIXE spectrum of vapor-rich fluid inclusions in quartz crystal from miarolitic cavity at the Tsushima granite, Japan.

References

[1] S. R. Taylor and S. M. McLennan, The Continental Crust: Its Composition and Evolution, Blackwell Scientific, Oxford. 1985.

[2] N. Shimada and Y. Watanabe, Sci. Rep. Dep. Geol. Kyushu Univ. 11 (1973) 225.

[3] Y. Shiga, Mining Geol. 25 (1975) 27.

[4] N. Shimada, Mem. Fac. Sci., Kyushu Univ. Ser. D 23 (1977) 417.

[5] Y. Shiga, Mining Geol. 33 (1983) 385.

[6] N. Jackson et al., Econ. Geol. 84 (1989) 1101.

[7] K. Shin et al., Res. Geol., 59 (2009) 25.

[8] M. Kurosawa et al., Geochim. Cosmochim. Acta 182 (2016) 216.

[9] M. Kurosawa et al., Nucl. Instr. Meth. Phys. Res. B 266 (2008) 3633.

[10] W. Reuter et al., J. Appl. Phys. 46 (1975) 3194.

4.9 Physico-chemical properties of active layers controlling the boric acid rejection by polyamide composite reverse osmosis and nanofiltration membranes

R. Tanaka[1], M. Niinae[1], T. Suzuki[1]

State-of-the-art thin-film composite reverse osmosis (RO) and nanofiltration (NF) membranes consist of a nonwoven polyester layer (~50–150 μm) that backs an intermediate layer of polysulfone (~20–50 μm), which in turn supports an active layer of polyamide (< 100 nm) [1]. Among these three layers, the performance of the membrane was mainly determined by a polyamide active layer [2]. However, it is well-documented in the literatures [3, 4] that neutral and small molecules including H_3BO_3 are poorly rejected by state-of-the-art RO/NF membranes. Therefore, the objective of this study is to investigate physico-chemical properties of active layers controlling the boric acid (H_3BO_3) rejection by polyamide composite reverse osmosis and nanofiltration membranes. To achieve this objective, we measured the concentration of deprotonated carboxy group ($R\text{-}COO^-$) of polyamide active layer of 6 commercial RO/NF membranes by probing $R\text{-}COO^-$ with Ag^+ and quantifying the Ag^+ using Rutherford backscattering spectrometry.

All solutions were prepared using distilled deionized water with a resistivity greater than 18 MΩ cm (WA200, Yamato Scientific Co., Ltd., Tokyo, Japan). All reagents were purchased at guaranteed reagent grade quality from Nacalai Tesque, Inc. (Kyoto, Japan) or Wako Pure Chemical Industries, Ltd. (Osaka, Japan) and used without further purification. Saturation of $R\text{-}COO^-$ with Ag^+ at pH6.0 and 10.0 was performed according to the procedures reported in the literature [5]. Permeation experiments were performed with a cross-flow, closed-loop filtration system similar to that described in the literature [1]. The system had two flat-leaf cells in series and each cell had 155 cm^2 effective filtration area. The system was always operated at constant feed solution temperature of 24 ± 0.3ºC and pH = 6.0. For performance evaluation, the membrane samples were initially stabilized for three weeks at 2.5 MPa to allow for membrane compaction, using a feed solution containing 141 mM NaCl and 1.85 mM H_3BO_3.

Representative RBS spectra obtained for (a) polysulfone support and commercial RO membrane (M1), and (c) Ag^+-treated M1 membranes at pH6.0 and pH10.0 are shown in Fig. 1. Also shown are the fitted spectra obtained by using the software SIMNRA. Obviously, the Ag^+ peak is higher at pH10.0 than at pH6.0, which means that more fraction of R-COOH is deprotonated at higher pH. Next, we investigated the relationship between physico-chemical parameters obtained from charge density analysis (i.e., $R\text{-}COO^-$ concentrations at pH6.0 and pH10.0) and water/H_3BO_3 transport parameters obtained by modeling experimental data using the solution-diffusion model allowing for the existence of unhindered advection through nano-scale imperfections. However, as shown in Fig. 2 as an example, we could not find strong correlation between these values.

[1] Yamaguchi University

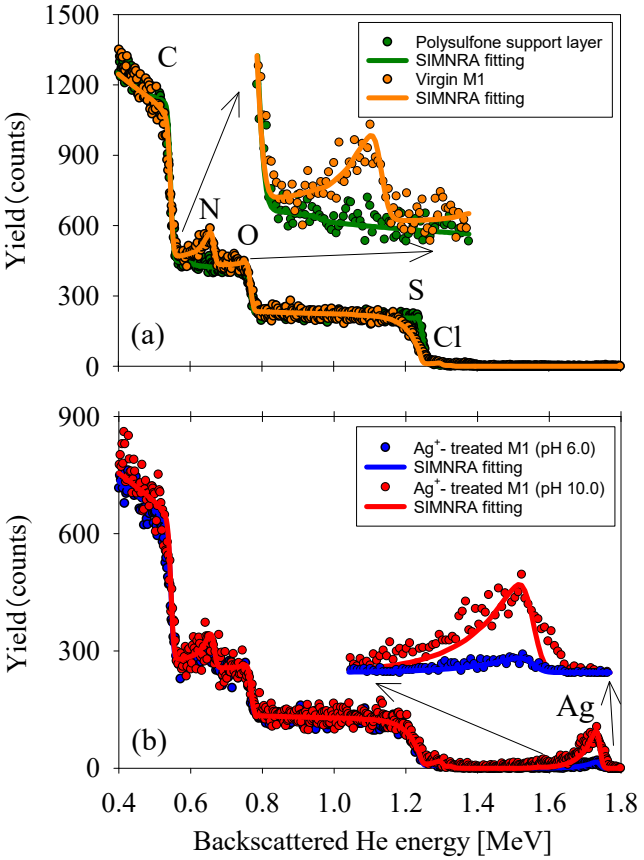

Fig. 1. Representative RBS spectra obtained for (a) polysulfone support and M1 membranes, and (b) Ag^{+}- treated M1 membrane at pH6.0 and pH10.0. The H/C ratio for M1 membrane was assumed to be 0.67 (value for fully aromatic polyamide). The average and standard deviation in Gamma distribution of active layer thickness were determined from the nitrogen peak, oxygen peak, and the energy shift of the frontal peak of sulfur.

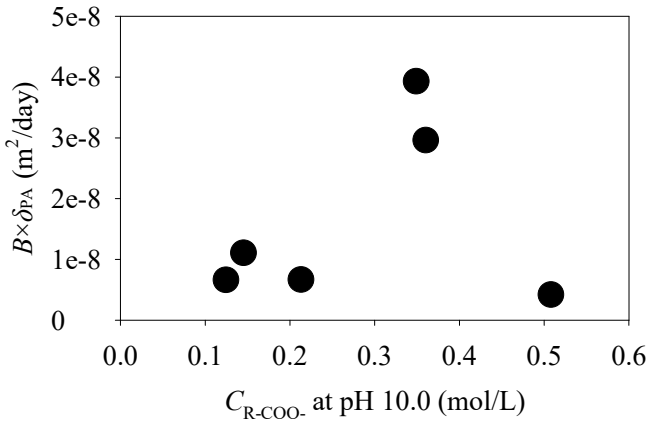

Fig. 2. Relationship between physico-chemical parameters obtained from charge density analysis and water/H_3BO_3 transport parameters obtained by modeling experimental data using the solution-diffusion model allowing for the existence of unhindered advection through nano-scale imperfections.

References

[1] T. Suzuki et al., Water Res. 100 (2016) 326.

[2] R. J. Petersen, J. Membr. Sci. 83 (1993) 81.

[3] B. Van der Bruggen et al., Water Res. 36 (2002) 1360.

[4] Y. Sato et al., Water Res. 36 (2002) 3371.

[5] O. Coronell et al., Environ. Sci. Technol. 45 (2011) 4513.

4.10 Thermoelectric SiGe film synthesized on a flexible plastic substrate

K. Toko, T. Suemasu

A composition tunable $Si_{1-x}Ge_x$ alloy has a wide range of applications, for example, to thermoelectric devices. We investigate the Al-induced layer exchange (ALILE) growth of $Si_{1-x}Ge_x$ on an insulator (SGOI). Preparation of the bilayered amorphous (a-) $Si_{1-x}Ge_x$ and Al of 50 nm thickness each on a SiO_2 glass substrate was performed at room temperature using radio frequency (RF) magnetron sputtering (base pressure: 3.0×10^{-4} Pa) with Ar plasma. The RF power was set to 50 W for all of the $Si_{1-x}Ge_x$ targets. The Ge compositions x in the prepared a-$Si_{1-x}Ge_x$ layers were determined to be 0, 0.15, 0.3, 0.6, 0.8, and 1 by Rutherford backscattering spectrometry (RBS). Between the two deposition cycles, the Al film was exposed to air for 30 min to form a native Al oxide layer as a diffusion-limiting layer. The samples were then annealed at 340–450°C in a N_2 ambient chamber with an in-situ optical microscopy system until the layer exchange was finished. The Al and AlO_x layers were then etched away with HF solution (HF: 1.5%) for 1 min.

The effect of the Ge fraction x in $Si_{1-x}Ge_x$ on layer exchange temperature range was examined. The higher the value of x, the lower the temperature range wherein the layer exchange occurred. This is indicative of the activation energy required for crystallization. Furthermore, the hole concentration p increased with increasing x and growth temperature. The variation of electrical conductivity σ with increasing x was observed to be directly proportional to p. Contrarily, there was no detectable variation of σ with respect to the growth temperature. Such observed behavior could be due to the balance between p and crystal quality because the grain size increases with decreasing growth temperature in ALILE. The electrical conductivities of the Si and Ge layers approached to those of bulk single crystals within one order of magnitude, despite these layers being polycrystalline. Such high σ may be attributed to the large grains, i.e., a few grain boundaries, in the ALILE grown layers. These results mean that p and σ can be controlled by adjusting x and the annealing temperature. The Seebeck coefficient S decreased with increasing p and x, which is a well-known phenomenon in SiGe. Here, S can be determined using the following equation:

$$S = \frac{k_B}{q}\left(-\log\frac{p}{p_0} + \delta\right) \quad (1)$$

where k_B is the Boltzmann constant, q is the elementary charge, p_0 is a constant given afterwards by eq. (2), and δ is a constant ≈ 1. This equation clearly illustrates the relationship between p and S. Furthermore, p_0 can be expressed as:

$$p_0 = \frac{1}{2}\left(\frac{2mk_BT}{\pi\hbar^2}\right)^{\frac{3}{2}} \quad (2)$$

where m is the effective mass of the hole, T is the absolute temperature, and $\hbar$ is Dirac's constant. For $Si_{1-x}Ge_x$, m decreases as x increases. Therefore, from eqs. (1) and (2), it can be deduced that S decreases with an increase in x. The power factor $P = S^2\sigma$ at room temperature (RT) increased with an increasing p

for $x \geq 0.8$, and the opposite trend was observed for $x \leq 0.6$. It is generally observed for SiGe that P improves as p approaches the order of 10^{20} cm^{-3}, and this is attributed to the increase in σ. Conversely, the observed grain size increasing with a decrease in growth temperature for ALILE-SiGe is responsible for the increase in σ. Therefore, the behavior of P for $x \leq 0.6$ could be highly attributed to the enlargement of grains due to low temperature growth. The maximum P of 430 $\mu W/mK^2$ was recorded for $x = 1$. By assuming a κ (thermal conductivity) value for 100-nm-thick SiGe films, the dimensionless figure of merit ZT was determined. In relative terms, ZT was observed to be maximum at $x = 0.6$. Therefore, for ALILE processed SiGe thermoelectric devices, $x = 0.6$ could be considered to be the optimum composition.

Since the growth temperature (350°C) of $Si_{0.4}Ge_{0.6}$ is lower than the heat resistance temperature of the plastic (polyimide) substrate, we developed ALILE-$Si_{0.4}Ge_{0.6}$ on a SiO_2-covered polyimide substrate. The processed $Si_{0.4}Ge_{0.6}$ films were of high quality as evidenced by the absence of cracks on the sample surface and a relatively high degree of film uniformity over the entire substrate. From the Hall effect measurement p was determined to be 5.8×10^{19} cm^{-3} and hence $\sigma = 157$ S/cm. Thus, we have achieved the growth of $Si_{0.4}Ge_{0.6}$ on a plastic substrate, though σ is slightly lower than those of the previous glass substrates. This may be due to the fact that the sample with a plastic substrate has a smaller grain size and higher p than those of glass. For the $Si_{0.4}Ge_{0.6}$ samples on a plastic substrate, P at RT is estimated to be 190 $\mu W/mK^2$. Although this value is about half of those of the $Si_{0.4}Ge_{0.6}$ samples on glass, it is the highest level among thermoelectric films synthesized directly on a flexible plastic substrate.

SiGe generally requires high processing temperatures to obtain high values of P mainly because high temperatures are required to activate impurities contained. The ALILE technique enabled us to achieve both high P (> 400 $\mu W/mK^2$) and low processing temperatures (< 400°C). The main reason for this achievement could be described as follows: for the Si and Ge layers, secondary ion mass spectrometry indicated that the Al concentrations in these two layers were of the same order as that of p. In addition, each of the amount of Al atoms in Si and Ge was almost equal to the solubility limit. These results suggest that the hole concentration in the $Si_{1-x}Ge_x$ layers is determined by the solubility limit of Al in $Si_{1-x}Ge_x$. Since the solubility limit increases with increasing temperature, this model accounts for the growth temperature dependence of p in the $Si_{1-x}Ge_x$ layers. Therefore, it could be implied that the advantage of the metal-induced layer exchange is not only crystallizing SiGe at low temperatures but also doping and activating impurities in a self-organizing manner during growth.

In conclusion, we demonstrated that SiGe formed by ALILE on insulating substrates has excellent characteristics as a thermoelectric film while maintaining low process temperatures (≤ 400°C). The SiGe layers introduce Al atoms to the solid solubility limit during growth, so that they are self-organically-highly-hole-doped without high-temperature-activation annealing. With this feature, a high power factor (430 $\mu W/mK^2$) and a low process temperature are simultaneously achieved. Furthermore, we developed the $Si_{0.4}Ge_{0.6}$ layer on a plastic substrate and obtained a power factor of 190 $\mu W/mK^2$. This value is the highest level among most thermoelectric films that are directly grown on a plastic substrate. The technology developed in this study is a promising candidate for its use in next-generation flexible thermoelectric devices.

The authors are grateful to Dr. D. Sekiba of UTTAC for RBS analyses.

4.11 Development of T-ERDA method for sensitive hydrogen-profiling

H. Naramoto, M. Sataka, H. Kudo, A. Yamazaki, K. Sasa

Interstitial hydrogen atoms can be incorporated into metals beyond the solubility limit by forming agglomerates with atomic defects under the defect-generation process. These agglomerates induce the serious deterioration on ductility in less-hydrogen soluble materials typically [1] and it is essential to know the 3-dimensional distribution of agglomerates in the materials. The hydrogen-recoiling resulting from the nuclear elastic scattering of the broad resonance type [2] is contributable for this purpose. Actually, for ten-MeV He on H the recoil cross section at ~0° is extremely larger than in the Rutherford case, for example, by a factor of up to 380. In this study, the angle-sensitive features of the transmission ERDA method are characterized for developing a more sensitive/reliable hydrogen-detection method.

Figure 1 shows the hydrogen recoil spectra for the uncalibarated detection angles, of which the origin must be determined precisely, under the normal incidence of 8 MeV $^4He^{2+}$ ions to the layered model film. Two recoil peaks at higher and lower channels correspond to two Mylar films separated by Al film at the 1st and the 3rd layer, respectively. The half-width of the 2nd recoil peak is wider by 35% than that of the 1st one because of the energy-straggling of incident ^4He ions when passing through the Al interlayer. The ratio of the 2nd to the 1st peak area, 0.74, can be accounted for in terms of the ratio of recoil cross-sections at the two layers, 0.81. One can see the symmetric shifts of hydrogen recoil peaks to the lower channel centering around +3.2° together with the broadening and the intensity decrease of the recoil peaks.

From Fig. 1, the recoil peak positions are plotted as a function of the uncalibarated detection angles in Fig. 2. The angular dependence is fitted with the expression of "$A\cos^2\theta$-$B(dE/dX)/\cos\theta$" considering the recoil kinetics and the followed energy loss of recoil protons as guided by a red solid curve, where A and B are constants, θ is the recoil angle (which of course equals to the calibrated detection angle), and (dE/dX) expresses the stopping power. In the relevant energy region, (dE/dX) in Al can be approximated to be a linear function of the proton travel distance (X). From the fitting, +3.13° should be taken as the calibrated 0° in the detector rotating system. Judging from the evaluated data, the angular range of ±4° around the calibrated 0°

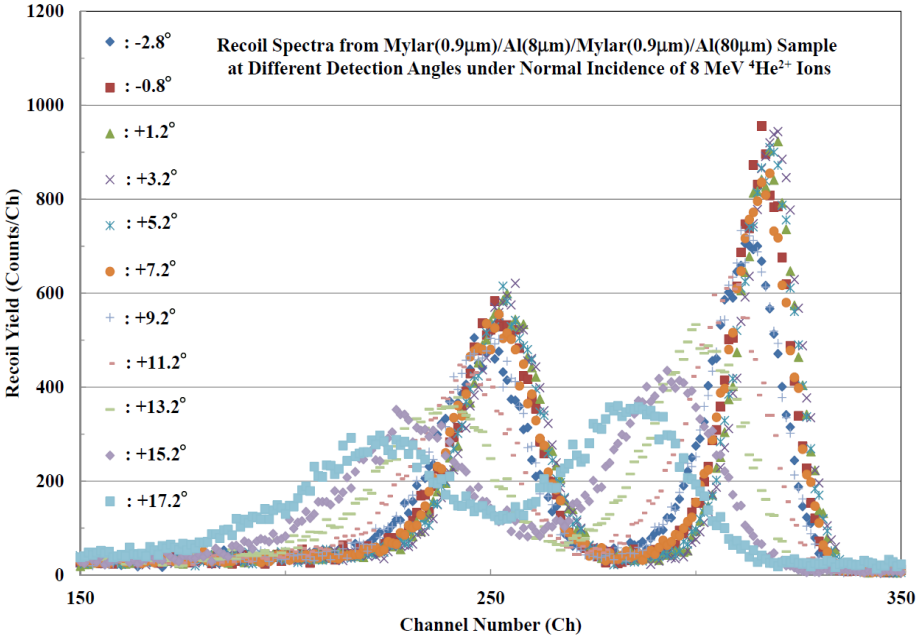

Fig. 1. Hydrogen recoil spectra for uncalibrated detection angles (nominal ones) under the normal incidence of 8 MeV $^4He^{2+}$ ions on the layered model film.

can be employed for the depth-sensitive hydrogen profiling without degrading the energy resolution. For the detailed hydrogen profiling, it is also important to set up the surface normal condition using the analysis beam. The calibration with a shift of 3.46° in the rotation angle of sample-stage was made by analyzing a series of spectra taken at the calibrated detection angle, i.e., the recoil angle of 0° .

Following the angle calibration procedure described, T-ERDA spectra of hydrogen adsorbed on as-rolled Al film surface were taken at three different energies covering the large recoil cross-sections. The hydrogen recoil intensities without background for 8, 9 and 10 MeV $^4He^{2+}$ ions reasonably correspond to the cross-sections for the nuclear elastic collisions at the relevant energies, but one can see the complicated background structure. In Al, the background seems to be originated from the two kinds of sources: 1) the high intensity background with the decaying nature in the lower energy region, and 2) the background with the prompt nature in the high energy region. Judging from the higher signal/noise ratio, 8 MeV $^4He^{2+}$ ions are suitable for the sensitive analysis. The recoil peak energy for 8 MeV $^4He^{2+}$ ions is close to the background tail but the situation can be improved by decreasing the Al thickness.

In conclusion, the precise angle-calibration procedure developed can be applied at each set of machine times, which enables reliable hydrogen profiling with the improved sensitivity and without degrading the energy resolution. The allowed acceptance of the ±4° recoil angle can be effectively employed for the 3-dimensional hydrogen-profiling combined with the microbeam-scanning. In general, hydrogen detection in a deeper layer requires higher-energy projectiles. Practically, we may use nuclear elastic collisions of He at 8-11 MeV, as is demonstrated in Fig. 3. For sophisticated T-ERDA, it is required to make a suitable choice of the analysis beam energy and the sample thickness depending on sample species.

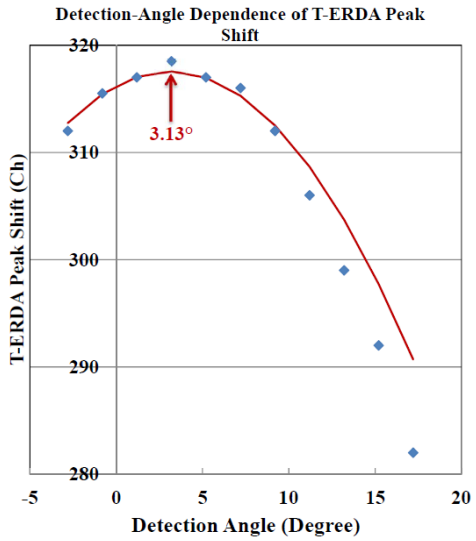

Fig. 2. Recoil peak positions as a function of the uncalibrated detection angle under the normal incidence of analysis beam. The data were fitted considering the recoil kinetics and the energy loss process of recoil protons.

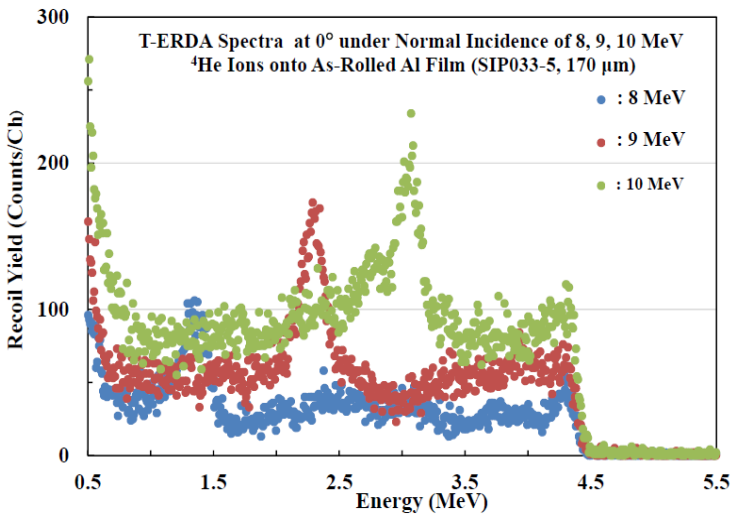

Fig. 3. T-ERDA spectra detected at the 0º recoil angle under the normal incidence of 8, 9, and 10 MeV $^4He^{2+}$ ions on the as-rolled Al film (170 μm). The recoil yields in the spectra are normalized to the accumulated charge of 10 μC.

References

[1] For example: S. Lynch, Corrosion Reviews 30 (2012) 105.

[2] For example: A. H. Bott et al., Surface and Coating Technology 70 (1995) 257.

4.12 Epitaxial strain-induced enhancement of low-temperature topotactic hydrogen substitution reaction of $SrTiO_3$

D. Kutsuzawa[1], Y. Hirose[1], D. Sekiba

Recently, oxyhydrides have been intensively studied because of their unique physical and/or chemical properties. For example, hydride (H^-) ions in perovskite-type $ATiO_xH_y$ (A = Ca, Sr, Ba) are highly labile, which enables low-temperature anion exchange reaction, such as H^-/D^-, H^-/O^{2-}, H^-/N^{3-}, etc. [1]. These oxyhydrides are also expected as catalysts for synthesis of NH_3. Thus far, transition metal oxyhydrides have been synthesized by low temperature topotactic hydrogen substitution of precursor oxides using metal hydrides (e.g. CaH_2) or high temperature high pressure reactions. The former has the advantage that it is applicable to precursor oxides not only in a fine powder form but also in an epitaxial thin film form, producing single-crystal like thin samples suitable for measuring the materials' intrinsic electrical transport properties. Another intriguing feature of epitaxial thin films is that their physical and/or chemical properties can be modified by epitaxial strain, as reported in various materials.

In this study, we synthesized $SrTiO_xH_y$ epitaxial thin films on various substrates by topotactic hydrogen substitution to examine the effect of epitaxial strain on the hydrogen content y. A quantitative analysis of the anion compositions by combination of Elastic Recoil Detection Analysis (ERDA) and Rutherford Backscattering Spectrometry (RBS) revealed that much hydrogen can be incorporated in the tensile-strained precursor $SrTiO_3$ film.

$SrTiO_xH_y$ thin films were prepared by a topotactic reaction reported previously [2]: First, precursor $SrTiO_3$ epitaxial thin films were grown on the following three single crystalline substrates with different lattice mismatch values $f = (a_{sub}-a_{film})/a_{film}$, where a_{sub} and a_{film} are the in-plane lattice constants of the substrate and the film ($SrTiO_3$; 3.905 Å), respectively; namely on the (001) plane of $LaSrAlO_4$ (LSAO) (tetragonal, a_{sub} = 3.75 Å, f = −4.0%), the (001) plane of LSAT (cubic, a_{sub} = 3.87 Å, f = −0.90%), and the (110) plane of $DyScO_3$ (DSO) (orthorhombic, a_{sub} = 3.94 Å under pseudo-cubic approximation, f = +0.89%) by pulsed laser deposition method. The crystal structure of the films was evaluated by XRD. The hydrogen amounts in the films were determined by ERDA using a 2.5 MeV $^4He^{2+}$ beam obtained from the 1MV Tandetron accelerator at UTTAC. The oxygen amounts in the films were evaluated by energy dispersive X-ray spectroscopy equipped with a scanning electron microscope (SEM-EDX) and cross-checked by heavy ion ERDA with a 38.4 MeV $^{35}Cl^{7+}$ beam performed using a 5 MV electrostatic tandem accelerator at MALT, University of Tokyo. In both the SEM-EDX and ^{35}Cl-ERDA measurements, a $SrTiO_3$ precursor film was used as the standard for the amount of oxygen in a film.

Figure 1(a) shows ^{4}He-ERDA spectra of the tensile-strained $SrTiO_3$/DSO films before and after the CaH_2 treatment. The precursor films show a weak hydrogen peak at ~400 channel originating from surface adsorbed water. The peak intensity of hydrogen significantly increased after the CaH_2 treatment and became stronger with increasing reaction time. Accompanied by this increased amount of hydrogen, a

[1] The University of Tokyo

decreased amount of oxygen was also observed by SEM-EDX, shown in Fig. 1(b), as well as by ^{35}Cl-ERDA, shown in Fig. 1(c). The decrease of the oxygen amount x and the increase of y in the $SrTiO_xH_y$ films are almost balanced within the experimental uncertainty (Fig. 1d), proving that substitution of hydrogen for oxygen occurred as previously reported for $SrTiO_3$/LSAT epitaxial thin films [2]. The substitution of hydrogen for oxygen was also confirmed in the $SrTiO_3$/LSAT and $SrTiO_3$/LSAO films after CaH_2 treatment (Fig. 1d). Notably, the amount of substituted hydrogen, i.e., y strongly depends on the substrates: the largest y is obtained by the tensile-strained $SrTiO_xH_y$/DSO films, followed by the almost relaxed $SrTiO_xH_y$/LSAO films, and subsequently by the compressive-strained $SrTiO_xH_y$/LSAT films.

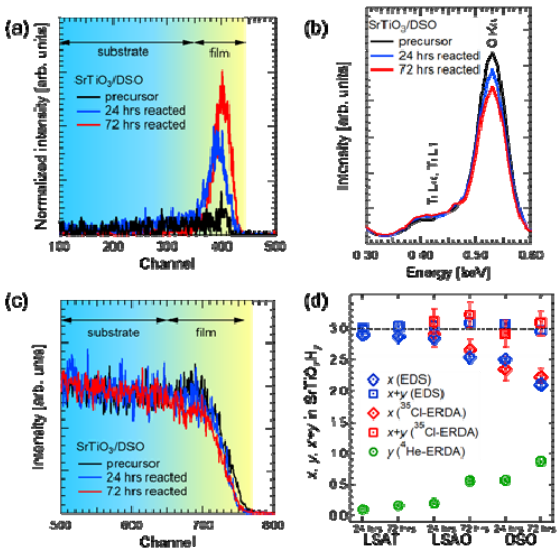

Fig. 1. (a) ^{4}He-ERDA spectra of the $SrTiO_3$/DSO films before and after CaH_2 treatment. (b) SEM-EDX spectra of the $SrTiO_3$/DSO before and after the CaH_2 treatment. (c) ^{35}Cl-ERDA spectra of oxygen recoils reconstructed from ΔE-E histogram of the $SrTiO_3$/DSO before and after the CaH_2 treatment. (d) Oxygen amount x, hydrogen amount y, and total anion amount $x + y$ in the $SrTiO_xH_y$ films on the three kinds of substrates after the CaH_2 treatment.

The hydrogen substitution reaction consists of two steps, the H^-/O^{2-} exchange at the surface and anion diffusion inside the film. We considered that the epitaxial strain affects the ionic diffusion in the films, as reported in various materials. It is reasonable to assume that diffusion of O^{2-} limits the reaction rate, since the diffusion of divalent O^{2-} is generally slower than that of monovalent H^- owing to stronger electrostatic interactions. Recent theoretical calculations on the O^{2-} diffusion in $SrTiO_3$ predicted that both the in-plane and out-of-plane diffusion of O^{2-} are enhanced by in-plane tensile strain [3], whereas the out-of-plane diffusion of O^{2-} is suppressed by in-plane compressive strain [4], supporting our hypothesis.

In conclusion, we revealed that the amount of substituted hydrogen is enhanced in tensile-strained $SrTiO_xH_y$/DSO films, probably owing to the promotion of oxygen diffusion. These results demonstrate the possibility for strain-engineering the chemical and physical properties of metal oxyhydrides.

References

[1] K. Masuda et al., J. Am. Chem. Soc. 137 (2015) 15315.

[2] T. Yajima et al., J. Am. Chem. Soc. 134 (2012) 8782.

[3] R. AL-Hamadany et al., J. Appl. Phys. 113 (2013) 224108.

[4] R. Al-Hamadany et al., J. Appl. Phys. 113 (2013) 024108.

4.13 Room and helium temperature Mössbauer experiments on Co-Ni ferrites to assess effect of synthesis method on magnetic properties

S. Sharmin, M. Kishimoto, H. Latiff, H. Yanagihara, E. Kita

Magnetic particles with a size on the order of several nanometers may exhibit superparamagnetic properties. The nanoparticles of metal oxides such as spinel ferrites possess great potentials for applications since they are relatively inert and their magnetic properties can be fine-tuned by chemical manipulation [1]. The aim of the present study was to characterize using Mössbauer spectroscopy the magnetic properties of Co-Ni ferrite nanoparticles synthesized by the successive methods of chemical co-precipitation, hydrothermal treatment, and etching in hydrochloric acid (HCl). A static measurement, such as magnetic susceptibility, sees the collective behaviors of paramagnetic clusters, while the Mössbauer effect can see the behavior of the individual species within a cluster [1].

In a typical synthesis method, 0.02 mole of $FeCl_3$-H_2O, 0.005 mole of $CoCl_2$, and 0.003 mole of $NiCl_2$ (Wako Pure Chemical Industries, Ltd, 99.0% purity) were dissolved in 20 mL of distilled water, to obtain a 2.5 times molar ratio of Fe^{3+} against (Co^{2+} + Ni^{2+}). The samples produced by chemical co-precipitation and then hydrothermal treatment are denoted by AP and HT respectively, while the samples produced as a result of etching after hydrothermal treatment are indicated by ET2 (HCl solution 2.0 mole/L), ET4 (4.0 mole/L), and ET6 (6.0 mole/L). The Mössbauer spectra of the samples were recorded in transmission geometry at room temperature (RT) and liquid helium temperature of 4.2 K (LT) using a ^{57}Co/Rh source.

The Mössbauer spectra collected for the AP sample (with diameter of only a few nanometers) at RT and 4.2 K are shown in Figs. 1 (a) and (b) respectively. A doublet is observed in the central part of the spectrum recorded at RT. When the temperature decreases below RT, the sextet is more pronounced. This doublet is attributed to superparamagnetism.

Figure 1 (c) shows the Mössbauer spectra recorded at RT and 4.2 K for the HT sample. Figure 1 (d) shows the Mössbauer spectra recorded at RT and liquid He temperature for the sample ET4. Both HT and ET4 samples exhibited similar spectra which could be fitted with two components. The two sextets correspond to the octahedral (A) and tetrahedral (B) Fe positions in the Co-Ni ferrite structure. From TEM studies, the diameters of the HT and ET4 samples were found to be equal to 30-40 nm. Superparamagnetic relaxation was found to be absent at RT in both HT and ET samples.

In sufficiently small nanoparticles, the direction of magnetization can randomly invert as a result of fluctuations in temperature. The typical time interval between two orientation inversions is given by the Nèel-Arrhenius equation,

$$\tau_N = \tau_0 exp(KV/k_B T) \quad (1)$$

where K is the magnetic anisotropy energy density of the particle, V is the volume of the particle, k_B is the Boltzmann constant and T is the temperature. τ_0 is the attempt time with a value between 10^{-9} and 10^{-10} s.

The characteristic measurement time in milliseconds, τ_1, corresponds to the Larmor precession period of the ^{57}Fe nucleus. For fine nanoparticles, the relaxation time, τ, is smaller than τ_1, and the magnetic fluctuation is so fast that the average internal magnetic hyperfine field at the ^{57}Fe nuclei is equal to zero. In this case, a

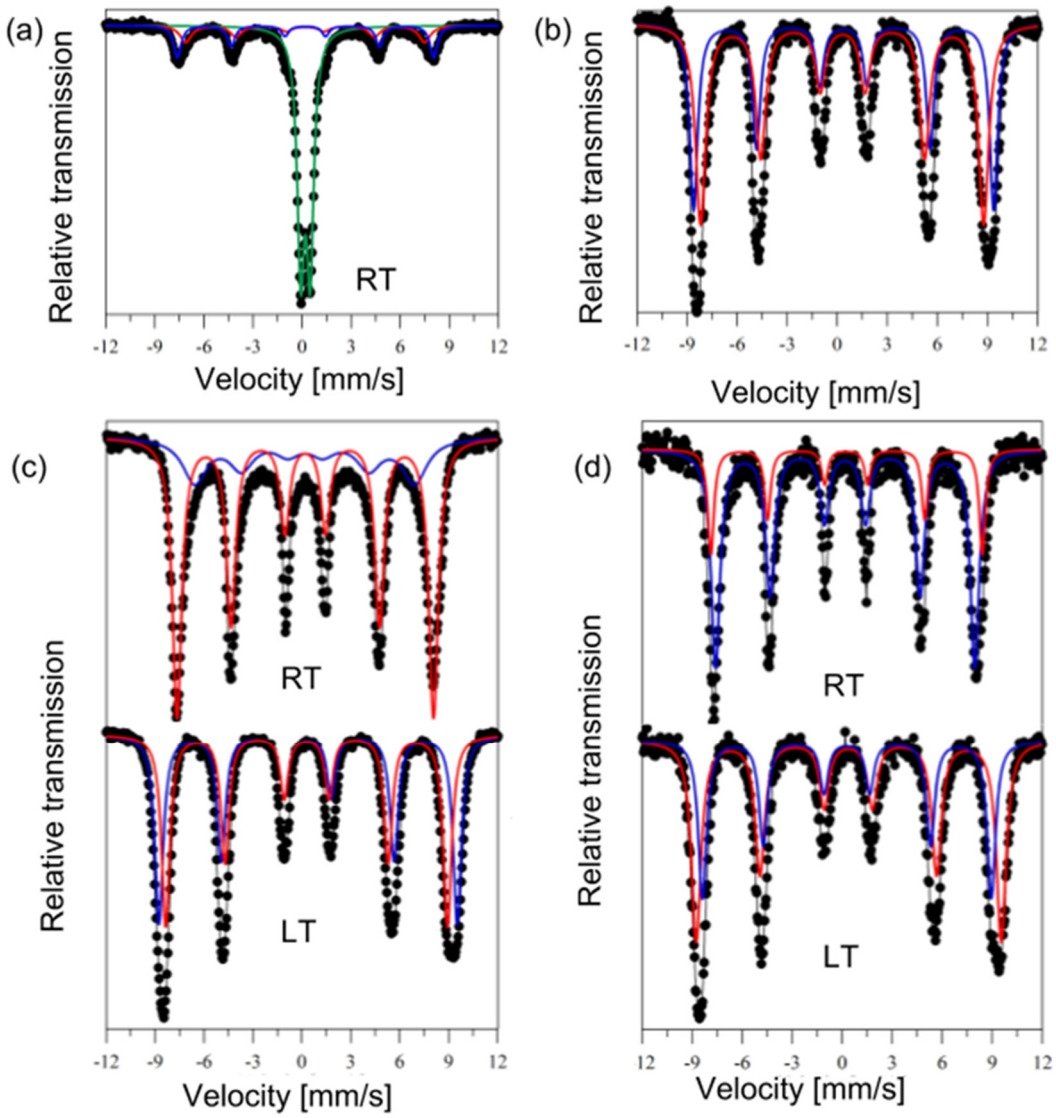

Fig. 1. ^{57}Fe Mössbauer spectra of Co-Ni ferrite nanoparticles for the AP sample obtained at RT (a) and at LT (b). ^{57}Fe Mössbauer spectra of Co-Ni ferrite nanoparticles for the HT (c) and ET4 samples (d) obtained at RT and LT.

doublet can be observed in the Mössbauer RT spectrum. As the temperature decreases, τ increases and becomes τ_1. If this occurs, some ^{57}Fe nuclei undergo rapid superparamagnetic relaxation and a doublet and sextet coexist in the pattern [3]. As temperature further decreases the relaxation of nanoparticles becomes even slower and the spectrum takes on the form of a sextet. The size of the nanoparticles increases significantly for the HT and ET samples, making the temperature at which $\tau = \tau_1$ much higher in these samples than RT. Thus it can be concluded that the magnetic properties of superparamagnetic Co-Ni ferrites depend on their size and method of synthesis. These results can provide a better understanding of the influence of different stages of synthesis condition on the magnetic properties of the Co-Ni ferrites.

References

[1] A.-D et al., Beni-Suef University Journal of Basic and Applied Sciences (2017).

[2] D. W. Collins et al., Mössbauer Effect Methodology, Springer, Boston, MA (1967) 103.

[3] Z. Surowiec et al., Nukleonika 62 (2017) 73.

[4] Q. Chen and Z. J. Zhang, Appl. Phys. Lett. 73 (1998) 3156.

4.14 Mössbauer spectroscopy study of spinel structured $Mn_xFe_2O_{4-\delta}$ particles under external magnetic field

H. Latiff, M. Kishimoto, E. Kita, H. Yanagihara

Magnetic anisotropy of spinel ferrites can be enhanced via the symmetry reduction approach using lattice distortion [1]. We proposed use of the Jahn-Teller (JT) effect of Cu^{2+} ions and reported on the coercivity enhancement in tetragonal $(Cu,Co)Fe_2O_4$ particles [2]. In this study, we used Mn^{3+} as the source of JT effect to increase the magnetization. ^{57}Fe Mössbauer experiments were performed for Mn ferrite particles to investigate the Fe^{3+} site distribution.

The Mn ferrite particles were synthesized by coprecipitation and hydrothermal methods. Aqueous solutions containing Mn^{2+} and Fe^{3+} with a ratio of 1.3 : 2 were mixed with NaOH aqueous solution to form precipitates, which were treated hydrothermally at 280°C. The particles as-prepared (AP) in this way were subsequently heat-treated (HT), i.e., annealed at 450°C in air to oxidize the Mn^{2+} to Mn^{3+}. The X-ray diffraction (XRD) patterns are shown in Fig. 1. For the AP sample, all the peaks are attributable to the cubic spinel phase. After heat-treated, splitting of the peaks is observed, except for the (400) peak. Primarily, the peak splitting is attributed to the JT effect of Mn^{3+} ions induced by the heat-treatment. In $CuFe_2O_4$, such peak splitting indicates the tetragonal spinel phase transition due to the JT effect. In this study, the (400) peak which accounts to the c-axis showed no sign of splitting after the heat treatment. However, the intensity ratios of the other split peaks indicate a compressed c-axis type of distortion (c/a<1).

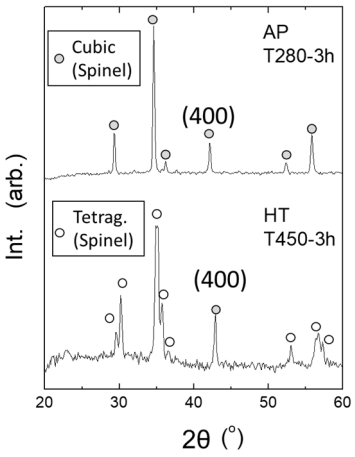

Fig. 1. XRD patterns of AP and HT samples of Mn ferrite particles.

Figures 2 and 3 show zero-field (0T) and applied-field (5T) ^{57}Fe Mössbauer spectra of the AP and HT samples recorded at RT, respectively. The 0T spectra are fitted to a combination of two magnetic sextets. The sub-spectra with higher and lower hyperfine field (H_{hf}) values are attributable to Fe^{3+}(A) and Fe^{3+}(B), respectively. The 0T literature values of the H_{hf} of the A and B sites are 48T and 43T, respectively [3]. The 0T spectra thus show considerably good agreement with the reported values within experimental errors. On the other hand, the 5T spectra are fitted to a combination of two magnetic quadruplets which are clearly separated. For the AP sample, the 5T spectrum composed of 3 sextets can be attributed to Fe (A↑), Fe (A↓), and Fe (B↓), where ↑ and ↓ represent the minor (parallel to H_{ext}) and the major (anti-parallel to H_{ext}) moments, respectively.

The fitting parameters used in Figs. 2 and 3 are listed in Table 1.The electric fields given in terms of Q. S. values are effectively zero for the AP sample, indicating a highly symmetrical structure. In contrast, for the HT sample there exists a non-zero value −0.189 mm/s for Fe(B) at 0T, indicating the presence of non-cubic structure, which is consistent with the XRD pattern. The I. S. of all sub-spectra ranges from 0.22 to 0.37 mm/s, indicating that they originate from Fe^{3+}, and not from Fe^{2+}. At 5T, the area populations of the Fe^{3+} ions distributed in the A and B sites are 50.7 and 49.3% for the AP sample; while 33 and 67% for the

HT sample, respectively. The Fe cation can be distributed as $[Fe]_A(Mn,Fe)_BO_4$ for the AP sample, and as $[Fe_{0.67},Mn_{0.33}]_A(Mn_{0.66},Fe_{1.34})_BO_4$ for the HT sample. If 33% of Mn in the A site are Mn^{3+} oxidized from Mn^{2+}, then there is a possible emergence of the JT effect by Mn^{3+} in the tetrahedral A site, causing a c/a<1 distortion of the system. Since there is no indication of the presence of Fe^{2+}, this suggests that instead of Fe^{3+} reduction to Fe^{2+}, the charge is likely balanced by the presence of lattice vacancy defect. The cation distribution for the HT sample is thus suggested as $[Fe_{0.67},Mn_{0.33}]_A(Mn_{0.66},Fe_{1.0}\square_{0.34})_BO_4$, where vacancy is represented by the symbol □.

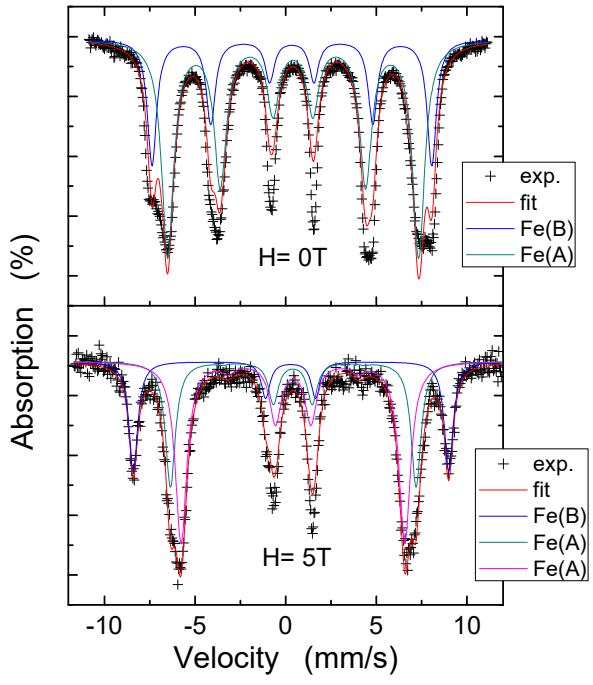

Fig. 2. RT ^{57}Fe Mössbauer spectra of as-prepared Mn ferrite particles at H_{ext} = 0T (top) and H_{ext} = 5T (bottom).

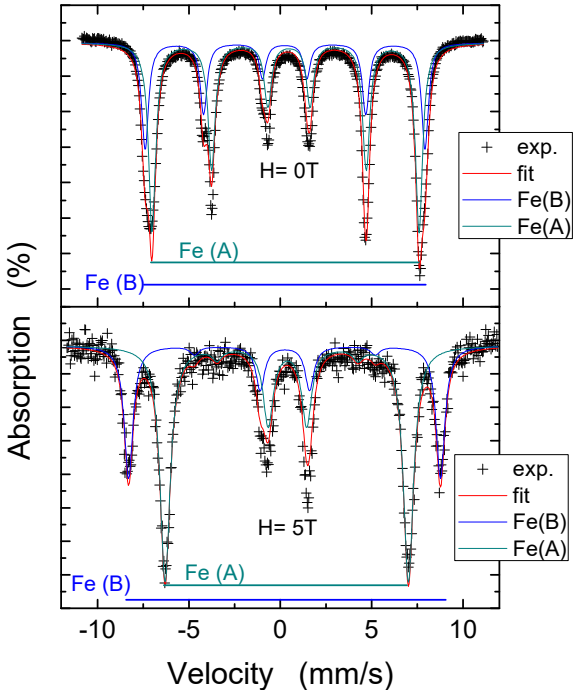

Fig. 3. RT ^{57}Fe Mössbauer spectra of heat-treated Mn ferrite particles at H_{ext} = 0T (top) and H_{ext} = 5T (bottom).

Table 1. Mössbauer fitting parameters.

Sample XRD pattern	H_{SCM} (T)	Line spectrum	$H_{h.f.}$ (T)	I. S. (mm/s)	Q. S. (mm/s)	L. W. (mm/s)	Area (%)	B/A
As-prepared (AP)	0	Fe^{3+} (A)	48	0.3368	0.005	0.6073	30.7	2.3
cubic		Fe^{3+} (B)	43	0.4033	0.009	0.7979	69.3	
	5	Fe^{3+} (A↑)	54.1	0.2787	0.024	0.5808	21.9	1
		Fe^{3+} (A↓)	42.1	0.4028	0.024	0.6637	28.8	
		Fe^{3+} (B↓)	38.4	0.4039	-0.013	0.77	49.3	
Heat-treated (HT)	0	Fe^{3+} (A)	47.7	0.2223	0.049	0.398	32.7	2.1
Non-cubic		Fe^{3+} (B)	45.5	0.3799	-0.189	0.4806	67.3	
	5	Fe^{3+} (A↑)	53.1	0.2416	-0.020	0.6628	33.3	2
		Fe^{3+} (B↓)	41.4	0.3740	-0.037	0.5822	66.7	

References

[1] T. Niizeki et al., Appl. Phys. Lett. 103 (2013) 162407.

[2] H. Latiff et al., IEEE Trans. Magn. 53 (2017) 9402304.

[3] G. A. Sawatzky et al., Phys. Letters 25A (1967) 147.

4.15 Magnetic properties of individual magnetite nanoparticles

H. Mamiya[1]

In recent years, the method for synthesizing magnetic nanoparticles has made remarkable progress. However, the true magnetic characteristics of the nanoparticles such as magnetic anisotropy are yet to be revealed due to possible interactions between nanoparticles. As a consequence, the application- oriented design of magnetic nanoparticles has become difficult. Thus in this study, we have prepared an ideal interaction-free magnetite nanoparticle system by coating magnetite particles with silica of enough shell thicknesses to clarify the true magnetic anisotropy of individual magnetite nanoparticles.

First, magnetite particles with average diameters ranging from 8 to 23 nm were synthesized. Then, these magnetite particles were coated with silica shell of various thicknesses between 0 and 33 nm. Their microscopic magnetic states were examined using ^{57}Fe Mössbauer spectroscopy, while their macroscopic magnetic properties were studied using SQUID magnetometry.

A typical ^{57}Fe Mössbauer spectrum is shown in Fig. 1. The presence of six lines in the spectrum thus indicates that its microscopic magnetic state is ferromagnetic. In the first-order reversal curve (FORC) diagrams, we can find that interaction field disappears with coating. In other words, the magnetite nanoparticles are magnetically isolated by the silica-shell, as expected. This fact can be confirmed by the proportionality between the isothermal remanent magnetization and the DC demagnetization remanence. Consequently, this advance enables us to study the true magnetic anisotropy of individual magnetite nanoparticles in the next step.

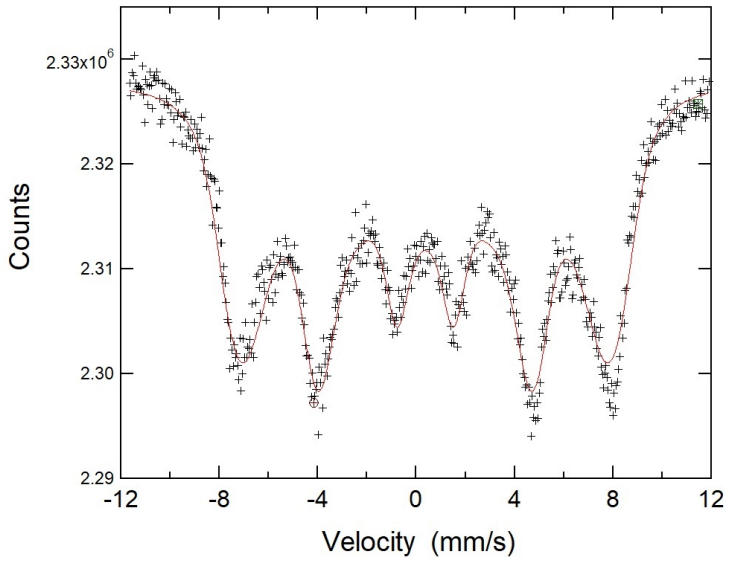

Fig. 1. Typical ^{57}Fe Mössbauer spectrum of the prepared magnetite nanoparticles.

[1] National Institute for Materials Science

5.

BEAM IRRADIATION EFFECT

5.1 Construction of efficient radiation experiment system

A. Nagata, A. Yasuda, H. Watanabe, T. Kameda

The purpose of this research is to improve the accuracy and efficiency of radiation tests [1]. For this purpose, a test support system was developed, and it was verified through radiation testing. Through the tests, the effectiveness of the test support system was confirmed and its points of improvement relative to previous methods were identified. In addition, for the purpose of evaluating the space applicability of a communication module using a commercial communication IC [2], radiation resistance testing was conducted and the radiation resistances of a communication module and microcontroller, which are considered as a control microcontroller, were evaluated.

In this study, the test support system is made to detect SEEs (Single Event Effects), reset equipment, and record automatically. The support system consists of current sensors, reset circuits, and processing units (Fig. 1). The processing units are connected to the monitoring PC in the monitoring room; thus, the status can be monitored and the power to the test pieces is controlled with the monitoring PC. Figure 1 shows the schematic view of the support system. The following requirements for the support system were tabulated and validated in advance. (1) Ability to turn off power automatically when the consumption current exceeds the threshold for the test piece. (2) Ability to detect SEL (Single Event Latch up) and SEU (Single Event Upset) of a test piece automatically and record voltages and currents during SEE occurrences along with the driving time taken from when power is supplied to the test piece to the occurrence of the SEE. (3) Ability to log the test. (4) Support system transmission of the consumption current, voltage, and occurrences of SEEs to the monitoring PC. (5) Ability to control the power to a test piece using the monitoring PC in the monitoring room.

In this experiment, the support system needs to reset the test pieces automatically and instantaneously in order to prevent them from breaking down owing to SELs. However, it is improbable for an SEU to cause destruction, and power must be supplied to test pieces until the occurrence of an SEL if an SEU is more likely to occur than an SEL. Therefore, an automatic reset for SEU detection by the processing unit was not adopted, but manual reset from the monitoring PC was used.

For the microcontroller, the test support system operated with automatic SEE detection and automatic resets as expected, and it was confirmed that automatic detection of SEEs and automatic resets for breakage prevention were effective. However, it was found that the support system could not detect the SELs of the communication module correctly using the conventional detection method because of the difference in the consumption current during transmission and during standby. In the conventional method, the threshold of the current value is set from approximately 1.5 to 2.0 times as much as the consumption current during normal driving, and when the consumption current exceeds this threshold, an SEL is detected. On the other hand, the consumption current of the communication module greatly differs between radio wave transmission and standby modes, and it is difficult to set the threshold value based on the current consumption value during normal driving.

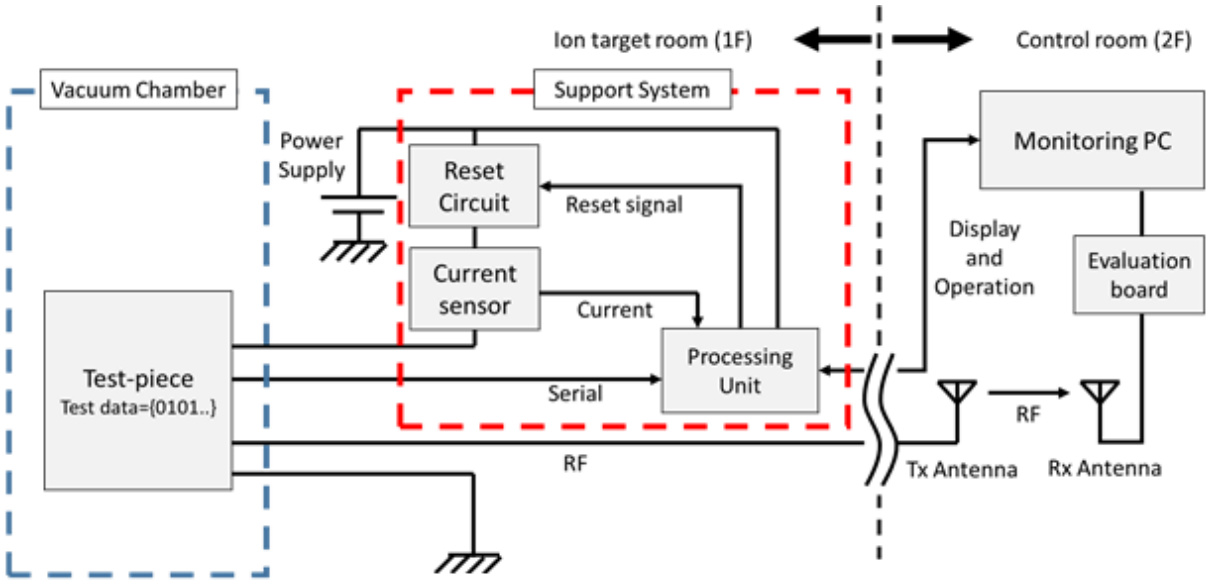

Fig. 1. System block diagram.

In conclusion, a test support system that can detect SEEs automatically and can automatically reset the equipment when SELs occur was studied and developed for the purpose of improving the accuracy and efficiency of radiation resistance tests. The test support system's effectiveness and improvement points were confirmed by using it in a radiation test experiment. Radiation resistance testing was conducted and the radiation resistance of consumer communication modules being considered for space applications were evaluated; specifically, microcontrollers considered as controllers for communication modules were tested. It is found that the automatic SEE detection function and the automatic reset function are effective for reducing the omission of SEE detection and reducing the risk of damage to test pieces. It is also found that the accuracy of test is expected to be improved by using the present test support system. On the other hand, the consumption current transition around an SEL of the communication module shows a different tendency from that of the microcontroller. Therefore, the SEL detection method must still be improved.

The authors would like to thank K. Sasa and M. Sataka of UTTAC for technical assistance with the experiments.

References

[1] V. M. Placinta et al., Romanian Journal of Physics 62 (2017) 903.

[2] N. Ikeda et al., Transactions of the Institute of Electronics, Information and Communication Engineers, Series B 88 (2005) 108.

5.2 Comparison of LET versus SEU cross section curves for irradiation with energetic ions and with pulsed laser

K. Takeuchi, Y. Tsuchiya, K. Sakamoto, K. Yukumatsu, H. Shindo[1], M. Sataka, K. Sasa

Commercial off-the-shelf (COTS) electronic parts are widely employed especially for small satellites nowadays since the cost can be reduced efficiently. When selecting commercial parts for space application, the most concerned issue is radiation effects: Single Event Upset (SEU), Single Event Latch-up (SEL), Total Ionizing Dose (TID), and so on. Because COTS parts do not have enough radiation tolerance in many cases, accurate estimation of the error rate is necessary for practical use. The cross section of COTS parts for radiation effects noted above changes significantly in a narrow and low range of linear energy transfer (LET). Therefore, various radiation ion sources are needed to determine the accurate device cross section and the error rate.

A new vacuum chamber for the irradiation test, as shown in Fig. 1, was built in the beam line of the UTTAC 6MV tandem accelerator which generates energetic ions with various LET values by changing the acceleration voltage. This report describes evaluation results of a 9M bit SRAM device using the facility. In addition, we study the pulsed laser technique to estimate the cross section curve [1], which could be an alternative tool for the irradiation test procedure.

The vacuum chamber at UTTAC is equipped with various types of feedthroughs and a three-axis goniometer stage to set electronic parts at a desired position precisely. Besides, de-capped photo-diode sensors were placed next to the device to count the ion beam flux. Figure 2 shows the LET versus SEU cross section curve of the SRAM device. The plots in blue and red were obtained at UTTAC and the Takasaki Ion Accelerators for Advanced Radiation Application (TIARA), respectively. The data obtained at UTTAC is compatible as a quantitative evaluation with other measurements because they are in good agreement between the facilities. Li ion was selected as a radiation source to determine the accurate cross section around the LET range of 0.7 to 1.4 MeV/(mg/cm^2) where the cross section changes significantly. The device error rate under a certain radiation environment can be calculated from the acquired characteristics of the curve.

We study another approach to determine the cross section curve using the pulsed laser technique to simplify the irradiation test procedure for COTS parts. The backside of the SRAM device was drilled so that the pulsed laser beam could reach the sensitive area of the transistors. Figure 3 shows a comparison result between the heavy ion at UTTAC and the pulsed laser. The LET value of the pulsed laser experiment is calculated as a function of the laser intensity and the physical parameters associating with the test conditions [1]. The saturated cross section value is consistent with the result by the heavy ions. However, when looking at the region of the small cross section, the calculated LET values are not matched with the heavy ion results. It would be caused by the difference between the laser spot size and the transistor sensitivity area and/or the laser intensity profile. Further investigation of the disagreement will be required.

Fig. 1. The vacuum chamber at UTTAC for irradiation test of electronic parts.

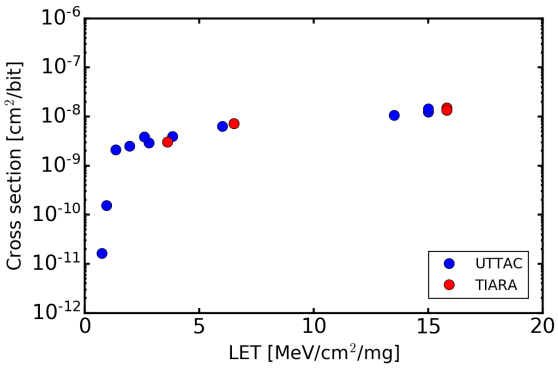

Fig. 2. SEU cross section vs. LET, obtained from the experiments at UTTAC and TIARA.

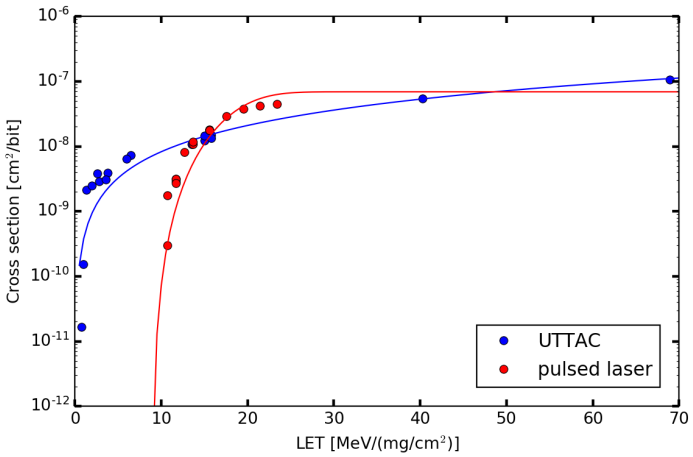

Fig. 3. SEU cross sections determined from the experiments at UTTAC and the pulsed laser technique.

Reference

[1] S. P. Buchner et al., IEEE Transactions on Nuclear Science 60 (2013) 1852.

[1] Japan Aerospace Exploration Agency, 2-1-1 Sengen, Tsukuba-city, Ibaraki, JAPAN

6.

LIST OF PUBLICATIONS AND PRESENTATIONS

6.1 Journals

ACCELERATOR AND RELATED FACILITIES

1. A. Yamazaki, K. Sasa, S. Ishii, M. Kurosawa, S. Tomita, Y. Shiina, S. Shiki, G. Fujii, M. Ukibe, M. Ohkubo, A. Uedono, E. Kita, Development of a microbeam PIXE system for additive light elements in structural materials, Nuclear Instruments and Methods in Physics Research B, 404 92-95 (2017).

NUCLEAR AND ATOMIC PHYSICS

1. T. Tanaka, Y. Narikiyo, K. Morita, K. Fujita, D. Kaji, K. Morimoto, S. Yamaki, Y. Wakabayashi, K. Tanaka, M. Takeyama, A. Yoneda, H. Haba, Y. Komori, S. Yanou, B. J.-P. Gall, Z. Asfari, H. Faure, H. Hasebe, M. Huang, J. Kanaya, M. Murakami, A. Yoshida, T. Yamaguchi, F. Tokanai, T. Yoshida, S. Yamamoto, Y. Yamano, K. Watanabe, S. Ishizawa, M. Asai, R. Aono, S. Goto, K. Katori, and K. Hagino, Determination of fusion barrier distributions from quasielastic scattering cross sections towards superheavy nuclei synthesis, J. Phys. Soc. Jpn. 87, 014201/1-9 (2018).

2. Q. Zeng, M. Wang, X. H. Zhou, Y. H. Zhang, X. L. Tu, X. C. Chen, X. Xu, Yu. A. Litvinov, H. S. Xu, K. Blaum, R. J. Chen, C. Y. Fu, Z. Ge, W. J. Huang, H. F. Li, J. H. Liu, B. Mei, P. Shuai, M. Si, B. H. Sun, M. Z. Sun, Q. Wang, G. Q. Xiao, Y. M. Xing, T. Yamaguchi, X. L. Yan, J. C. Yang, Y. J. Yuan, Y. D. Zang, P. Zhang, W. Zhang, and X. Zhou, Half-life measurement of short-lived $^{94m}Ru^{44+}$ using isochronous mass spectrometry, Physical Review C 96, 031303(R)/1-5 (2017).

3. J. C. Zamora, T. Aumann, S. Bagchi, S. Boenig, M. Csatlos, I. Dillmann, C. Dimopoulou, P. Egelhof, V. Eremin, T. Furuno, H. Geissel, R. Gernhaeuser, M. N. Harakeh, A.-L. Hartig, S. Ilieva, N. Kalantar-Nayestanaki, O. Kiselev, H. Kollmus, C. Kozhuharov, A. Krasznahorkay, Th. Kroell, M. Kuilman, S. Litvinov, Yu. A. Litvinov, M. Mahjour-Shafiei, M. Mutterer, D. Nagae, M. A. Najafi, C. Nociforo, F. Nolden, U. Popp, C. Rigollet, S. Roy, C. Scheidenberger, M. von Schmid, M. Steck, B. Streicher, L. Stuhl, M. Thuerauf, T. Uesaka, H. Weick, J. S. Winfield, D. Winters, P. J. Woods, T. Yamaguchi, K. Yue, and J. Zenihiro, Nuclear-matter radius studies from ^{58}Ni (α, α) experiments at the GSI Experimental Storage Ring with the EXL facility, Physical Review C 96, 034617/1-6 (2017).

4. E. Miyata, M. Takechi, T. Ohtsubo, M. Fukuda, D. Nishimura, K. Abe, K. Aoki, A. Ikeda, T. Izumikawa, H. Oikawa, K. Ohnishi, S. Ohmika, I. Kato, Y. Kanke, N. Kanda, R. Kanbe, H. Kikuchi, A. Kitagawa, S. Sato, H. Shimamura, J. Shimaya, S. Suzuki, T. Suzuki, R. Takagaki, H. Takahashi, Y. Takei, Y. Takeuchi, T. Takenouchi, N. Tadano, M. Tanaka, Y. Tanaka, K. Chikaato, H. Du, J. Nagumo, K. Nishizuka, T. Nishimura, S. Fukuda, M. Machida, A. Mizukami, M. Mihara, J. Muraoka, S. Yagi, S. Yamaoka, T. Yamaguchi, K. Yokoyama, Development of high resolution TOF detector for RI beams using Cherenkov radiation, Acta Phys. Pol. B 48, 409-412 (2017).

5. H. Du, M. Fukuda, D. Nishimura, M. Takechi, T. Suzuki, Y. Tanaka, I. Kato, M. Tanaka, K. Abe, T. Izumikawa, H. Oikawa, T. Ohtsubo, J. Ohno, Y. Kanke, H. Kikuchi, A. Kitagawa, S. Sato, U. Sayama, J. Shimaya, S. Suzuki, Y. Takeuchi, T. Takemoto, N. Tadano, R. Tamura, J. Nagumo, K. Nishizuka, S. Fukuda, K. Hori, S. Matsunaga, A. Mizukami, M. Mihara, E. Miyata, D. Murooka, S. Yamaoka, T. Yamaguchi, Nuclear structure of ^{15,16}C via reaction cross-section measurements, Acta Phys. Pol. B 48, 473-479 (2017).

6. M. Tanaka, M. Fukuda, D. Nishimura, M. Takechi, S. Suzuki, H. Du, Y. Tanaka, K. Aoki, S. Fukuda, A. Honma, T. Izumikawa, Y. Kamisho, N. Kanda, I. Kato, Y. Kanke, A. Kitagawa, J. Kohno, M. Machida, K. Matsuta, M. Mihara, E. Miyata, Y. Morita, J. Muraoka, D. Murooka, T. Nagai, M. Nagashima, K. Ohnishi, J. Ohno, T. Ohtsubo, H. Oikawa, S. Sato, H. Shimamura, T. Sugihara, T. Suzuki, N. Tadano, R. Takagaki, Y. Takei, A. Takenouchi, S. Yagi, T. Yamaguchi, S. Yamaki, S. Yamaoka, Reaction cross sections for $^{13\text{-}15}$B and one-neutron halo in ^{14}B, Acta Phys. Pol. B 48, 461-466 (2017).

7. A. Homma, M. Takechi, T. Ohtsubo, D. Nishimura, M. Fukuda, T. Suzuki, T. Yamaguchi, T. Kuboki, A. Ozawa , S. Suzuki , H. Ooishi , T. Moriguchi , T. Sumikawa, H. Geissel, N. Aoi, R.-J. Chen, D.-Q. Fang, N. Fukuda, S. Fukuoka, H. Furuki, N. Inaba, N. Ishibashi, T. Ito, T. Izumikawa, D. Kameda, T. Kubo, M. Lantz, C. S. Lee, Y.-G. Ma, M. Mihara, S. Momota, D. Nagae, R. Nishikiori, T. Niwa, T. Ohnishi, K. Okumura, T. Ogura, M. Nagashima, H. Sakurai, K. Sato, Y. Shimbara, H. Suzuki, H. Takeda, S. Takeuchi, K. Tanaka, H. Uenishi, M. Winkler, Y. Yanagisawa, Measurements of interaction cross sections for $^{19\text{-}27}$F isotopes, JPS Conf. Proc. 14, 021010/1-3 (2017).

8. K. Nishizuka, M. Takechi, T. Ohtsubo, D. Nishimura, M. Fukuda, K. Aoki, K. Abe, A. Ikeda, T. Izumikawa, H. Oikawa, K. Ohnishi, J. Ohno, S. Ohmika, I. Kato, Y. Kanke, S. Kanbe, N. Kanda, H. Kikuchi, A. Kitagawa, S. Sato, U. Sayama, J. Shimaya, T. Sugihara, S. Suzuki, T. Suzuki, H. Takahashi, Y. Taguchi, Y. Takei, Y. Takeuchi, A. Takenouchi, T. Takemoto, N. Tadano, M. Tanaka, Y. Tanaka, K. Chikaato, H. Du, T. Nagai, J. Nagumo, S. Fukuda, K. Hori, A. Honma, M. Machida, S. Matsunaga, A. Mizukami, M. Mihara, E. Miyata, D. Murooka, S. Yagi, S. Yamaoka, T. Yamaguchi, K Yokoyama, Measurements of reaction cross sections for $^{9\text{-}11}$C, JPS Conf. Proc. 14, 021015/1-3 (2017).

9. K. Sawahata, A. Ozawa, Y. Saito, Y. Abe, Y. Ichikawa, N. Inaba, Y. Ishibashi, A. Kitagawa, S. Matsunaga, T. Moriguchi, D. Nagae, S. Okada, S. Sato, S. Suzuki, T. Suzuki, Y. Takeuchi, T. Yamaguchi, J. Zenihiro, Investigations of charge-changing processes for light proton-rich nuclei on carbon and solid-hydrogen targets, Nuclear Physics A 961, 142-153 (2017).

10. D. Kaji, K. Morita, K. Morimoto, H. Haba, M. Asai, K. Fujita, Z. Gan, H. Geissel, H. Hasebe, S. Hofmann, M. Huang, Y. Komori, L. Ma, J. Maurer, M. Murakami, M. Takeyama, F. Tokanai, T. Tanaka, Y. Wakabayashi, T. Yamaguchi, S. Yamaki, and A. Yoshida, Study of the Reaction ^{48}Ca + ^{248}Cm → ^{296}Lv* at RIKEN-GARIS, J. Phys. Soc. Jpn 86, 034201/1-7 (2017).

11. P. Zhang, X. Xu, P. Shuai, R.J. Chen, X.L. Yan, Y.H. Zhang, M. Wang, Yu.A. Litvinov, K. Blaum, H.S. Xu, T. Bao, X.C. Chen, H. Chen, C.Y. Fu, J.J. He, S. Kubono, Y.H. Lam, D.W. Liu, R.S. Mao, X.W. Ma, M.Z. Sun, X.L. Tu, Y.M. Xing, J.C. Yang, Y.J. Yuan, Q. Zeng, X. Zhou, X.H. Zhou, W.L. Zhan, S. Litvinov, G. Audi, T. Uesaka, Y. Yamaguchi, T. Yamaguchi, A. Ozawa, B.H. Sun, Y. Sun, F.R. Xu, High-precision Q_{EC} values of super allowed 0^+ -> 0^+ β-emitters ^{46}Cr, ^{50}Fe, and ^{54}Ni, Phys. Lett. B 767, 20-24 (2017).

12. X. L. Tu, A. Kelic-Heil, Yu. A. Litvinov, Zs. Podolyak, Y. H. Zhang, W. J. Huang, H. S. Xu, K. Blaum, F. Bosch, R. J. Chen, X. C. Chen, C. Y. Fu, B. S. Gao, Z. Ge, Z. G. Hu, D. W. Liu, S. A. Litvinov, X. W. Ma, R. S. Mao, B. Mei, P. Shuai, B. H. Sun, Y. Sun, Z. Y. Sun, P. M. Walker, M. Wang, N. Winckler, J. W. Xia, G. Q. Xiao, Y. M. Xing, X. Xu, T. Yamaguchi, X. L. Yan, J. C. Yang, Y. J. Yuan, Q. Zeng, W. Zhang, H. W. Zhao, T. C. Zhao, and X. H. Zhou, Application of isochronous mass spectrometry for the study of angular momentum population in projectile fragmentation reactions, Physical Review C 95, 014610/1-6 (2017).

13. Y. Hirayama, Y.X. Watanabe, M. Mukai, M. Oyaizu, M. Ahmed, H. Ishiyama, S.C. Jeong, Y. Kakiguchi, S. Kimura, J.Y. Moon, J.H. Park, P. Schury, M. Wada, H. Miyatake, Doughnut-shaped gas cell for KEK Isotope Separation System, Nuclear Instruments and Methods in Physics Research B 412, 11 (2017).

14. Y. Hirayama, M. Mukai, Y. X. Watanabe, M. Ahmed, S. C. Jeong, H. S. Jung, Y. Kakiguchi, S. Kanaya, S. Kimura, J. Y. Moon, T. Nakatsukasa, M. Oyaizu, J. H. Park, P. Schury, A. Taniguchi, M. Wada, K. Washiyama, H. Watanabe, and H. Miyatake, In-gas-cell laser spectroscopy of the magnetic dipole moment of the N ≈126 isotope ^{199}Pt, Physical Review C 96 (2017) 014307.

15. Y. Hirayama, M. Mukai, Y. Watanabe, M. Oyaizu, M. Ahmed, Y. Kakiguchi, S. Kimura, Ionization cross section, pressure shift and isotope shift measurements of osmium H. Miyatake, P. Schury, M. Wada and Sun-Chan Jeong, Ionization cross section, pressure shift and isotope shift measurements of osmium, J. Phys. B: At. Mol. Opt. Phys. 50 (2017) 215203.

16. M. Mukai, Y. Hirayama, Y.X. Watanabe, P. Schury, H.S. Jung, M. Ahmed, H. Haba, H. Ishiyama, S.C. Jeong, Y. Kakiguchi, S. Kimura, J.Y. Moon, M. Oyaizu, A. Ozawa, J.H. Park, H. Ueno, M. Wada, and H. Miyatake, High-efficiency and low-background multi-segmented proportional gas counter for β-decay spectroscopy, Nuclear Instruments and Methods in Physics Research A 884,1 (2018).

ACCELERATOR MASS SPECTROMETRY

1. Yukihiko Satou, Keisuke Sueki, Kimikazu Sasa, Hideki Yoshikawa, Shigeo Nakama, Haruka Minowa, Yoshinari Abe, Izumi Nakai, Takahiro Ono, Kouji Adachi and Yasuhito Igarashi, Analysis of two forms of radioactive particles emitted during the early stages of the Fukushima Dai-ichi Nuclear Power Station accident, Geochemical Journal, Vol. 52, 137-143, 2018. doi:10.2343/geochemj.2.0514

2. Masumi Matsumura, Kimikazu Sasa, Tetsuya Matsunaka, Keisuke Sueki, Tsutomu Takahashi and Hiroyuki Matsuzaki, Temporal variation of iodine-129 in rainwater at Tsukuba before and after the Fukushima Daiichi Nuclear Power Plant accident, Geochemical Journal, Vol. 52, 155-162, 2018. doi:10.2343/geochemj.2.0504

3. Seiji Hosoya, Kimikazu Sasa, Tetsuya Matsunaka, Tsutomu Takahashi, Masumi Matsumura, Hiroshi Matsumura, Mark Sundquist, Mark Stodola, Keisuke Sueki, Optimization of a ΔE - E detector for 41Ca AMS, Nuclear Instruments and Methods in Physics Research B, 406, 268-271, 2017. DOI: 10.1016/j.nimb.2017.03.161

BEAM AND ISOTOPE APPLICATIONS

1. A. Uedono, S. Takashima, M. Edo, K. Ueno, H. Matsuyama, W. Egger, T. Koschine, C. Hugenschmidt, M. Dickmann, K. Kojima, S. F. Chichibu, and S. Ishibashi, Carrier trapping by vacancy-type defects in Mg-implanted GaN studied using monoenergetic positron beams, Phys. Stat. Sol. B 2017, 1700521(1-9). [DOI: 10.1002/pssb.201700521]

2. L. V. Devi, S. Sellaiyan, T. Selvalakshmi, H.J. Zhang, A. Uedono, K. Sivaji, S. Sankar, Synthesis, defect characterization and photocatalytic degradation efficiency of Tb doped CuO nanoparticles, Adv. Powder Tech. 28, (2017) 3026-3038. [DOI: 10.1016/j.apt.2017.09.013]

3. S. R. Aid, T. Uneme, N. Wakabayashi, K. Yamazaki, A. Uedono, and S. Matsumoto, Carrier activation in Mg implanted GaN by short wavelength Nd:YAG laser thermal annealing, Phys. Stat. Sol. A 214, 1700225(1-5) (2017). [DOI: 10.1002/pssa.201700225]

4. A. Uedono, T. Tanaka, N. Ito, K. Nakahara, W. Egger, C. Hugenschmidt, S. Ishibashi, and M. Sumiya, Electron capture by vacancy-type defects in carbon-doped GaN studied using monoenergetic positron beams, Thin Solid Films 639, (2017) 78-83. [DOI: 10.1016/j.tsf.2017.08.021]

5. A. Uedono, M. Imanishi, M. Imade, M. Yoshimura, S. Ishibashi, M. Sumiya, and Y. Mori, Vacancy-type defects in bulk GaN grown by the Na-flux method probed using positron annihilation, J. Cryst. Growth 475, (2017) 261-265. [DOI: 10.1016/j.jcrysgro.2017.06.027]

6. L. V. Devi, T. Selvalakshmi, S. Sellaiyan, A. Uedono, K. Sivaji, S. Sankar, Effect of La doping on the lattice defects and photoluminescence properties of CuO, J. Alloys & Comp. 709, (2017) 496-504. [DOI: 10.1016/j.jallcom.2017.03.148]

7. H. J. Zhang, S. Sellaiyan, T. Kakizaki, A. Uedono, Y. Taniguchi, K. Hayashi, Effect of Free-Volume Holes on Dynamic Mechanical Properties of Epoxy Resins for Carbon-Fiber-Reinforced Polymers, Macromolecules 50, (2017) 3933-3942. [DOI: 10.1021/acs.macromol.7b00472]

8. Y. Mizushima, Y. Kim, T. Nakamura, A. Uedono, and T. Ohba, Behavior of copper contamination on backside damage for ultra-thin silicon three dimensional stacking structure, Microelectronic Engineering 167, 23 (2017).

9. F. Inoue, A. Jourdain, L. Peng, A. Phommahaxay, J. De Vos, K. J. Rebibis, A. Miller, E. Sleeckx, E. Beyne, and A. Uedono, Influence of Si wafer thinning processes on (sub)surface defects, Applied Surface Science 404, 82 (2017).

10. S. F. Chichibu, K. Kojima, A. Uedono, and Y. Sato, Defect-Resistant Radiative Performance of m-Plane Immiscible Al1-xInxN Epitaxial Nanostructures for Deep-Ultraviolet and Visible Polarized Light Emitters, Advanced Materials 29, 1603644 (2017). [DOI: 10.1002/adma.201603644]

11. S. Ishibashi, H. Kino, A. Uedono, T. Miyake, and K. Terakura, Prediction of positron-annihilation parameters for vacancy-type defects in ternary alloy semiconductors by data-scientific approach, J. Phys.: Conf. Ser. 791, 012023(1-5) (2017). [DOI: 1088/1742-6596/791/1/012023]

12. K. Kojima, S. Takashima, M. Edo, K. Ueno, M. Shimizu, T. Takahashi, S. Ishibashi, A. Uedono, and S. F. Chichibu, Nitrogen vacancies as a common element of the green luminescence and nonradiative recombination centers in Mg-implanted GaN layers formed on a GaN substrate, APEX 10, 061002 (2017). [https://doi.org/10.7567/APEX.10.061002]

13. M. Saito, T. Tanabe, M. Lintuluoto, E. B. Starikov, K. Noda, T. Majima, S. Tomita and K. Takahashi, Photodissociation of orange I monoanion studied using an electrostatic storage ring, Journal of Physics: Conference Series 875, 032035 (2017).

14. V. Motaneeyachart, Y. Hirose, A. Suzuki, S. Nakao, I. Harayama, D. Sekiba, T. Hasegawa, Epitaxial Growth of Baddeleyite NbON Thin Films on Yttria-Stabilized Zirconia by Pulsed Laser Deposition, Chem. Lett. 47, 65 (2018).

15. T. Katayama, A. Chikamatsu, Y. Hirose, M. Minohara, H. Kumigashira, I. Harayama, D. Sekiba, T. Hasegawa, Ferromagnetism with strong magnetocrystalline anisotropy in A-site ordered perovskite

$YBaCo_2O_6$ epitaxial thin film prepared via wet-chemical topotactic oxidation, J. Mater. Chem. C 6, 3445 (2018).

16. I. Harayama, D. Sekiba, Q. Zhao, A. Vantomme, W. Vandervorst, J. Meersschaut, Calibration of PIXE yields using Cu as a reference, Nuclear Instruments and Methods in Physics Research Section B 406, 115-118 (2017).

17. D. Sekiba, K. Chito, I. Harayama, Y. Watahiki, S. Ishii, K. Ozeki, Installation of high-resolution ERDA in UTTAC at the University of Tukuba: Determination of the energy resolution and the detection limit for hydrogen, Nuclear Instruments and Methods in Physics Research Section B: Beam Interactions with Materials and Atoms, Volume 401, 29-32 (2017).

18. K. Kawahara, A. Chikamatsu, T. Katayama, T. Onozuka, D. Ogawa, K. Morikawa, E. Ikenaga, Y. Hirose, I. Harayama, D. Sekiba, T. Fukumura, T. Hasegawa, Topotactic fluorination of perovskite strontium ruthenate thin films using polyvinylidene fluoride, CrystEngComm, 19, 313-317 (2017).

19. T. Onozuka, A. Chikamatsu, T. Katayama, Y. Hirose, I. Harayama, D. Sekiba, E. Ikenaga, M. Minohara, H. Kumigashira, T. Hasegawa, Reversible resistance modulation induced by fluorine substitution in perovskitenickelate NdNiO2 thin films, ACS Appl. Mater. Interfaces, 9, 10882-10887 (2017).

20. N. Nagakura, K. Fujii, I. Harayama, Y. Kato, D. Sekiba, Y. Watahiki, S. Yamashita, Experimental verification of a gain reduction model for the space charge effect in a wire chamber, Prog. Theor. Exp. Phys. 013C01 (2018).

21. M. Saito, T. Tanabe, M. Lintuluoto, E. B. Starikov, K. Noda, T. Majima, S. Tomita and K. Takahashi, Photodissociation of orange I monoanion studied using an electrostatic storage ring, Journal of Physics, Conference Series 875, 032035 (2017).

22. E Kita, H Yanagihara, M Kishimoto, K Ota, R Miyamoto, T Oda, N. Ohkohchi, Dynamic magnetization properties of platelet ferromagnetic nanoparticles and their heat generation injected in tumors of mice, IEEE Trans. Magn., 53 (11), 5100905 (2017).

23. H Latiff, M Kishimoto, S Sharmin, E Kita, H Yanagihara, T Nakagawa, Enhanced anisotropy in tetragonalized (Cu,Co)Fe_2O_4 particles via the Jahn-Teller effect of Cu^{2+} ions, IEEE Trans. Magn., 53 (11), 9402304 (2017).

24. Eiji Kita, Kenichi Shibata, Yuji Sasaki, Mikio Kishimoto, and Hideto Yanagihara, Magnetic anisotropy in spherical $Fe_{16}N_2$ core–shell nanoparticles determined by torque measurements AIP Advances 7 (2017) 056212.

6.2 Reviews and books

1. 黒澤 正紀、 鉱物の微細組織・化学組成に基づいた土器の焼成温度推定, 現代文明の基層としての古代西アジア文明ニュースレター、vol. 9, 55-60, 2017.

2. 笹 公和、イオンビーム多目的利用研究のための筑波大学 6 MV タンデム型静電加速器、日本加速器学会誌「加速器」、14 巻 1 号 5-14（2017）.

3. SEKIBA Daiichiro, Compendium of Surface and Interface Analysis, Chapter 12, Elastic Recoil Detection Analysis, Chapter 87, Rutherford Backscattering Spectrometry, Springer, 2018.

6.3 Poster or oral presentations at academic meetings

1. 上殿明良、石橋章司、角谷正友、“陽電子消滅による窒化物半導体中 0 次元特異構造（点欠陥）のキャリア捕獲の評価”、 第 65 回応用物理学会春季学術講演会、早稲田大学、東京、2018 年 3 月 19 日．(招待講演)

2. A. Uedono, M. Sumiya, and S. Ishibashi, “Carrier trapping by vacancy-type defects in group-III nitrides studied by means of positron annihilation”, Third DAE-BRNS Trombay Positron Meeting, Bhabha Atomic Research Centre, Mumbai, India, 23th March 2018 (Invited).

3. S. F. Chichibu, K. Kojima, A. Uedono, and Y. Sato, “Vacuum-fluorescent-display devices emitting polarized deep-ultraviolet and visible lights using m-plane $Al_{1-x}In_xN$ epitaxial nanostructures”, 11th Int. Sym. Semiconductor Light Emitting Devices, Banff, Alberta, Canada, 10th October 2017 (Invited).

4. A. Uedono, Study of point defects in nitrides and oxides by means of positron annihilation, 5th Int. Conf. Light-Emitting Devices and Their Industrial Applications, Pacifico Yokohama, Yokohama, Japan, 21st April 2017 (Invited).

5. A. Ozawa, “Rare-RI Ring in RIKEN RI Beam Factory” China-Japan collaboration workshop on “Nuclear mass and life for unravelling mysteries of r-process” 2017, 6/26-28, University of Tsukuba, Tsukuba, Japan (Invited).

6. 小沢　顕、不安定核の質量測定, 第 61 回放射化学討論会　核化学分科会、2017, 9/7, 筑波大学　(Invited).

7. A. Ozawa, “Past and future of Rare-RI Ring”, The 10th International Conference on Nuclear Physics at Storage Rings (STORI’17), 2017, 11/13-18, Kanazawa theater, Kanazawa, Japan (Invited).

8. T. Yamaguchi, “Storage-ring mass spectrometry of exotic nuclei”, International symposium on RI beam physics in the 21st century: 10th anniversary of RIBF, RIKEN, Wako, Japan, 4-5 Dec., 2017 (Invited).

9. T. Yamaguchi, “ILIMA project: isomeric beams, lifetimes and masses at the FAIR storage rings”, 10th International Conference on Nuclear Physics at Storage Rings, Kanazawa, Japan, 13-18 Nov., 2017 (Invited).

10. T. Yamaguchi, “ILIMA status report”, NUSTAR week 2017, Jozef Stefan Institute, Ljubljana, Slovenia, 25-29 Sep., 2017 (Invited).

11. Kimikazu Sasa, Tsutomu Takahashi, Seiji Hosoya, Kenta Takano, Yuta Ochiai, Maki Honda, Yuki Ohta, Aya Sakaguchi, Tetsuya Matsunaka, Hongtao Shen and Keisuke Sueki, Progress in Multi-nuclide AMS for the 6 MV AMS System at the University of Tsukuba, The 7th East Asia Accelerator Mass Spectrometry Symposium (EA-AMS 7), Guangxi Normal University, Guilin, China, November 20th to 25th 2017 (Invited).

12. Tetsuya Matsunaka, Kimikazu Sasa, Seiji Hosoya, HongTao Shen, Tsutomu Takahashi, Masumi Matsumura, Keisuke Sueki, Yukihiko Satou, Rapid C-14 measurement system at the University of Tsukuba and application for nuclear safety, The 7th East Asia Accelerator Mass Spectrometry Symposium (EA-AMS 7), Guangxi Normal University, Guilin, China, November 20th to 25th 2017 (Invited).

13. E. Kita, H. Yanagihara, M. Kishimoto, R. Miyamoto, T. Oda and N. Ohkohchi
Dynamic magnetization properties and heat generation of platelet ferromagnetic nanoparticles injected in tumors of mice, InterMAG Europe 2017, Dublin, Ireland 24th - 28th April 2017 (Invited).

14. 笹　公和、「加速器質量分析法（AMS）による極微量放射性核種の高感度分析手法の開発」、京都大学原子炉実験所専門研究会「放射化分析及び中性子を用いた地球化学的研究 -1-」、京都大学原子炉実験所（大阪府熊取市）、2018 年 1 月 10 日（水）. (招待講演)

15. 笹　公和、「タンデム・静電加速器を用いた先端研究の現状と将来展望 - 第 30 回「タンデム加速器及びその周辺技術の研究会」を記念して - 」、第 30 回「タンデム加速器及びその周辺技術の研究会」セラトピア土岐、岐阜県土岐市、日本原子力研究開発機構東濃地科学センター、2017 年 7 月 6- 7 日.（招待講演）

16. 関場大一郎、イオンビーム分析における検出器開発、平成 29 年度　電気学会低レベル放射線（能）に関する技術調査専門委員会ミニシンポジウム「放射線計測半導体検出器の先端開発と応用」、東京大学　弥生講堂アネックス　セイホクギャラリー、2017 年 11 月 1 日.（招待講演）

17. 関場大一郎、イオンビーム分析：水素を含む軽元素絶対深さプロファイル決定と構造解析、日本表面科学会　第 2 回関東支部講演大会、東京大学　山上会館、2017 年 4 月 8 日.（招待講演）

18. 笹 公和，細谷青児，本多真紀，高橋 努，佐藤志彦，高野健太，落合悠太，末木啓介，加速器質量分析法によるストロンチウム 90 の迅速定量法の開発，日本原子力学会「2018 年春の年会」，大阪大学吹田キャンパス（大阪市），2018 年 3 月 26 日~28 日.

19. S. Ishibashi and A. Uedono, Theoretical Calculation of Positron Annihilation Parameters for defects in UV materials (AlN, ZnO, Ga_2O_3), Int. Workshop on UV Materials and Devices, Fukuoka, Japan, 14th November 2017.

20. S. Iwashita, T. Moriya, T. Kikuchi, N. Noro, T. Hasegawa, and A. Uedono, Correlation between ion energies in CCRF discharges and film characteristics of titanium oxides fabricated via plasma enhanced atomic layer deposition, AVS 65th Int. Sym. & Exhibition, Long Beach Convention Center Long Beach CA, USA, 21th October 2017.

21. A. Uedono, Behaviors of free volumes during curing processes of epoxy resins for CFRP studied by positron annihilation, Joint Sym. 3rd Innovative Measurement and Analysis for Structural Materials and TIA-Fraunhofer workshop, AIST, Tsukuba, Japan, 4th October 2017.

22. S. Ishibashi and A. Uedono, Theoretical Calculation of Positron Annihilation Parameters in Group-III nitrides, 29th Int. Conf. Defects in Semiconductors, Matsue, Japan, 1st August 2017.

23. S. F. Chichibu, K. Kojima, S. Takashima, M. Edo, K. Ueno, M. Shimizu, T. Takahashi, S. Ishibashi, and A. Uedono, Role of point defects on the luminescent properties of epitaxial and ion-implanted Mg-doped GaN fabricated on a GaN substrate, 12th Int. Conf. Nitride Semiconductors, Strasbourg Convention Center, Strasbourg, France, 24th July 2017.

24. 角谷正友、福田清貴、上田茂典、浅井祐哉、Cho Yujin、関口隆史、上殿明良、尾沼猛儀、Sang Liwen、本田徹、III-V 族窒化物の価電子帯構造およびギャップ内準位の評価、第 65 回応用物理学会春季学術講演会、早稲田大学、東京、2018 年 3 月 20 日.

25. 嶋紘平、井口紘子、成田哲生、片岡恵太、上殿明良、小島一信、秩父重英、Mg イオン注入 N 極性面 GaN の時間分解フォトルミネッセンス評価、第 65 回応用物理学会春季学術講演会、早稲田大学、東京、2018 年 3 月 19 日.

26. 高島信也、田中亮、上野勝典、松山秀昭、江戸雅晴、小島一信、秩父重英、上殿明良、中川清和、Mg イオン注入 GaN MOSFET のチャネル特性向上、第 65 回応用物理学会春季学術講演会、早稲田大学、東京、2018 年 3 月 19 日.

27. 松木伸行、松井卓矢、満汐孝治、オローク ブライアン、大島永康、上殿明良、a-Si:H/c-Si ヘテロ界面近傍ボイド構造の高速評価－ボイドサイズと光学パラメータの相関普遍性に関する考察－、第 65 回応用物理学会春季学術講演会、早稲田大学、東京、2018 年 3 月 18 日.

28. 秩父重英、小島一信、嶋紘平、高島信也、江戸雅晴、上野勝典、石橋章司、上殿明良、Ga 基板上 Mg 添加 GaN の時間分解フォトルミネッセンス評価、第 78 回応用物理学会秋季学術講演会、福岡国際会議場、福岡、2017 年 9 月 7 日.

29. 松木伸行、オローク ブライアン、大島永康、上殿明良、a-Si:H/c-Si ヘテロ界面近傍ボイド構造の高速評価－ボイドサイズ・水素結合・Si 結合角ゆらぎの相互相関－、第 78 回応用物理学会秋季学術講演会、福岡国際会議場、福岡、2017 年 9 月 6 日.

30. 大和 良広、EPICS と CSS を用いた偏極イオン源制御システムの開発 Development of the polarized ion source control system using EPICS and CSS、日本加速器学会第 14 回年会、 平成 29 (2017)年 8 月.

31. 大和 良広, 偏極イオン源の現状 （震災復旧３）、第 30 回タンデム加速器及びその周辺技術の研究会、日本原子力研究開発機構　東濃地科学センター、平成 29(2017)年 7 月.

32. T. Moriguchi et al., Lamb-shift Polarized Ion Source at UTTAC, The 2017 International Workshop on Polarized Sources, Targets & Polarimetry(PSTP2017), KAIST Munji Campus, Dajeon, Republic of Korea, Oct 16-20, 2017.

33. 森口哲朗、筑波大学タンデム加速器施設 UTTAC の現状（2016 年度）、第 30 回タンデム加速器及びその周辺技術の研究会、日本原子力研究開発機構　東濃地科学センター（岐阜県）、2017/07/06-07.

34. 森口哲朗、偏極陽子ビームを用いた陽子吸収反応による不安定核の核偏極、日本物理学会 2017 秋季大会、宇都宮大学峰キャンパス、2017/09/12-15.

35. 森口哲朗、固体水素標的を用いた不安定核のスキン厚導出手法の開発、H28 年度 HIMAC 共同利用研究成果発表会、ホテルポートプラザ千葉、2017/04/17-18.

36. S. Suzuki, Performance of time-of-flight detector and demonstration of completely new position detector for mass measurements with the Rare-RI Ring, 10th International Conference on Nuclear Physics at Storage Rings (STORI'17), Kanazawa, Japan, 13- 18 November 2017.

37. 鈴木伸司、RI 質量測定用の薄膜を用いた準非破壊的位置検出器の開発、日本物理学会第 73 回年次大会、東京理科大学野田キャンパス、2018 年 3 月 22-25 日.

38. 鈴木伸司, 質量測定用飛行時間検出器の大型実機の開発, 日本物理学会秋季大会、宇都宮大学、2017 年 9 月 12-15 日.

39. 向井もも、KISS II : $^{196–198}$Ir のレーザー共鳴イオン化核分光筑波、日本物理学会第 73 回年次大会、宇都宮大学、2017 年 9 月 12-15 日.

40. Momo Mukai, Beta-ray detector in KISS, The inaugural symposium of the Tomonaga Center of the History of the Universe, University of Tsukuba, Mar. 26-27, 2018.

41. 山口貴之、Storage-ring mass spectrometry at GSI/FAIR、日本物理学会 2017 年秋季大会、宇都宮大学（峰キャンパス）2017.9.12-15.

42. Kimikazu Sasa, Seiji Hosoya, Tetsuya Matsunaka, Tsutomu Takahashi, Masumi Matsumura, Hangtao Shen, Yasuji Oura, Keisuke Sueki, Isobar separation techniques of ^{41}Ca AMS with the 6 MV tandem accelerator, The Fourteenth International AMS Conference (AMS14), Ottawa (Canada), August 14-18, 2017.

43. Kimikazu Sasa, Tsutomu Takahashi, Tetsuya Matsunaka, Seiji Hosoya, Masumi Matsumura, Hangtao Shen, Maki Honda, Aya Sakaguchi, Keisuke Sueki, Mark Stodola, Mark Sundquist, Performance of the 6 MV multi-nuclide AMS system at the University of Tsukuba, The Fourteenth International AMS Conference (AMS14), Ottawa (Canada), August 14-18, 2017.

44. Tetsuya MATSUNAKA, Kimikazu SASA, Seiji HOSOYA, Hongtao SHEN, Tsutomu TAKAHASHI, Masumi MATSUMURA, Keisuke SUEKI, Radiocarbon measurement system using gas ion source and automatic sample preparation system at the University of Tsukuba, The Fourteenth International AMS Conference (AMS14), Ottawa (Canada), August 14-18, 2017.

45. Tetsuya MATSUNAKA, Kimikazu SASA, Tsutomu TAKAHASHI, Seiji HOSOYA, Masumi MATSUMURA, Keisuke SUEKI, Yukihiko SATOU, Radiocarbon variations since 1960 in tree rings near the Tokai nuclear facilities in Japan, The Fourteenth International AMS Conference (AMS14), Ottawa (Canada), August 14-18, 2017.

46. Seiji HOSOYA, Kimikazu SASA, Tsutomu TAKAHASHI, Tetsuya MATSUNAKA, Masumi MATSUMURA, Hongtao SHEN, Keisuke SUEKI, Isobar suppression for ^{36}Cl-AMS with the 6 MV tandem accelerator, The Fourteenth International AMS Conference (AMS14), Ottawa (Canada), August 14-18, 2017.

47. Hongtao SHEN, Kimikazu SASA, Ming HE, Baojian HUANG, Masumi MATSUMURA, Seiji HOSOYA, Tetsuya MASUNAKA, Tsutomu TAKAHASHI, Maki HONDA, Keisuke SUEKI, Qingzhang ZHAO, Qi MENG, Kejun DONG, Xiaoming WANG, Yijun PANG, Xianlin YANG, Xiangdong RUAN, Shan JIANG, Study on Multiple radionuclides for Exposure Age Dating of Chinese Tiankeng, The Fourteenth International AMS Conference (AMS14), Ottawa (Canada), August 14-18, 2017.

48. Masumi MATSUMURA, Kimikazu SASA, Tetsuya MATSUNAKA, Tsutomu TAKAHASHI, Seiji HOSOYA, Keisuke SUEKI, Yukihiko SATOU, Hiroyuki MATSUZAKI, Contamination assessment of chemical preparation rooms for I-129 AMS, The Fourteenth International AMS Conference (AMS14), Ottawa (Canada), August 14-18, 2017.

49. Qi MENG, Hongtao SHEN, Ming HE, Kimikazu SASA, Huang BAOJIAN, Masumi MATSUMURA, Tetsuya MASUNAKA, Qingzhang ZHAO, Kejun DONG, Xiaoming WANG, Yijun PANG, Xianlin YANG, Xiangdong RUAN, Shan JIANG, TianKeng Sample Preparation for ^{36}Cl-AMS, The Fourteenth International AMS Conference (AMS14), Ottawa (Canada), August 14-18, 2017.

50. Seiji Hosoya, Kimikazu Sasa, Tsutomu Takahashi, Maki Honda, Yukihiko Satou, Kenta Takano, Yuta Ochiai, Koji Yamaguchi, Keisuke Sueki, Calusium-41 and Strontium-90 measurements with 6MV AMS, The 7th East Asia Accelerator Mass Spectrometry Symposium (EA-AMS 7), Guangxi Normal University, Guilin, China, November 20th to 25th 2017.

51. Hongtao Shen, Kimikazu Sasa, Qi Meng, Masumi Matsumura, Tetsuya Masunaka, Tsutomu Takahashi, Seiji Hosoya, Keisuke Sueki, Ming He, Baojian Huang, Qingzhang Zhao, Kejun,Dong, Xiangdong Ruan, Jiang Shan, Study on Cl-36 for Exposure Age Dating of Chinese Tiankeng, The 7th East Asia Accelerator Mass Spectrometry Symposium (EA-AMS 7), Guangxi Normal University, Guilin, China, November 20th to 25th 2017.

52. Yuta Ochiai, Kimikazu Sasa, Yuki Tosaki, Tsutomu Takahashi, Masumi Matsumura, Satomi Abe, Seiji Hosoya, Kenta Takano, Yuki Ohta, Keisuke Sueki, Correlation between the ^{36}Cl deposition flux and solar activity, The 7th East Asia Accelerator Mass Spectrometry Symposium (EA-AMS 7), Guangxi Normal University, Guilin, China, November 20th to 25th 2017.

53. Kenta Takano, Kimikazu Sasa,Tsutomu Takahashi, Yuki Tosaki, Yuki Ota, Seiji Hosoya, Yuta Ochiai, Keisuke Sueki, Kazuho Horiuchi, ^{36}Cl record in the Antarctic ice core around the cosmic-ray event of 5480 BC and improved ^{36}Cl AMS at the University of Tsukuba, The 7th East Asia Accelerator Mass Spectrometry Symposium (EA-AMS 7), Guangxi Normal University, Guilin, China, November 20th to 25th 2017.

54. T. Matsunaka, S. Nagao, M. Inoue, S. Ochiai, K. Hayakawa, N. Tang, N. Suzuki, S. Ogiso, H. Ando, T. Shimotani, N. Hirohashi, M. Nishizaki, T. Morita, S. Miki, T. Aramaki, I. Kudo, N. Honda, T. Takikawa, K. Sasa, M. Honda and K. Sueki, Anthropogenic iodine-129 and PAHs in seawater from the Japan Sea and the southern Okhotsk Sea, International Symposium “Environmental researches in northern Japan Sea and related regions: Renewed horizon of Japan-Russia scientific partnership” Shiinoki Cultural Complex, Kanazawa, Ishikawa Prefecture, 2018, March 3 to 4.

55. Tetsuya Matsunaka, Kimikazu Sasa, Keisuke Sueki, Akio Goto, Takahiro Watanabe, Yoshinori Tuchiya, Nobuo Hirano, Miwa Kuri, Masaaki Takahashi, Kohei Kazahaya, Isoji Miyagi, Hiroyuki Matsuzaki, Iodine isotopic composition in water from the crater lake and fumarolic area at Zao volcano, 15th International Workshop on WATER DYNAMICS, Deeper and Hotter in Frontier Earth, Sendai, Japan, 13-15 March, 2018.

56. 末木啓介、松尾一樹、笹公和、佐藤志彦、吉川英樹、箕輪はるか、福島第一原子力発電所事故によって放出された放射性粒子中の放射性核種、日本放射線安全管理学会第 16 回学術大会、ホルトホール大分　大分県大分市、2017 年 6 月 28-30 日.

57. 笹 公和、高橋 努、細谷 青児、高野 健太、落合 悠太、松中 哲也、末木 啓介、極微量放射性核種を超高感度で検出可能な 6 MV タンデム加速器質量分析装置の開発、第 14 回日本加速器学会年会、北海道大学、2017 年 8 月 1 日～ 3 日.

58. 笹 公和、石井 聰、大島 弘行、高橋 努、田島 義一、大和 良広、森口 哲朗、上殿 明良、筑波大学タンデム加速器施設の現状報告、第 14 回日本加速器学会年会、北海道大学、2017 年 8 月 1 日～ 3 日.

59. 笹 公和、高橋　努、細谷 青児、高野 健太、落合 悠太、本多 真紀、太田 祐貴、松尾 一樹、松中 哲也、坂口 綾、末木　啓介、6 MV タンデム加速器質量分析装置を用いた長寿命放射性核種の超高感度検出技術の開発、2017 年日本放射化学会年会・第 61 回放射化学討論会、筑波大学、2017 年 9 月 6 日～8 日.

60. 落合 悠太、笹 公和、高橋 努、戸崎 裕貴、松村 万寿美、安部 聡美、細谷 青児、高野 健太、末木 啓介、福島第一原子力発電所事故前後における降水中の塩素 36 同位体比変動、2017 年日本放射化学会年会・第 61 回放射化学討論会、筑波大学、2017 年 9 月 6 日～8 日.

61. 細谷　青児、笹　公和、高橋　努、本多　真紀、佐藤　志彦、高野　健太、落合　悠太、末木　啓介、加速器質量分析法を用いた ^{90}Sr 測定の試み、2017 年日本放射化学会年会・第 61 回放射化学討論会、筑波大学、2017 年 9 月 6 日～8 日.

62. 松中 哲也、笹 公和、高橋 努、恩田 裕一、谷口 圭輔、脇山 義史、末木 啓介、福島の河川における 2013 年から 4 年間にわたる粒子状ヨウ素 129 のフラックス、2017 年日本放射化学会年会・第 61 回放射化学討論会、筑波大学、2017 年 9 月 6 日～8 日.

63. 高野 健太、笹 公和、太田 裕貴、高橋 努、細谷 青児、落合 悠太、末木 啓介、6MV タンデム加速器質量分析装置における長寿命放射性核種 ^{36}Cl の検出感度の改善、2017 年日本放射化学会年会・第 61 回放射化学討論会、筑波大学、2017 年 9 月 6 日～8 日.

64. 本多 真紀、高久　雄一、松崎 浩之、笹　公和、末木 啓介、福島第一原子力発電所から放出された ^{129}I の化学形態別分析、 2017 年日本放射化学会年会・第 61 回放射化学討論会、筑波大学、2017 年 9 月 6 日～8 日.

65. 笹 公和、山崎明義、石井 聰、黒澤正紀、冨田成夫、左高正雄、楢本 洋、工藤 博、構造材料計測用マイクロイオンビーム分析装置によるビーム収束試験と材料組成分析、日本原子力学会「2017 年秋の大会」、北海道大学、2017 年 9 月 13 日～15 日.

66. 黒澤 正紀、笹 公和、石井 聰、丹沢花崗岩体の多相流体包有物の析出結晶、日本鉱物化学会 2017 年年会、愛媛大学、2017 年 9 月 12-14 日.

67. 池端 慶、服部浩一、黒澤 正紀、小室光世、笹 公和、石井 聡、三好陽子、島田和彦、戸塚修平、石橋純一郎、中部沖縄トラフ伊平屋北海丘熱水域に産する熱水変質鉱物の地球化学的研究、日本火山学会 2017 年度秋季大会、熊本大学黒髪南キャンパス、9 月 21 日～24 日.

68. 松中哲也、長尾誠也、井上睦夫、落合伸也、森田貴己、三木志津帆、笹公和、本多真紀、末木啓介、放射性ヨウ素 129 を用いた日本海における海洋循環に関する研究、金沢大学・環日本海域環境研究センター　共同利用シンポジウム「海流が繋ぐ日本海―オホーツク海の海洋循環・物質循環の変動機構」、石川四高記念文化交流館、2017 年 12 月 13 日.

69. 松中哲也、長尾誠也、井上睦夫、落合伸也、早川和一、唐寧、森田貴己、三木志津帆、工藤勲、滝川哲太郎、笹公和、本多真紀、末木啓介、日本海－オホーツク海における放射性ヨウ素 129 と多環芳香族炭化水素の動態研究、2018 年 1 月 11 日　中央水産研究所.

70. 笹 公和、高橋 努、松中 哲也、細谷 青児、太田 祐貴、高野 健太、落合 悠太、本多 真紀、末木 啓介、筑波大学 6 MV タンデム加速器質量分析装置による多核種 AMS と応用研究の現状、第 20 回 AMS シンポジウム、セラトピア土岐（岐阜県土岐市）、2017 年 12 月 14 日～15 日.

71. 高野健太、笹公和、高橋努、細谷青児、落合悠太、戸崎裕貴、堀内一穂、末木啓介、南極ドームふじアイスコア中の 5480 BC イベント周辺における宇宙線生成核種 ^{36}Cl フラックス、第 20 回 AMS シンポジウム、セラトピア土岐（岐阜県土岐市）、2017 年 12 月 14 日～15 日.

72. 細谷 青児、笹 公和、高橋 努、本多 真紀、佐藤 志彦、高野 健太、落合 悠太、末木 啓介、6 MV タンデム加速器による ^{90}Sr-AMS，第 20 回 AMS シンポジウム、セラトピア土岐（岐阜県土岐市）、2017 年 12 月 14 日～15 日.

73. 本多真紀、高久雄一、鹿籠康行、中野かずみ、松崎浩之、笹公和、高橋努、細谷青児、末木啓介、リアクションセル ICP-MS、ICP-MS/MS のための ^{129}I 標準溶液の作製、第 20 回 AMS シンポジウム、セラトピア土岐（岐阜県土岐市）、2017 年 12 月 14 日～15 日.

74. 太田祐貴、末木啓介、笹公和、高橋努、松中哲也、松村万寿美、戸崎裕貴、本多真紀、細谷青児、高野健太、落合悠太、佐藤志彦、吉川英樹、中間茂雄、箕輪はるか、福島原発周辺土壌中の ^{36}Cl の深度・蓄積量分布、第 20 回 AMS シンポジウム、セラトピア土岐（岐阜県土岐市），2017 年 12 月 14 日～15 日.

75. 落合悠太，笹公和，戸崎裕貴，高橋努，松村万寿美，本多真紀，細谷青児，高野健太，太田祐貴，末木啓介，つくば市における福島第一原子力発電所事故前後の ^{36}Cl 降下フラックス変動，第 20 回 AMS シンポジウム，セラトピア土岐（岐阜県土岐市），2017 年 12 月 14 日～15 日.

76. 落合悠太、笹公和、戸崎裕貴、高橋努、松村万寿美、細谷青児、高野健太、太田祐貴、末木啓介、つくば市における ^{36}Cl 降下フラックス変動、第１９回「環境放射能」研究会、高エネルギー加速器研究機構、2018 年 3 月 13 日‐15 日.

77. 笹　公和、アイスコア中の宇宙線生成核種 Cl-36 の測定 - 宇宙線強度変動および環境変動と年代の指標として、研究集会「南極ドームふじ氷床深層アイスコアの解析による気候・環境変動の研究の新展開」、国立極地研究所３F　多目的会議室、2018 年 3 月 28－29 日.

78. I. Harayama, T. Tamura, K. Tsujita, Y. Watahiki, K. Ozeki, D. Sekiba, Study of PSD with energy resolution for improvement of hydrogen sensitivity in high-resolution ERDA, (P1-10), 23rd International Conference on Ion Beam Analysis, Fudan University, Shanghai (China), 8-13 October, 2017.

79. 上ノ町水紀、辻田耕希、原山勲、杉澤悠紀、関場大一郎、島添健次、織田忠、高橋浩之、多チャンネル半導体と時間幅信号処理を用いた高分解能 ERDA 装置の開発、日本物理学会 第 73 回年次大会　東京理科大学野田キャンパス、2018 年 3 月 22～25 日.

80. I. Harayama, T. Tamura, K. Tsujita, Y. Watahiki, D. Sekiba, Study of background noise in high-resolution ERDA spectrum for improvement on detection limit of hydrogen, 第 18 回「イオンビームによる表面・界面解析」特別研究会, 物質・材料研究機構　WPI-MANA 棟オーディトリアム, 2017 年 12 月 15～16 日.

81. 加藤悠、藤井一毅、原山勲、長倉直樹、関場大一郎、綿引悠美、山下了、陽子ビーム空間電荷が引き起こすワイヤーチェンバーのゲイン低下評価、日本物理学会 2017 年秋季大会、宇都宮大学峰キャンパス、2017 年 9 月 12～15 日.

82. 長倉直樹、藤井一毅、原山勲、加藤悠、関場大一郎、綿引悠美、山下了、陽子ビーム空間電荷が引き起こすワイヤーチェンバーのゲイン低下評価、日本物理学会 2017 年秋季大会、宇都宮大学峰キャンパス、2017 年 9 月 12～15 日.

83. 三島賢二、広田克也、家城斉、猪野隆、岩下芳久、北口雅暁、北原龍之介、古賀淳、森下彩、長倉直樹、生出秀行、音野瑛俊、関義親、関場大一郎、嶋達志、清水裕彦、角直幸、角野浩史、竹谷薫、富田龍彦、山田崇人、山下了、横橋麻美、吉岡瑞樹、J-PARC/BL05 における中性子寿命測定実験：実験の現状と最新結果、日本物理学会 2017 年秋季大会、宇都宮大学峰キャンパス、2017 年 9 月 12～15 日.

84. 北原龍之介、岩下芳久、清水裕彦、広田克也、横橋麻美、北口雅暁、山下了、山田崇人、家城斉、長倉直樹、角野浩史、吉岡瑞樹、音野瑛俊、富田龍彦、角直幸、森下彩、古賀淳、生出秀行、嶋達志、三島賢二、猪野隆、竹谷薫、関義親、関場大一郎、J-PARC/BL05 における中性子寿命測定実験 : 高統計測定に向けたビームラインアップグレード、日本物理学会 2017 年秋季大会、宇都宮大学峰キャンパス、2017 年 9 月 12～15 日.

85. 辻田耕希、杉澤悠紀、原山勲、関場大一郎、高分解能 ERDA 測定に向けた 16 チャンネル位置敏感検出器用プリアンプの開発、日本物理学会 2017 年秋季大会　岩手大学上田キャンパス、2017 年 9 月 21～24 日.

86. 杉澤悠紀、原山勲、辻田耕希、関場大一郎、試作プリアンプと半導体検出器の組み合わせによる反跳水素の観察、日本物理学会 2017 年秋季大会　岩手大学上田キャンパス、2017 年 9 月 21～24 日.

87. 原山勲、関場大一郎、Qiang Zhao、Andre' Vantomme、Wilfried Van der Vorst、Johan Meersschaut、PIXE の定量性向上に向けた相対補正因子 h factor を用いた構成方法の評価、日本物理学会 2017 年秋季大会　岩手大学上田キャンパス、2017 年 9 月 21～24 日.

88. 永田晃大、Development of a Support System for Radiation Resistance Testing, ISTS 31（宇宙技術および科学の国際シンポジウム）、松山市、2017.6.3 – 6.9.

89. 冨田成夫、浅川大樹、高橋勝利、 静電型イオンストレージリングを用いた電子-イオン散乱の研究、第 65 回質量分析総合討論会、つくば国際会議場 、2017/5/17-19.

90. Shigeo Tomita, Experiments on Interaction of Electrons with Biomolecular Ions using Electrostatic Ion Storage Ring in KEK, 7th International Workshop on Electrostatic Storage Devices, Lyon, June 19-22, 2017.

91. 冨田成夫、高速クラスターイオン照射による固体内電子の応答、TIA 連携プログラム探索推進事業シンポジウム　準相対論的巨大クラスターイオンビームが開く世界：ゲノム改変・極端非平衡材料創生に向けて、つくば国際会議場、2017/9/11-12.

92. 冨田成夫、高速クラスターイオン入射による固体内エネルギー付与過程、日本放射線影響学会　第 60 回大会、京葉銀行文化プラザ、 2017.10.26-28.

93. 椎名陽子、木下亮、松田誠、今井誠、川面澄、左高正雄、笹公和、冨田成夫、高速クラスター照射におけるコンボイ電子収量の標的膜厚依存性、第１２回先進原子力科学技術に関する連携重点研究討論会，量子科学技術研究開発機構 高崎量子応用研究所，2017 年 8 月.

94. 山崎明義、笹公和、石井聰、黒澤正紀、冨田成夫、上殿明良、筑波大学 6MV タンデム加速器イオンマイクロビームシステムのビーム集束と元素分布測定、第 30 回タンデム加速器及びその周辺技術の研究会、セラトピア土岐、2017 年 7 月 6-7 日.

95. A. Yamazaki, K. Sasa, S. Ishii, M. Kurosawa, S. Tomita, H. Naramoto, M. Sataka, H. Kudo, S. Shiki, M. Ohkubo, A. Uedono, Elemental Mapping Using the Ion Microbeam System on the 6 MV Tandem accelerator at the University of Tsukuba, 3rd International Symposium for Innovative Measurement and Analysis for Structural Materials, 産総研つくば中央、2017 年 10 月 3-5 日.

96. A. Yamazaki, H. Naramoto, K. Sasa, S. Ishii, M. Kurosawa, S. Tomita, M. Sataka, H. Kudo, M. Ohkubo, A. Uedono, Imaging of Hydrogen in Thin Samples with Microbeam Transmission ERDA Method, 3rd International Symposium for Innovative Measurement and Analysis for Structural Materials, 産総研つくば中央、2017 年 10 月 3-5 日.

97. A. Yamazaki, H. Naramoto, M. Sataka, H. Kudo, K. Sasa, S. Ishii, H. Oshima S. Tomita, M. Ohkubo, A. Uedono, Two-dimensional mapping of hydrogen and other elements in thin materials with microbeam-based transmission ERDA and PIXE, 23th International Conference on Ion Beam Analysis (IBA2017), Shanghai, China, 2017 年 10 月 8-13 日.

98. A. Yamazaki, K. Sasa, S. Ishii, S. Tomita, Y. Shiina, M. Kurosawa, H. Naramoto, M. Sataka, H. Kudo, S. Shiki, M. Ohkubo, A. Uedono, Improvement of ion microbeam scanning system for realizing multi-method elemental analysis at the University of Tsukuba, 23th International Conference on Ion Beam Analysis (IBA2017), Shanghai, China, 2017 年 10 月 8-13 日.

99. 山崎　明義、楢本　洋、左高 正雄、工藤　博、笹 公和、石井 聰、冨田 成夫、黒澤 正紀、志岐 成友、大久保雅隆、上殿 明良、筑波大学 6MV タンデム加速器イオンマイクロビームシステムにおけるビーム集束と He ビームによる PIXE-透過 ERDA 同時測定、33 回 PIXE シンポジウム、京都大学宇治キャンパス、2017 年 10 月 19-21 日.

100. H Latiff, M Kishimoto, S Sharmin, E Kita, H Yanagihara, T Nakagawa, Enhanced anisotropy in tetragonalized (Cu,Co)Fe_2O_4 particles via the Jahn-Teller effect of Cu^{2+} ions, InterMAG Europe 2017, Dublin, Ireland 24th - 28th April 2017.

6.4 UTTAC seminars

2017.5.17 Precision mass measurements of neutron-deficient nuclei in A ~ 60 − 80 region via multireflection time-of-flight mass spectrograph, *Souta Kimura* (*University of Tsukuba*).

2017.6.16 Ice core record of ^{10}Be from Dome Fuji, Antarctica revealing the history of cosmic-ray variations, *Kazuho Horiuchi* (*Hirosaki University*).

2017.9.1 Measurement of jet spectra reconstructed with charged particles in Pb-Pb collisions at $\sqrt{s_{\mathrm{NN}}} = 5.02$ TeV with the ALICE detector at the LHC, *Hiroki Yokoyama* (*University of Tsukuba*).

2017.10.23 Measurements of Azimuthal Angle Dependence of HBT Radii with respect to Event Plane in $\sqrt{s_{\mathrm{NN}}} = 2.76$ TeV Pb-Pb Collisions at LHC-ALICE, *Naoto Tanaka* (*University of Tsukuba*).

2017.11.8 Laser resonance ionization spectroscopy of $^{196–198}$Ir, *Momo Mukai* (*University of Tsukuba*).

2017.11.30 Measurement of the sixth order cumulant of net-proton multiplicity distributions in $\sqrt{s_{\mathrm{NN}}} = 200$ GeV Au+Au collisions, *Toshihiro Nonaka* (*University of Tsukuba*).

2018.1.15 Measurement of elliptic flow at forward and backward rapidities in d+Au collisions at $\sqrt{s_{\mathrm{NN}}}$ = 200, 62.4, 39 and 19.6 GeV with PHENIX detector at RHIC, *Kazuki Sato* (*University of Tsukuba*).

2018.1.15 Measurement of soft-hard correlations with jets and the event plane in $\sqrt{s_{\mathrm{NN}}} = 2.76$ TeV Pb+Pb collisions at ALICE experiment, *Yoshimi Rebaza* (*University of Tsukuba*).

2018.1.15 Reaction Cross-section Measurement of proton drip line nucleus ^{17}Ne using Solid Hydrogen Target, *Masamichi Amano* (*University of Tsukuba*).

2018.1.15 Development of hard-to-measure nuclides measurements by Accelerator Mass Spectrometry with the 6 MV tandem accelerator, *Seiji Hosoya* (*University of Tsukuba*).

2018.1.15 Cross wake field and correlated Head-Tail instability in beam-beam collision with a large crossing angle, *Nami Kuroo* (*University of Tsukuba*).

7.

THESES

Doctor theses

Souta Kimura	Precision mass measurements of neutron-deficient nuclei in A ～ 60-80 region via multireflection time-of-flight mass spectrograph
Momo Mukai	In-gas-cell laser resonance ionization spectroscopy of $^{196-198}$Ir

Master theses

Masamichi Amano	Reaction Cross-section Measurement of proton drip line nucleus ^{17}Ne using Solid Hydrogen Target
Seiji Hosoya	Development of hard-to-measure nuclides measurements by Accelerator Mass Spectrometry with the 6 MV tandem accelerator
Koki Tsujita	Development of high-sensitivity ERDA equipped with multi-channel semiconductor detector
Naoki Yamamoto	Experimental study of electron – molecule scattering using electrostatic ion storage ring

Undergraduate theses

Yuta Ochiai	Evaluation of temporal variation of cosmogenic ^{36}Cl flux
Takeshi Mitsuhashi	Geochemical study of Iheya North Knoll hydrothermal field in the Okinawa Trough
Ruri Suganuma	Production process of NO_3 in atmosphere by cosmic rays

8.

LIST OF PERSONNEL

Tandem Accelerator Complex

A. Uedono	Director, Professor
K. Sasa	Associate Professor
D. Sekiba	Lecturer
T. Moriguchi	Assistant Professor
H. Oshima	Electrical Engineer
Y. Tajima	Mechanical Engineer
S. Ishii	Mechanical Engineer
T. Takahashi	Electrical Engineer
Y. Yamato	Electrical Engineer
M. Sataka	Research Fellow
M. Matsumura	Research Supporter
S. Kuramochi	Administrative Staff
M. Satoh	Administrative Staff
H. Muromachi	Administrative Staff

Research Members[1]

Division of Physics

A. Ozawa T. Moriguchi K. Sasa S. Suzuki

T. Yamaguchi (Saitama University [Cross-appointment])

Hongtao Shen (Guangxi Normal University, China [Visiting Foreign Research Fellow])

Division of Applied Physics

E. Kita D. Sekiba S. Sharmin S. Tomita

A. Uedono H. Yanagihara I. Harayama

Division of Geoscience

M. Kurosawa K. Ikehata

Division of Chemistry

K. Sueki A. Sakaguchi

Division of Information and Systems

T. Kameda

[1] The “research members” include the authors and coauthors within 5 years back from this fiscal year, as well as the members of research projects running at UTTAC.

Staff of Open Advanced Facilities Initiative

H. Kudo H. Naramoto M. Sataka

K. Awazu (National Institute of Advanced Industrial Science and Technology [AIST])

S. Aoki (Comprehensive Research Organization for Science and Society [CROSS])

Staff of Joint Research Projects with Other Organizations

A. Yamazaki (Cross-ministerial Strategic Innovation Promotion Program [SIP])[2]

Y. Watahiki (Nanotech Career-up Alliance [CuPAL])

Graduate students

Graduate School of Pure and Applied Sciences

Graduate School of Life and Environmental Sciences

M. Ahmed	Y. Shiina	S. Kimura	M. Mukai
M. Honda	Y. Liu	R. Patel	H. Latiff
Y. Hisamatsu	T. Tainosho		

M. Matsumoto	E. Noguchi	D. Kamioka	T. Tamura
R. Tomita	T. Ojima	M. Amano	S. Hosoya
N. Yamamoto	K. Takano	Y. Ota	Y. Sugisawa
J. Kikuda	T. Eguchi	Y. Hosoi	H. Onoda
K. Tsujita	A. Nagata	A. Yasuda	Y. Asai
K. Sako	K. Nakayama	N. Kuroo	

Undergraduates

S. Hashimoto	Y. Ochiai	K. Hattori	R. Mase
T. Mitsuhashi	R. Suganuma	S. Yaguchi	W. Ueno
S. Ando			

External users and collaborators

Y. Tosaki	National Institute of Advanced Industrial Science and Technology (AIST)
K. Masumoto	High Energy Accelerator Research Organization (KEK)
T. Miura	High Energy Accelerator Research Organization (KEK)
H. Matsumura	High Energy Accelerator Research Organization (KEK)
Y. Oura	Tokyo Metropolitan University
T. Hara	Tokyo Metropolitan University
Y. Katou	The University of Tokyo

[2] Also, a staff of *Open Advanced Facilities Initiative*

N. Nagakura	The University of Tokyo
K. Fujii	The University of Tokyo
K. Ozeki	Ibaraki University
T. Matsunaka	Kanazawa University
K. Wakayama	Saitama University
H. Arakawa	Saitama University
K. Inomata	Saitama University
K. Nishimuro	Saitama University
T. Fujii	Saitama University
T. Kobayashi	Saitama University
R. Tanaka	Yamaguchi University